



מכון ויצמן למדע

WEIZMANN INSTITUTE OF SCIENCE

Thesis for the degree
Doctor of Philosophy

Submitted to the Scientific Council of the
Weizmann Institute of Science
Rehovot, Israel

עבודת גמר (תזה) לתואר
דוקטור לפילוסופיה

מוגשת למועצה המדעית של
מכון ויצמן למדע
רחובות, ישראל

By
Itamar Israeli
(Israelashvili)

מאת
איתמר ישראלי
(ישראלאשוילי)

גלאי קסנון נוזלי חדשני לספקטרוסקופיה והדמיה משולבת של ניטרונים
מהירים וקרינת גמא

A novel liquid-Xenon detector concept for combined fast-neutron
and gamma-ray imaging and spectroscopy

Advisor: Professor
Amos Breskin

מנחה : פרופסור
עמוס ברסקין

Mars 2017

ניסן התשע"ז

Acknowledgments

I would like to thank my supervisor Prof. Amos Breskin for his encouragement and confidence, guidance and valuable input during all the stages of this research. I am especially thankful for the opportunity provided to me for developing in so many levels. The various discussions offered me with the opportunity to learn from his unmatched experimental knowledge and his deep theoretical grasp. His positive and straightforward leadership, patience and support in difficult moments granted me with an invaluable reference point.

I am also deeply grateful to Dr. Lior Arazi, Dr. David Varstky and Dr. Elad Nisan Caspi for all the productive discussions, patience and time shared within and outside the laboratory, for their deep theoretical insight, and determined experimental drive; for their unmatched experience with electronics and phototubes and their willingness to discuss and explain the several subtleties related to these subjects; to Dr. Sergei Shchemelinin for all his assistance in the effort put into the production and characterization of the photocathodes; to Dr. Michael Rappaport for his valuable suggestions and advices, rooted in his textbook experience, and his friendliness; to Benny Pasmantirer and Oz Diner for their impressive design work on the cryogenic system and GPM and their readiness to share their experience in design software; to Moshe Klin, Yafa Gil, Yehuda Asher, Harel Takeia and Alex Jahanfard for their willingness to share their year long experience in the laboratory and patience and dedication in the workshop; to Doron Bar from Soreq- NRC for his valuable assistance in GEANT4 toolkit and parallel computing; to Dvir Hamawi, Amil Malka, Sharon Hliva, Zion Versolker, Moshe Kendelker, Yitzhak Halamish, Nissim Mimon, Hanoch Apteker and Sharon Biton from NRCN for their appreciated assistance in preparation of the collimators for the neutron and gamma sources.

I would also like extend a warm thanks to my colleagues in the Radiation Detection Physics Laboratory in WIS, Dr. Artur Emanuel Cardoso Coimbra, M.Sc. Michael Pitt, M.Sc. Luca Moleri, Dr. Arindam Roy, M.Sc. Eran Erdal, M.Sc. Adam Rubin for their valuable skills and for taking their time to transmit their knowledge, for all of their support and for giving a helpful hand when needed. Warm thanks to my colleagues in the NRCN Dr. Arie Beck, Dr. Eyal Yahel, Dr. Alex Landu and Dr. Udi

Netzer for their heedful efforts throughout the study. I would especially like to thank Dr. Marco Cortesi for sharing his knowledge and providing helpful and motivational presence and discussions at the initial stages of the project.

My most grateful acknowledgement goes to my family; to my parents, Moshe and Ruth, for providing the backbone over which everything else rests, to my wife Michal for supporting me in every possible way, to my parents-in-law Shlomo and Simcha for all of their help, to my brothers Jacob, Michal and Yochai and to my kids Tamar, Eitan and Boaz who brought a new and precious beacon guiding our lives.

This work was partly supported by the PAZY Foundation (Grant No. 258/14), by the Minerva Foundation with funding from the German Ministry for Education and Research (Grant No. 710827) and by the Israel Science Foundation (Grant No. 477/10).

וְזָכַרְתָּ אֶת־ה' אֱלֹהֶיךָ כִּי הוּא הַנָּתַן לָךְ כֶּחַ לַעֲשׂוֹת חַיִּיל (דברים ח יח)

Declaration

I hereby declare that this thesis summarizes my independent research. Part of the research (mainly part of the GPM R&D, described in section 6.2.2 and appendix 8.1) was done in collaboration with Dr. Artur E. C. Coimbra, who was at that time a PhD student in Coimbra University of Portugal.

Table of Contents

1	Introduction and motivation	14
2	Liquid xenon as a detection medium.....	18
2.1	Thermodynamic properties of xenon	19
2.2	Interaction modes of radiation with liquid xenon	19
2.2.1	Charged particles.....	19
2.2.2	Gamma-ray and x-ray interactions.....	21
2.2.3	Neutrons	22
2.3	Ionization and excitation	24
2.4	Scintillation – recombination and de-excitation.....	25
2.5	Temporal components of scintillation	26
2.6	Scintillation and ionization yield.....	28
3	Cesium iodide photocathodes and gaseous photomultipliers.....	30
3.1	Cesium iodide photocathodes.....	30
3.2	Gas Electron Multipliers and Thick Gas Electron Multipliers.....	34
3.2.1	Photo-detection efficiency of a GPM.....	37
4	Experimental setup and methodology.....	39
4.1	LXe cryostat	39
4.2	Cryogenic GPM.....	42
4.3	Readout electronics and typical signals	44
4.4	Setup for point-like UV-photon imaging (GPM only) at room temperature.	49
4.5	Setup for gain measurements	51
4.6	Setup for gamma-ray imaging (GPM+LXe converter).....	52
4.7	Setup for imaging by mixed neutron and gamma field (GPM+LXe converter)	

4.7.1	Time-of-flight measurements.....	55
4.7.2	Edge imaging with mixed neutron & gamma field.....	56
5	GEANT4 simulations for converter optimization and predicted performance	58
5.1	Methodology	58
5.2	Optimization of the LXe converter	59
5.2.1	Deposited Energy Spectra.....	60
5.2.2	Detection Efficiency	64
5.2.3	Spatial resolution	67
5.2.4	Effect of beam impinging point	73
5.2.5	Capillary - dimensions optimization.....	74
5.2.6	Simulation of radiographic images – elemental differentiation.....	75
5.3	Predicted performance of the small size laboratory detector prototype.....	80
5.3.1	Simulation of gamma imaging of a Pb-edge absorber.....	85
5.3.2	Simulation of gamma imaging of a narrow beam and a pencil beam....	89
5.3.3	Simulation of neutron imaging of a pencil beam.....	93
5.3.4	Simulation of mixed neutron and 4.4MeV gamma-ray imaging of a Pb edge absorber	96
5.3.5	Comparison between simulation FWHM results of the "general" large detector and the small size laboratory detector prototype	97
6	Results and discussion	99
6.1	Point-like UV-photon imaging at room temperature.....	99
6.2	Gain measurements	103
6.2.1	Ne/CH ₄ (5%).....	103
6.2.2	He/CF ₄ and He/CH ₄ mixtures	105

6.3	Gamma-ray imaging experiments	106
6.3.1	Gamma-ray imaging experiments of a Pb-object edge.....	108
6.3.2	Imaging of a narrow gamma beam	111
6.4	Measurements in mixed neutron & gamma field	113
6.4.1	Time-of-flight measurements.....	113
6.4.2	Edge imaging with mixed neutron & gamma field.....	115
7	Summary and conclusions.....	119
8	Appendices.....	125
8.1	Appendix A – Evaporation and characterization of CsI photocathode	125
8.1.1	CsI photocathode evaporation.....	125
8.1.2	Photocathode characterization	126
8.2	Appendix B – Estimation of the overall extraction efficiency	129
8.3	Appendix C - Large electrode preparation and testing.....	131
8.3.1	Leak current measurement	131
8.3.2	Optical discharge localization.....	131
8.4	Appendix D - α source imaging	133
9	Bibliography	137
10	List of all publications authored by Itamar during the study.....	147
11	List of publications resulting from this work	149

List of Abbreviations

LXe	Liquid Xenon
GPM	Gas photo multiplier
GEM	Gas electron multiplier
THGEM	Thick gas electron multiplier
CsI	Cesium iodide
WLiX	Weizmann Institute liquid Xenon cryostat
RT	Room temperature
DDGR	dual discrete gamma-ray radiography
FNRT	fast-neutron resonant transmission radiography
FWHM	Full width at half maximum
TOF	Time-of-flight
HEU	Highly enriched uranium
WIMP	Weakly Interacting Massive Particle
COG	Center-of-gravity
QE	Quantum Efficiency
PDE	Photo Detection Efficiency
PE	Photoelectron

תקציר

עבודת דוקטורט זו הוקדשה למחקר ופיתוח של קונספט גלאי חדשני להדמיה וספקטרוסקופיה בו-זמנית של ניטרונים מהירים וקרינת גמא; מטרתנו הייתה פיתוח מערכת דימות, יעילה ובעלת תווך גילוי יחיד, לסריקת מטענים ומכולות בחיפוש אחר חומרי נפץ וחומרים בקיעים חבויים. הגלאי החדש כולל נצנץ קסנון נוזלי, מוכל בצינוריות טפזל (Tefzel) ומצומד למכפל-אור גזי (Gaseous Photomultiplier -GPM) בעל יכולת דימות ורגישות לנצנוץ אולטרא-סגול. ייחודיותו וחדשנותו של גלאי הקסנון הנוזלי שפיתחנו, לעומת טכניקות גילוי אחרות, הינם יכולת דימות באותו תווך עם יעילות גילוי טובה הן עבור קרינת ניטרונים מהירים והן עבור קרינת גמא וכן יכולת הגימלון המאפשרת בניית גלאי בעל שטח פנים גדול למדידת מכולות.

המחקר התמקד בתיקוף רעיון הגלאי החדשני לגילוי בו זמנית של חומרי נפץ מוסתרים, בעיקר חומרים בעלי Z נמוך, וחומרים בקיעים בעלי Z גבוה – תוך שימוש בניטרונים מהירים וקרינת גמא, בהתאמה. הדמיה של שני סוגי הקרינה, בתחום אנרגטי של 0-14 MeV, מסתמך על איכון אור הנצנוץ האולטרא-סגול, הנפלט כתוצאה מאינטראקציה של הקרינה עם ממיר הקסנון הנוזלי, על ידי מכפל-אור גזי הרגיש לאור זה – מכפל אלקטרוניים גזי עבה רב-שלבי (cascaded). הפוטואלקטרוניים מוכפלים ומיקום פליטת האור נמדד באמצעות קריאת ענני אלקטרוניים, שעברו את תהליך ההכפלה בגז, המשרים אותות חשמליים על אלקטרודה המחולקת לפדים.

מחקר סימולצייט מחשב (GEANT4) מקיף בוצע לצורך אופטימיזציה של תצורת ממיר הקסנון הנוזלי והגאומטריה בה נמצא. סימולציות בוצעו גם על מנת להעריך את הביצועים הצפויים עבור שיקוף גמא וניטרונים מהירים עם קסנון נוזלי המוכל בצינוריות טפזל לעומת נפח קסנון נוזלי מלא. תוצאות הסימולציה שימשו לקביעה בפועל של תצורת ממיר הקסנון הנוזלי בגלאי.

בוצע אפיון מקיף בטמפרטורת החדר ובטמפרטורות קריוגניות, של גלאי GPM בעל שלושה מכפלי THGEM בקוטר פעיל של 100 מ"מ, בעל פוטוקטודת CsI שנודפה על המכפל הראשון. האפיון בוצע בקריוסטט WLiX (Weizmann Institute Liquid Xenon cryostat) בגזי מניה שונים ובלחצים שונים. מחקר יכולת הדימות, בטמפרטורת החדר ובטמפרטורות קריוגניות, נעשה באמצעות קריאה ועבוד אותות מאלקטרודת הגלאי המחולקת ל-61 פדים, על ידי אלקטרוניקה רבת-ערוצים APV25-SRS שפותחה ב- CERN-RD51 ועברה הסבה לפעולה בטמפרטורה קריוגנית.

ניסויי דימות עם קרינת ניטרונים וגמא נעשו באמצעות גאומטריית גלאי לא אופטימלית, תוך שימוש במקורות ^{60}Co (קרינת גמא באנרגיות של 1.17 MeV ו-1.33 MeV) ו-AmBe (שילוב של ניטרונים מהירים (0-11 MeV) וקרנת גמא (4.4 MeV)). רזולוציות מרחביות של $12\pm 2\text{mm}$ (FWHM) ו- $10\pm 2\text{mm}$ (FWHM) התקבלו, בהתאמה, מניסויי הקרנה של שפת עצם העשוי

עופרת, עם קרינת גמא באנרגיות הנמוכות ועם זו של שדה הקרינה המשולב. תוצאות הניסויים מתאימות יפה לתוצאות הסימולציות עבור גיאומטריית גלאי זו. הודגמה רזולוציה ספקטרוסקופית לגמא אך זו לניטרונים לא בוצעה במסגרת עבודה זו.

הרזולוציות המרחביות הצפויות, על פי סימולציה, עבור גלאי בגיאומטריה משופרת בו קצר המרחק בין הפוטוקטודה וממיר הקרינה, במדידת קרן בעלת רוחב אינפטיסימאלי, הינן 2-4 מ"מ ו-2 מ"מ (FWHM) לקרינת גמא באנרגיה רלוונטית של 4.4 ו-15.1 MeV וניטרונים באנרגיה של 1-15 MeV, בהתאמה. יעילות הגילוי הצפויה עבור ממיר קרינה בעובי 50 mm הינה 20% ו-35% בהתאמה.

תוצאות המחקר מצביעו על כך שקונספט גלאי חדשני זה, להדמיה וספקטרוסקופיה בו-זמנית של ניטרונים מהירים וקרינת גמא, הינו בעל פוטנציאל לשימוש במדידות טרנסמיסיית ניטרונים רזוננטית (Fast-Neutron Resonant Transmission - FNRT) ושיקוף גמא דו-אנרגטי (Dual Discrete Gamma-ray Radiography - DDGR). בעוד שכושר ההפרדה של גמא בשתי האנרגיות הצפויות הנו סביר, מדידת זמן המעוף של הניטרונים תדרוש שיפור הרזולוציה בזמן של מכפל האלקטרונים.

Abstract

This Ph.D. thesis is dedicated to the design and development of a new detector concept for simultaneous imaging and spectroscopy of fast-neutrons and gamma radiation. The work was motivated by the aim of developing a single efficient radiographic imager for scanning cargo and containers, in the search of small, operationally-relevant quantities of concealed special nuclear materials (SNM), such as highly enriched uranium (HEU) and ^{239}Pu and explosives. The reason to search for rather small quantities (500 g) of SNM is to interdict the scenario of terrorists smuggling small pieces of weapon grade uranium into targeted area, in order to assemble and deploy a crude improvised nuclear device. These requirements influence the design of detector parameters, such as position resolution and detection efficiency.

The new detector combines a liquid-xenon (LXe) scintillator contained in “fiber-like” Tefzel capillaries, coupled to a UV-sensitive Gaseous Imaging Photomultiplier (GPM). The research focused on validating this new idea for simultaneously detecting hidden explosives, predominantly of low-Z materials, and high-Z fissile materials - utilizing fast neutrons and gamma radiation, respectively. Imaging of both radiations, in the energy range of 0-14MeV, relies on their induced UV scintillation-light localization from in a LXe converter with a UV-sensitive GPM - a cascaded Thick-Gas Electron Multiplier (THGEM) coated with a cesium iodide (CsI) photocathode and equipped with a patterned readout anode electrode.

A comprehensive computer-simulation (GEANT4) study was performed aiming at the optimization of the LXe converter configuration and geometry. Simulations were also carried out in order to evaluate the expected performance for gamma-ray and fast-neutron radiography of the LXe in Tefzel capillaries versus a plain-volume LXe scintillator. The simulation results were used to determine the capillary LXe convertor configuration.

Characterization of a 100 mm in diameter triple-THGEM GPM detector, with CsI photocathode deposited on its first element, has been performed at room temperature (RT) and at LXe cryogenic conditions - in the Weizmann Institute Liquid Xenon cryostat (WLiX); the detector was investigated thoroughly in different counting gases and operation pressures. The imaging performances, at RT and at cryogenic

temperature, were studied with a segmented, 61-pads readout electrode and APV25-SRS CERN-RD51 readout electronics designed to operate at cryogenic temperature, using a dedicated software.

Gamma and neutrons imaging experiments were performed at the laboratory, using a ^{60}Co gamma source (1.17 and 1.33 MeV) and a AmBe neutrons source yielding a mixed field of 4.4 MeV gamma and 0-11 MeV fast neutrons.

The localization properties of low-energy gamma-rays (^{60}Co) and mixed fast-neutrons/gamma (AmBe) in the present, not optimal detector geometry, derived from irradiation of a Pb edge object, yielded spatial resolutions of $12\pm 2\text{mm}$ (FWHM) for gamma and $10\pm 2\text{mm}$ (FWHM) for the mixed gamma/neutron field. The experimental results are in good agreement with GEANT4 simulations.

For preferable detector geometry, in which the photocathode is closer to the LXe converter, the expected ultimate pencil-beam resolutions, for the energy ranges foreseen for the gamma/neutron radiography, e.g. 4.43 and 15.1 MeV gamma-rays and 1-15 MeV neutrons, are 2-4 mm and ~ 2 mm (FWHM), respectively. The expected detection efficiencies for a 50 mm thick converter would be $\sim 35\%$ and 20%, respectively.

The results indicate that the novel mixed radiation-field detection concept has the potential of use in fast-neutron resonant transmission (FNRT) radiography and in dual discrete gamma-ray radiography (DDGR). While the energy resolution of the detector would be sufficient for gamma spectroscopy, that of neutrons, by time-of-flight, would require further improvement of the GPM's time resolution.

1 Introduction and motivation

The general objective of this research is to develop improved screening tools in aviation and border crossing security for an efficient and more specific detection of contraband - mainly explosives and special nuclear materials (SNM) [1,2]. The quantities of interest of nuclear materials (e.g. Pu, or highly enriched U - HEU) are ~500 g, in air/marine/truck cargo; that of explosives are of ~200 g in air cargo/luggage. The requirement to detect sub-critical quantities of SNM stems from the possibility of terrorists smuggling small pieces of weapon grade uranium, or plutonium, into targeted area, in order to assemble and deploy a crude improvised nuclear device. Regarding explosives, it has been unfortunately shown, that such small quantities of plastic explosives can down an airplane.

Presently, commercial systems based on high energy X-ray or gamma-ray radiographic inspection methods are being applied for investigating the content of aviation- and marine-cargo containers, trucks and nuclear waste containers (see for example Ref [3]). These inspection methods provide high-resolution images of shape and density, but they lack the capability to distinguish between organic materials of similar density but of different chemical composition. Selectivity of high-Z elements can be achieved by Dual Energy Bremsstrahlung Gamma Radiography (DEBG), analyzing spectra generated by accelerated electrons at two different bombarding energies [4, 5, 6]. These techniques provide rather crude information on effective atomic composition of a material; however, discrimination between hidden fissile substances (like HEU or Pu) and “benign” high-Z materials (like Pb or W) are not possible because of the small differences in density and atomic numbers. This can be improved by using well defined dual-energy gamma radiation fields, like those originating from nuclear transitions yielding discrete gamma-emission lines. In particular the $^{11}\text{B}(d,n\gamma)^{12}\text{C}$ reaction provides well separated 4.43 and 15.1 MeV gamma lines. This technique is called Dual-Discrete-Energy Gamma Radiography (DDEGR) [7].

Fast-neutron imaging methods were extensively investigated in the US in the 90's and early 2000's [8]. These provide a sensitive probe for low-Z elements like H, C, N and O, which are the main constituents of explosives and narcotics. In fast-neutron

resonance radiography (FNRR) [9] two-dimensional (2-D) elementally-resolved images are obtained from fast-neutron radiographic images, taken at different neutron energies (1-10 MeV) chosen to cover the resonance cross-section features of those low-Z elements. In baggage and container screening FNRR holds promise for detecting a broad range of explosives, determining simultaneously the identity and density distribution of their principal constituent elements [7].

An inspection system featuring both fast-neutron resonance- and dual-energy gamma radiography techniques will combine the capability of low-Z objects detection and substance-identification of FNRR with the high-Z selectivity of DDEG. This requires suitable radiation sources, emitting intense fast-neutrons and gamma-rays as well as an efficient imaging detector of fast-neutrons and gamma radiation. As mentioned above, a suitable source for both is one based on the $^{11}\text{B}(\text{d},\text{n}\gamma)^{12}\text{C}$ reaction, with 3 to 7 MeV deuterons interacting with a thick ^{11}B target [7, 10]. In addition to the two discrete gamma rays (see above), the reaction yields a broad spectrum of fast neutrons; e.g., a 6 MeV deuteron beam yields an almost continuous neutron spectrum, with energies of up to ~18 MeV [7, 10]. Narrow (ns) pulsed deuteron beam would permit neutron-energy selection by Time-Of-Flight (TOF) [9].

In parallel to the ongoing R&D of a fast neutron and gamma-ray radiation source, there have been intense ongoing developments of fast-neutron and gamma imaging detectors. The demands from fast-neutron and gamma detectors used for these purposes can be defined as follows: (a) large area ($>20\times 160\text{ cm}^2$), (b) high detection efficiency ($>10\%$) for both, fast-neutrons and gammas, (c) spatial resolutions of 5-10 mm, (d) good discrimination between gamma-rays and neutrons, (e) high counting rate capability ($>10^5\text{ counts}/(\text{sec}\cdot\text{cm}^2)$) and (f) neutron spectroscopy in the range of 2-10MeV (with energy resolution of ~500 keV at 8MeV) and ability to discriminate between two discrete gamma-ray energies (4.43 MeV and 15.1 MeV) used in this application.

The detectors developed to date encompass scintillation-screens viewed by fast gated intensified cameras; e.g. the TRION and TRECOR systems combining solid-scintillator screens and intensified CCD cameras (developed by Soreq NRC and PTB-Braunschweig colleagues) [11, 12] yielded promising results [13]. Such systems are

capable of simultaneously capturing several images, each at different neutron energy and in principle, by adding another high Z scintillator [14], also gamma-ray images - allowing for combined neutron/gamma inspection of objects with mm-size spatial resolution. The fast- neutron detection efficiency varies between 30%, for 2MeV neutrons, and 8% for 14MeV neutrons [11]. Another group uses Cherenkov detectors for the gamma-ray detection [15]. In the above approaches the neutron and gamma-ray images are taken separately, either by sequential scanning or by positioning the different detectors one behind the other. This approach necessitates precise positioning and alignment of the neutron and gamma-ray data for reconstruction. In addition, the high cost of large-area imagers of this type, required for an operational container screening system, would add significantly to the price of the system.

In our research we focus on the development of a novel detector concept for combined imaging and spectroscopy of fast-neutrons and gamma rays, efficiently and simultaneously in the **same detection medium**. It encompasses a LXe scintillator, contained within “fiber-like” capillaries of a suitable bulk material (e.g. Tefzel [16]) (see scheme in Figure 1). The scintillation-light within the capillaries, induced by neutron or gamma interactions with Xe atoms (resulting in nuclear or electron recoils, respectively), propagates along the capillaries by total internal reflection and is detected by a position-sensitive gaseous photomultiplier (GPM) [17] through a UV-transparent window. The photoelectrons, induced by photon conversion on a CsI photocathode deposited on the top electrode of the GPM, are multiplied by successive gas avalanche multipliers, e.g. cascaded Thick Gas Electron Multiplier (THGEM) electrodes [18, 19, 20, 21] (see Figure 1). The localization of the interacting fast-neutron or gamma-photon in the LXe converter is derived from the center-of-gravity (COG) of all event-emitted photons detected by the GPM.

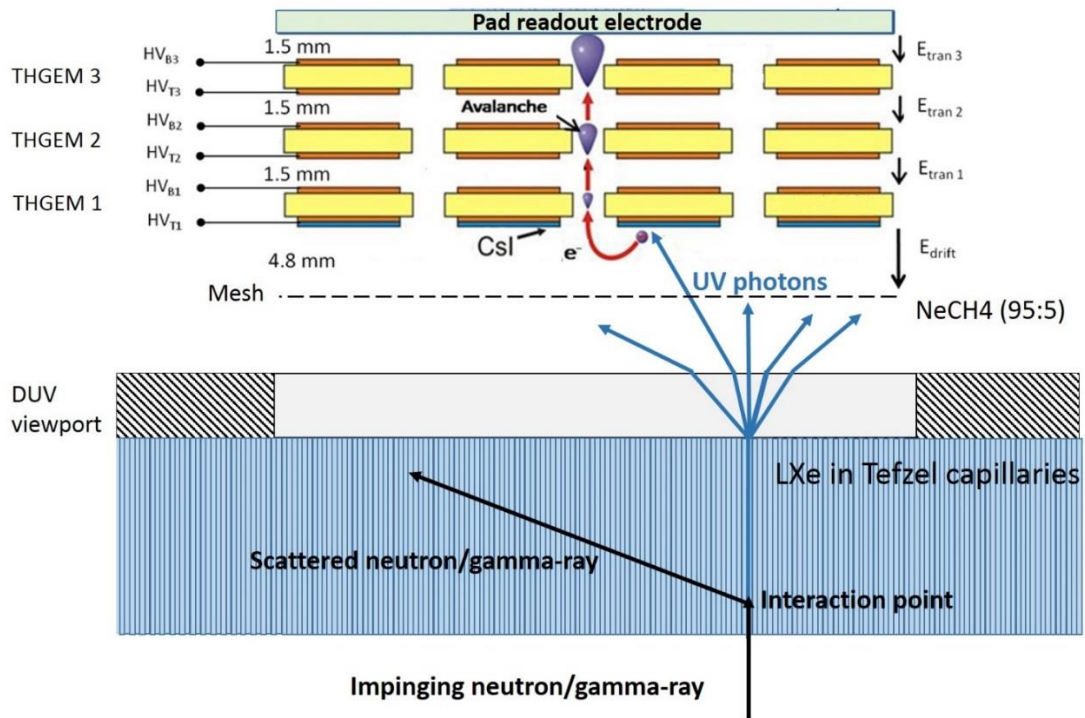


Figure 1: Schematic drawing of the combined gamma & fast-neutron imaging detector concept. The interaction of radiation with LXe (plain volume or here - within capillaries) induces a fast UV scintillation-light flash. These UV photons are detected by a gaseous photomultiplier (GPM) having a reflective CsI photocathode deposited on a gas-avalanche electron multiplier – here a triple-THGEM; the latter has a segmented readout anode. The LXe sensitive volume and the GPM (operating in a “counting gas” (here Ne/5%CH₄)) are separated by a UV-transparent quartz window.

2 Liquid xenon as a detection medium

Liquid noble gases are known to be excellent detection media due their high density, homogeneity and large scintillation yield [22, 23, 24]. They are transparent to their own scintillation light, easily expanded to large detector masses and they provide both radiation-induced ionization and scintillation signals. The main characteristics of the liquid noble gases are shown in Table 1 as a general guideline only. Among liquid rare gases, liquid xenon has the highest stopping power for penetrating radiation, thanks to its high atomic number ($Z = 54$) and density ($\rho = 2.94 \text{ g/cm}^3 @ 165 \text{ K}$). It also has the highest ionization and scintillation yields; the latter are comparable to that of NaI(Tl) but with a faster time response. It has no long-lived isotopes and has the highest boiling point, which make it the one of the preferred detection media.

Table 1: Main characteristics of noble gases in their liquid state: atomic number, boiling point at 1atm, liquid density at boiling point, ionization yield, scintillation yield and scintillation wavelength.

	Z (A)	BP at 1 atm [K]	Liquid Density at BP [g/cm^3]	Ionization Yield [electrons/keV]	Scintillation Yield [photons/keV]	Scintillation Wavelength [nm]
He	2 (4)	4.2	0.13	39	15	
Ne	10 (20)	27.1	1.21	46	74	78 – 85
Ar	18 (40)	87.3	1.4	42	40	125
Kr	36 (84)	119.8	2.41	49	25	145
Xe	54 (131)	165	3.06	64	46	178

LXe is an excellent electrical insulator, having a band structure analogous to semi-conductors, with a band-gap of 9.22 eV, corresponding to its ionization potential [25]. When energy is deposited in the medium by an interacting particle the electrons of the valence-band cross the band-gap to the conduction band - consequently inducing a detectable signal. This makes this noble liquid a prime candidate for use as a detection medium in a large variety of detectors used in particle physics, nuclear medicine, astrophysics and for the direct detection of dark matter (WIMPS) [22, 23, 24]. In this chapter the mechanisms of ionization and scintillation signals generation in liquid xenon will be described.

2.1 Thermodynamic properties of xenon

Figure 2 shows the phase diagram of xenon. It is in a liquid state at a relatively small temperature interval for pressures below 2 bar ($\sim 18^\circ\text{C}$, from 180 K to 162 K, at 2 bar and $\sim 4^\circ\text{C}$, from 166 K to 162 K, at 1 bar). Higher pressures are not practical for our application due to mechanical limitations in large systems (i.e. the UV-windows of the photon detector).

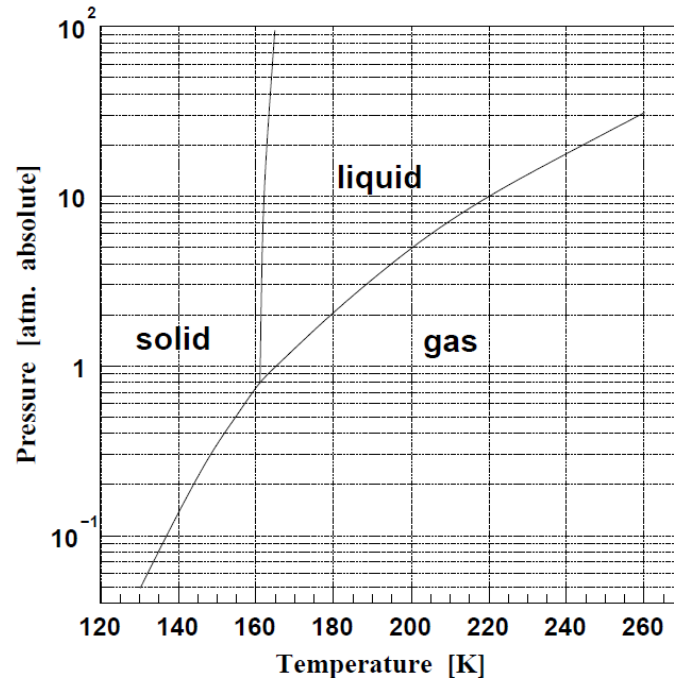


Figure 2: Phase diagram for xenon (taken from [22]).

2.2 Interaction modes of radiation with liquid xenon

2.2.1 Charged particles

Charged particles interact with the electrons and nucleus of LXe atoms via electromagnetic coupling. The electronic and nuclear stopping powers, for incident alpha particles, protons or electrons, are shown in Figure 3A. The figure shows also the contribution of the electronic and nuclear stopping power, for alphas and protons, and collisional and radiative stopping power for electrons [26]. For high energy particles and for electrons the nuclear stopping power can be neglected when compared to the electronic stopping power. For incident electron interactions with the medium, the resulting bremsstrahlung radiation emission can be important when compared to the electronic stopping power. The incident charged particle will then transfer its energy

mainly to the electrons of xenon atoms, inducing two types of interactions: either ionization or excitation of the xenon atoms. The range of alpha particles, protons and electrons in xenon, as a function of the energy of the particle, is shown in Figure 3B. I.e the range for 5.5 MeV alpha particles in LXe (of liquid density 2.94 g/cm^3) is $\sim 45 \mu\text{m}$ [27].

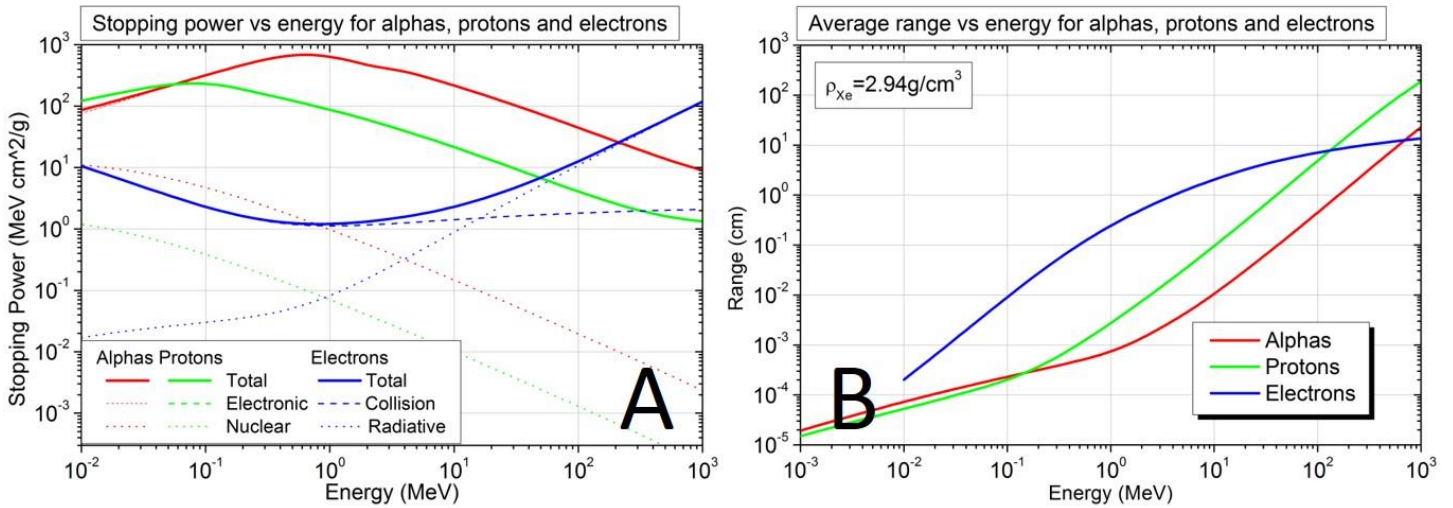


Figure 3: A- Total stopping power (in $\text{MeV}\cdot\text{cm}^2/\text{g}$) for alpha particles, protons and electrons in xenon versus energy. B- Range (in cm) for alpha particles, protons and electrons in liquid xenon for a liquid density of 2.94 g/cm^3 , versus particle energy [26].

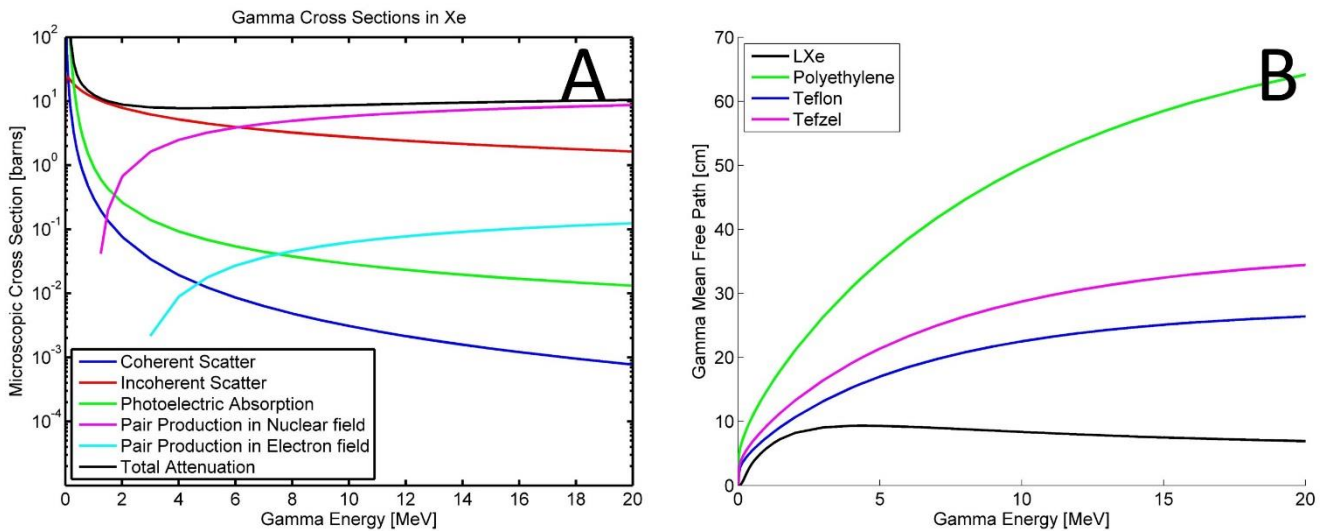


Figure 4: A- Gamma's cross sections in natural Xe for energies up to 20 MeV. B-Mean free path of gamma-rays in various radiation-converter materials (LXe, Polyethylene (C_2H_4), Teflon (C_2F_4) and Tefzel ($\text{C}_4\text{F}_4\text{H}_4$)). Calculated from data taken from [28].

2.2.2 Gamma-ray and x-ray interactions

Differently from charged particles, photons such as x-rays or gamma-rays in the energy range of 0-15 MeV, interact with matter mainly by photoelectric effect, Rayleigh (coherent scattering) effect, Compton (incoherent scattering) effect and pair production.

The photoelectric effect is the total absorption of the incoming photon by an electron of the xenon atom. It results in an ejection of an electron, with a kinetic energy equals to the energy difference between that of the incoming photon and the electron binding energy, leaving the atom ionized. For low photon energies this effect is dominant.

The Compton Effect is inelastic, incoherent, scattering of the incident photon on a weakly-bound electron of a xenon atom. The electron absorbs a certain amount of energy from the photon and is ejected from the atom. The photon is then scattered in a different angle with a lower energy obeying Equation 1, where $\Delta\lambda$ is the difference between the photon's wavelength after and before scattering.

Equation 1

$$\Delta\lambda = \frac{h}{m_e c} (1 - \cos\theta)$$

In the pair or triplet production interaction an electron–positron pair or an electron–electron–positron triplet is created in the vicinity of an atomic nucleus or electron, respectively. The energy threshold for pair production is at least twice the electron's rest mass, or 1.022 MeV, while the energy threshold for triplet production is at least four times the electron's rest mass or 2.044 MeV.

Gamma-interaction cross sections in LXe are shown in Figure 4A for energies up to 20 MeV [28]. The dominant processes above 2 MeV are Compton scattering and pair production. Both produce energetic electrons or electrons/positrons. Above ~7 MeV pair production becomes dominant. The total gamma cross section of ~15 barn, in the relevant energy range (0-20MeV) - assures high gamma conversion efficiency (>20%) in a few cm thick LXe converter.

Figure 4B shows the gamma-ray mean free path in LXe, as well as in optional capillary's materials (i.e. Teflon (C_2F_4), Tefzel ($C_4F_4H_4$) or Polyethylene ($(C_2H_4)_nH_2$). The latter were investigated (by GEANT4 simulations) aiming at finding converter configurations with improved localization resolution and detection efficiency (see details in section 5.2). The mean free path in LXe is much shorter than in the light capillary-materials considered. Hence, the gamma's mean free path in the converter will be influenced mainly by LXe.

2.2.3 Neutrons

Neutrons interact with the target's nucleus mainly by scattering, absorption or production of multiple lower energy neutrons ($n,2n$).

Neutron scattering (elastic or inelastic) by target's nucleus involves the change of velocity and direction of the neutron while the nucleus is left with the same number of protons and neutrons. In inelastic scattering the nucleus may recoil and may be left in an excited state, leading to a later emission of radiation. In single elastic events, the neutron-induced target nuclei recoils, with energy E_r , determined by the kinematics according to [29]:

Equation 2

$$E_r = E_n \frac{4A}{(1+A)^2} \cos^2\theta$$

Where E_n is the incoming neutron energy, A is the mass of the target (for natural Xe $A \sim 131$) and θ is the scattering angle, of the recoil nucleus, in the laboratory coordinate system. According to Equation 2, one can infer that in general, low mass elements like hydrogen or helium, are more efficient at slowing down neutrons. In a single elastic collision with Xe nucleus the neutron can transfer not more than about 3% of its energy to Xe. However, neutrons may scatter more than once in the LXe volume. These “multiple-scattering” events have a variety of scattering angles and, therefore, deposit a wider range of energies than a single elastic scatter.

In inelastic scattering, the nucleus undergoes an internal rearrangement into an excited state from which it eventually decays releasing gamma-ray radiation. The

energy deposited by this radiation will add to the total energy deposited by the neutron in the target. The total kinetic energy of the neutron and nucleus is less than the kinetic energy of the incoming neutron.

In the neutron absorption or capture reactions, the nucleus will rearrange its internal structure by emitting other particles: one or more gamma rays, protons or alpha particles. The nucleus may also emit one, two or three excess neutrons and finally a fission event may occur creating two or more fission fragments and additional neutrons [30].

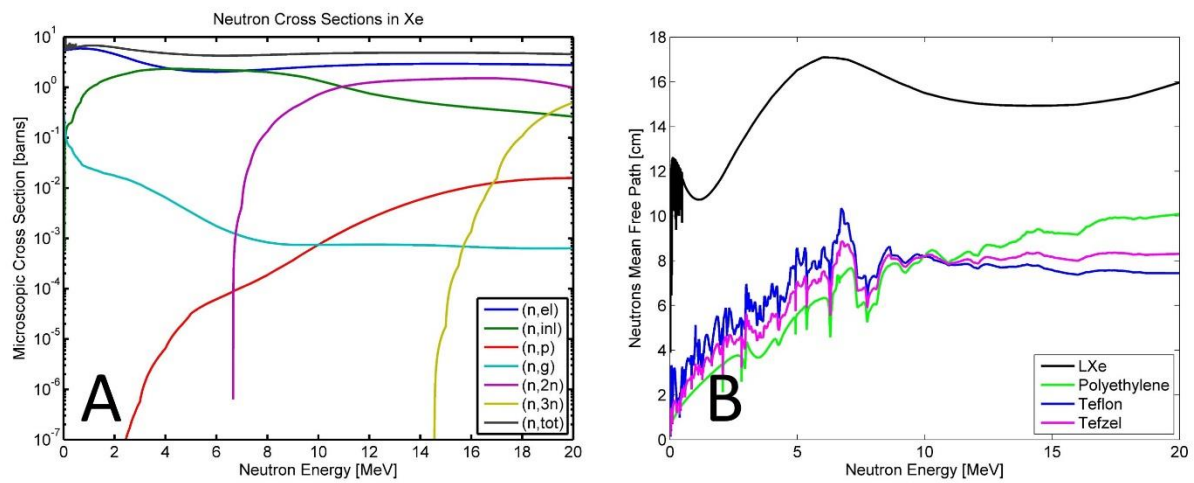


Figure 5: A- Neutron's microscopic cross sections in natural Xe for energies up to 20 MeV. In figure A, (n,el) stands for neutron elastic scattering, (n,inl) neutron inelastic scattering, (n,p) neutron-proton reaction, (n,g) neutron capture reaction, (n,2n) and (n,3n) neutron-2 neutrons and neutron-3 neutrons reaction and (n,tot) stands for the total cross section. B-Mean free path of neutrons in the various radiation-converter materials (LXe, Polyethylene (C_2H_4), Teflon (C_2F_4) and Tefzel ($C_4F_4H_4$)). Calculated from data taken from [31].

Neutron's cross sections in natural Xe (considering the natural abundances of each of the main xenon isotopes: 1.91% ^{128}Xe , 26.4% ^{129}Xe , 4.07% ^{130}Xe , 21.2% ^{131}Xe , 26.9% ^{132}Xe , 10.4% ^{134}Xe and 8.86% ^{136}Xe) are shown in Figure 5A for energies up to 20 MeV [31]. The prominent neutron interactions with Xe, in this energy range, are elastic and inelastic scattering. Much less probable but still important for energy deposition in LXe are neutron capture and (n,p) reactions. Neutron capture is followed by emission of energetic gamma-rays. The energy deposited by these gammas will add to the total energy deposited by the neutron in LXe, leading in some cases to an overall deposited energy higher than the incident neutron energy. Neutron capture is more

probable for incident neutrons in the 2 MeV range than for neutrons with energies above 4 MeV (see (n,g) at Figure 5A)).

LXe elastic scattering cross section of a few barns for fast-neutrons in the relevant energies (2-20MeV) - assures high neutron conversion efficiency (>20%) with a few cm thick LXe converter.

Figure 5B shows the neutron mean free path in LXe, along with the mean free path in the considered Hydrogen-rich capillary's materials. Although the dimensions of our prototype LXe converter ($\varnothing \sim 100$ mm) are smaller than the neutron mean free path in LXe, there is a small probability for multiple neutron scattering within the converter volume. The neutron's mean free path in all of the shown light materials, is shorter than in LXe. Hence, incorporating capillaries made of these materials within the LXe converter will increase the probability of interaction and lead to an efficient energy deposition of neutrons closer to their impinging point. In this manner, the neutron's spatial resolution may improve.

The resonances in Figure 5B occur at incident neutron energies which are close to the energy of an excited state of the compound nucleus [30].

2.3 Ionization and excitation

The average energy required for creating an electron – ion pair in liquid xenon is higher than its ionization potential, I , of 9.22 eV. Considering E_0 as the energy transferred to the xenon by the incident particle and N_i as the average number of electron-ion pairs created, the average energy W required for creation a pair can be defined as:

Equation 3

$$W = \frac{E_0}{N_i}$$

The difference between W and I , is due to the different modes of energy transfer to the medium - mainly ionization and excitation. For the case of incident electrons this can be expressed by Equation 4 [32].

Equation 4

$$E_0 = N_i \langle E_i \rangle + N_{ex} \langle E_{ex} \rangle + N_i \langle \epsilon \rangle$$

where $\langle E_i \rangle$ is the average energy required to ionize an atom, N_i is the average number of ionized atoms, $\langle E_{ex} \rangle$ is the average energy required to excite an atom, N_{ex} is the average number of excited atoms and $\langle \epsilon \rangle$ is the average energy of sub – excitation, below which the incident electrons interact only through elastic collisions with the atoms, transferring part of their kinetic energy. Combining Equation 3 and Equation 4, the average energy required to create an electron – ion pair, can be written as:

Equation 5

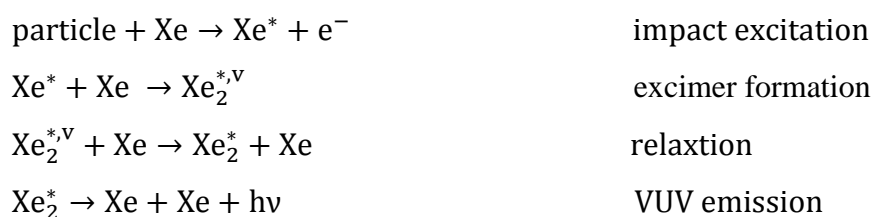
$$W = \langle E_i \rangle + \frac{N_{ex}}{N_i} \langle E_{ex} \rangle + \langle \epsilon \rangle$$

The value of W was determined to be 15.6eV for LXe [33, 34]. Nevertheless, the actual number of electron – ion pairs created per unit energy deposited in the medium is dependent on the type of ionizing particle and its energy and is different for gaseous and LXe.

2.4 Scintillation – recombination and de-excitation

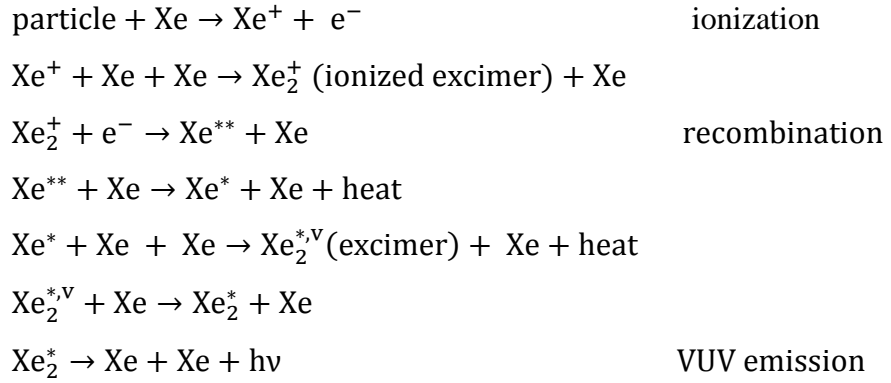
The process of luminescence in liquid xenon due to the passage of radiation involves the formation of diatomic excited molecules formed primarily by two channels [23].

The first is through excitation of xenon atoms by the primary particle or secondary electrons, forming strongly bound diatomic molecules in the excited state or “excimers”:



The superscript v is used to distinguish excited states with vibrational excitation ($\text{Xe}_2^{*,v}$) from purely electronic excitation with $v = 0$ (Xe_2^*).

The other channel for VUV luminescence is through ionization of xenon atoms, induced by the primary particles or secondary electrons, followed by recombination of the positive xenon ions as described by the following processes:



The excimers formed in both processes emit VUV light of the same wavelength. After recombination, the formed excimer is left in either one of the two lowest electronic excited states $^3\Sigma_u^+$ or $^1\Sigma_u^+$ and emits scintillation photons due to the transitions to the repulsive ground state $^1\Sigma_g^+$. These two transitions ($^3\Sigma_u^+$ to $^1\Sigma_g^+$ and $^1\Sigma_u^+$ to $^1\Sigma_g^+$) are spectroscopically indistinguishable but their decay times are significantly different as explained in the following section.

The emission spectrum of liquid xenon is centered around $\lambda=178$ nm, corresponding to a photon energy of 7eV, with a full-width-half-maximum (FWHM) value of ± 2 nm [35, 36].

2.5 Temporal components of scintillation

The recombination process, with associated photon emission, occurs within few picoseconds after ionization/excitation of the atoms of the liquid. Each of the $^3\Sigma_u^+$ or $^1\Sigma_u^+$ excited states has a different decay time to the ground state, making it possible to distinguish several components of the scintillation events:

- A fast component due to de-excitation of the $^1\Sigma_u^+$ state, with decay time τ_f .

- A slow component due to the de-excitation of the $^3\Sigma_u^+$ state, with decay time τ_s .
- A component due to the slower (when compared to the excimer de-excitation times) recombination process, with a time constant of τ_r .

The decay times are summarized in table 2 for incident alpha-particles, electrons and fission fragments [37, 38].

Table 2 – Summary of scintillation time constants of liquid xenon induced by fast electrons, by alpha particles and by fission fragments. τ_f , τ_s and τ_r are the decay times of the fast, slow and recombination components, respectively. (Data taken from [37, 38])

Incident Particle	τ_f (ns)	τ_s (ns)	τ_r (ns)
Electrons (0.5MeV<E<1MeV)	2.2±0.3	27±1	34
Alphas	4.3	22	
Fission fragments	4.1	21	

The direct transition from the $^3\Sigma_u^+$ excited state to the ground state is forbidden but becomes possible owing to the spin-orbital coupling with state $^1\Pi_u^+$. This leads to rather long decay times of the order the ~20 ns. For the case of incident alpha particles the density of the ionized and excited species along the particle track is much higher than with fast electrons, leading to much faster recombination. Experimentally, no ~30 ns recombination component of scintillation has been observed in liquid xenon with alpha particles. Figure 6 (taken from [38]) shows the scintillation light decay curves in liquid xenon induced by electrons, alpha particles and fission fragments. The strong particle-type dependence of the decay of the scintillation light makes it possible to discriminate electrons from heavier particles by pulse-shape analysis.

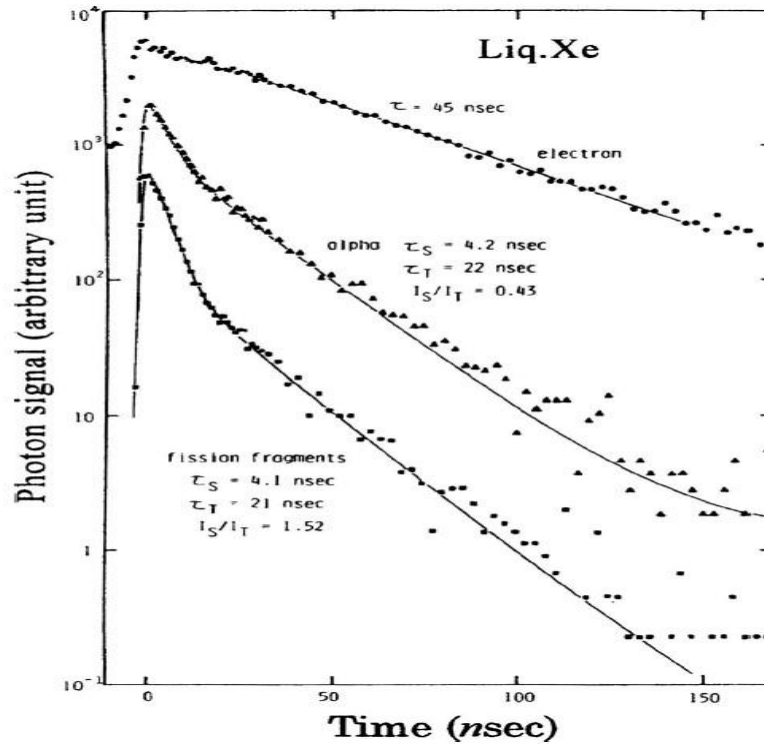


Figure 6: Liquid xenon scintillation light decay curves induced by electrons, alpha particles and fission fragments (figure taken from [38]).

2.6 Scintillation and ionization yield

The scintillation-photons yields in the noble liquid depend on the radiation type and on the presence of an electric field. A comprehensive analysis of the existing data for γ -ray and neutron induced scintillation in LXe are presented in [39]; these authors also developed a simulation model consistently describing most of the available datasets [40]. Based on their model, Figure 7 shows the light and charge yields induced by electron recoil events, for a gamma-ray interacting with LXe, and for nuclear (Xe) recoil events, as a function of both energy and electric field within the noble-liquid volume.

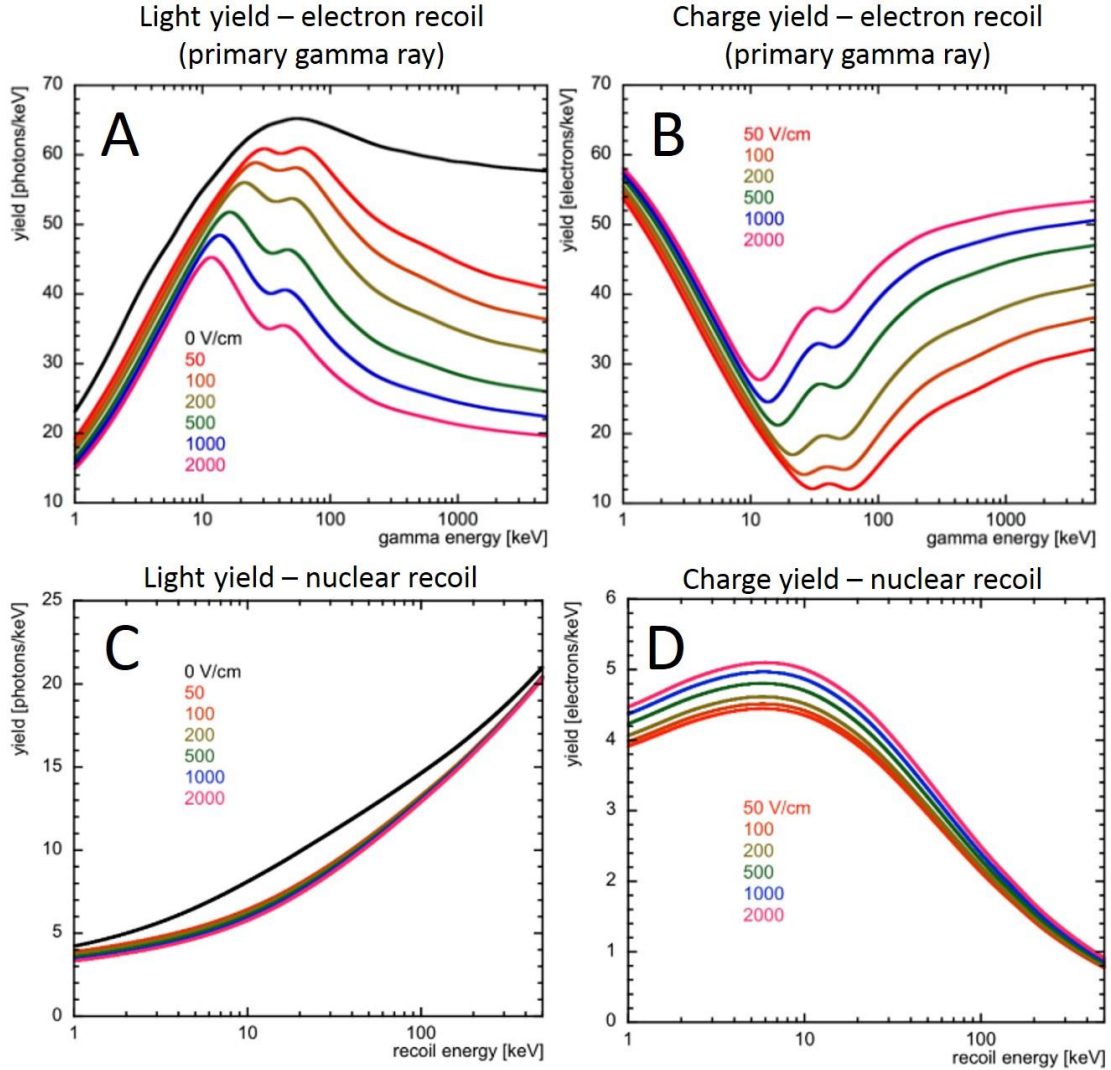


Figure 7: The simulated light (photons/keV, left) and charge (electrons/keV, right) yields of electron recoil events for gamma ray interaction with liquid xenon (figures A and B), and of nuclear-recoil events (figures C and D), as a function of both energy and electric field. (Taken from [40]).

Higher electric fields applied within the liquid reduce recombination, increasing the charge yield at the expense of light, in an anti-correlated fashion. The dip in the gamma-ray curves is caused by xenon K-edge x-rays that create secondary possible interaction sites, displaced from the initial interaction location (energy deposition). The turn-over in the nuclear recoil charge yield curve is caused by the decrease in the total number of quanta (as described by the Lindhard factor [41]) beginning to dominate over the increase in the charge yield resulting from the decreasing Thomas-Imel recombination probability [42] (a smaller total number of ions is being created). Discussion, and more details, of measurements of light and charge yields can be found in [40].

3 Cesium iodide photocathodes and gaseous photomultipliers

3.1 Cesium iodide photocathodes

Cesium iodide (CsI) photocathodes has good quantum efficiency (typical value of ~25% at 175 nm [43]) in the VUV region of the electromagnetic spectrum (100 nm to 200 nm); although being hygroscopic its production is relatively simple and it is significantly more stable than other types of photocathodes such as bi-alkali or multi-alkali ones. It is stable over time in vacuum and under dry gas circulation, when deposited on adequate substrates – e.g. on gold-plated printed-circuit detector readout boards [43,44].

The UV-photon detection with a CsI-based GPM [45] relies on the external photoelectric effect where photons with energy above a certain threshold interact with the photosensitive material (within a certain depth). This generates mobile charge carriers that are ejected from the photocathode surface into vacuum or gas medium in a so-called photoemission process. The fraction of charges extracted into a gas medium (dictating the effective QE value in a GPM) depends on the electric field at the CsI surface and on the gas type – as discussed below. The extracted charges are multiplied by a gas-avalanche multiplier - in this work a triple-THGEM (Figure 1), generating a measurable current pulse.

In semiconductors, like cesium iodide, the photoelectrons resulting from the photoelectric effect are mostly emitted from the valence band with a maximum energy, E_k , given by:

Equation 6

$$E_k = hv - (E_g + \chi)$$

where hv is the photon energy, E_g is the energy bandgap from the top of the valence band to the conduction band and χ is the electron affinity of the specific material – which is the energy gap from the conduction band minimum to the vacuum energy level. From literature it can be established that for CsI, due to experimental uncertainties, there is quite a significant scatter around the most probable values for E_g , χ and the energy threshold for photoemission, $E_t \equiv E_g + \chi$. Combining data from several

authors [46, 47, 48] it can be established that for CsI $E_g=6.0$ eV, $\chi=0.2$ eV and $E_t=6.2$ eV.

The external photoelectric effect occurring in CsI photocathodes can be described by Spicer's Three-Step model [49, 50], which treats the electron photoemission in terms of three successive steps (see Figure 8):

- 1) Optical absorption of a photon into the bulk of the photocathode leading to the liberation of electrons into the bulk,
- 2) The motion of the electrons through the bulk of the crystalline structure of the photocathode towards its surface, and
- 3) Escape of the electrons from the photocathode's surface (only if their energy is greater than the vacuum level).

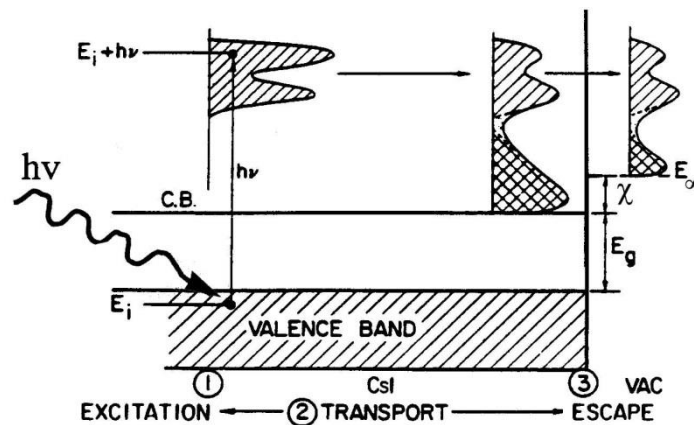


Figure 8: Representation of Spicer's Three-Step model (taken from [50]).

The Three-Step model provided the means of understanding photo-emitters, and more generally it has been found to describe photoemission from all solids, besides that it gave the possibility of estimating the photo-yield (photoelectrons per photon) as a function of photon energy. A more sophisticated development of this model by Berglund and Spicer [51] gives the energy distribution of the emitted photoelectrons. To determine the basic equation for the quantum yield of a photocathode in the frame of the Three-Step model it is necessary to recognize the excitation of photoelectrons as a consequence of a bulk absorption effect [49]. Photons hitting the photocathode will transverse a certain thickness of material before being absorbed, meaning that the light intensity I after traversing a thickness x of material is given by:

Equation 7

$$I(x, hv) = I_0(hv) \cdot (1 - R(hv))e^{-\alpha(hv) \cdot x}$$

where $I_0(hv)$ is the initial intensity of photons, $R(hv)$ is the photocathodes' surface reflectivity and $\alpha(hv)$ is the photocathodes' absorption coefficient, as a function of incident photons' energy, hv . The amount of light absorbed at a distance x from the photocathodes' surface can then be given by:

Equation 8

$$dI(x) = I_0 \cdot (1 - R)e^{-\alpha(hv) \cdot x} \cdot \alpha \cdot dx$$

Some of the excited electrons induced by the absorbed light will then travel to the surface and escape originating from a layer x to $x+dx$. The contribution $di(x)$ from the layer x to $x+dx$ to the quantum efficiency or yield can then be expressed by:

Equation 9

$$di(x) = P_{0\alpha}(hv, x, dx) \cdot P_T(hv, x) \cdot P_E(hv)$$

where $P_{0\alpha}(hv, x, dx)$ is the probability of exciting electrons above the vacuum energy level in the layer x and $x+dx$, or the "absorption probability," $P_T(hv, x)$ is the probability that electrons reach the surface with sufficient energy to escape, or "transport probability" and $P_E(hv)$ is the probability of escape of electrons reaching the surface, or "escape probability". Where $P_{0\alpha}(hv, x, dx)$ is given by:

Equation 10

$$P_{0\alpha}(hv, x, dx) = \alpha_{PE}(hv) \cdot I(x)dx = \alpha_{PE}(hv) \cdot I_0(1 - R)e^{-\alpha x} dx$$

Where α_{PE} represents the part of the photoelectrons that have energy higher than the vacuum energy level and have the possibility to escape and R is the photocathodes' surface reflectivity. It can also be shown that [49]:

Equation 11

$$P_T(hv, x) = e^{-\left(\frac{x}{L(hv)}\right)}$$

Where $L(h\nu)$ is the electron scattering length, since the electron scattering probability is proportional to the distance traveled. This way, for $di(x)$, we have:

Equation 12

$$di(x) = \alpha_{PE} \cdot I_0(1 - R)e^{-\alpha x} \cdot e^{-\left(\frac{x}{L}\right)} \cdot P_E(h\nu)dx$$

The quantum efficiency, or photo-yield, for a given wavelength can be defined as the ratio between the number of emitted photoelectrons to that of impinging photons (by integration of Equation 12 between 0 to ∞).

Equation 13

$$QE = \frac{\int_{x=0}^{x=\infty} di}{I_0} = \frac{\alpha_{PE} P_E}{\alpha} (1 - R) \frac{1}{1 + \frac{l_\alpha}{L}}$$

where α is the photocathodes' absorption coefficient, $l_\alpha = 1/\alpha$ is the absorption length, l_α/L is the ratio of absorption length to scattering length and α_{PE}/α is the fraction of electrons excited above the vacuum level, which normally increases monotonically as $h\nu$ increases above the threshold for emission ($E_t=6.2$ eV, for CsI). From this expression it can be observed that in order to maximize the quantum efficiency then $l_\alpha \ll L$, meaning that a large fraction of the photo-excited electrons contribute to the yield, and that α_{PE}/α and P_E should be close to unity.

Evaporation and characterization of CsI photocathode are described in details in section 8.1 of the appendices.

In a GPM, after being emitted from the photocathode, there is a probability for the PE to backscatter by gas molecules back to the photocathode surface. This probability depends on the electron energy and scattering cross-sections in the specific gas-mixture. The probability of the PE to escape (without backscattering) is called photoelectron extraction efficiency. The photoelectron extraction efficiencies from CsI into CH_4 , CF_4 , Ne/CF_4 , Ne/CH_4 and Ar/CH_4 as function of the drift field, were measured by several authors, using a UV lamp (185 nm peak) [52, 53, 54], and are shown in Figure 9. Estimations for the extraction efficiencies as a function of the

electric field for Ne/CH₄, Ar/CH₄ and Ne/CF₄ for few gold coated-THGEM electrode geometries are brought in section 8.2 of the appendices.

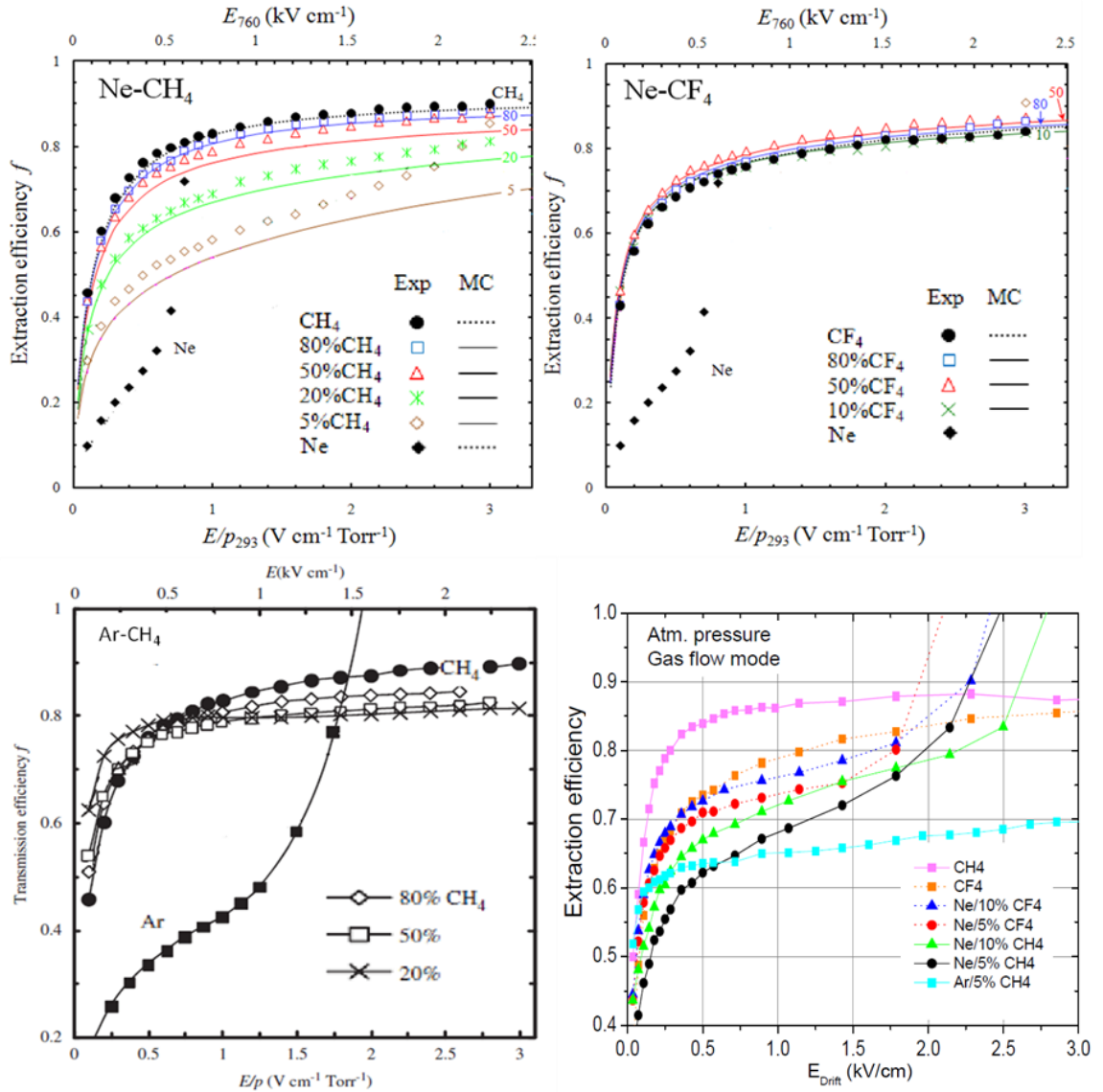


Figure 9: Photoelectron extraction efficiency from CsI into CH₄, CF₄, Ne/CF₄, Ne/CH₄ and Ar/CH₄ (atmospheric pressure) as function of the drift field using a UV lamp (185 nm peak). Data taken from [52, 53, 54].

3.2 Gas Electron Multipliers and Thick Gas Electron Multipliers

In gaseous photomultipliers (GPM) employing solid photocathodes, the emitted photoelectrons are drifted within the gas to an electron multiplier electrode, or a series of cascaded electrodes, where avalanche multiplication occurs due to a high applied electric field. The GPMs ability to operate under high magnetic fields while operating at atmospheric gas pressure allows constructing large-area, flat and thin detectors to cover large detection areas [55].

A significant part of the R&D effort on gaseous photomultipliers has shifted from "wire chambers" towards the so-called "closed geometry" electron multipliers - more specifically to hole-type micro-patterned structures. Previous generations of GPMs with electron multipliers relying on multi-wire proportional chambers (MWPCs) [56], parallel-plate avalanche chambers (PPACs) [57] or resistive-plate chambers (RPCs) [58], in which the electron avalanches occur in an "open geometry", suffered photon- and ion-mediated secondary avalanches; these resulted- in gain limitation and reduced photon detection efficiency and imaging properties. Hole-type electron multipliers, like the GEM [59, 60], the THGEM [18, 21, 61], the Micro-Hole-and-Strip Plate (MSHP) [62, 63] or the Thick -COBRA [64] were proposed for the charge multiplication in GPMs [17, 65, 66], aiming at reducing photon- and ion-feedback effects by screening in single and cascaded configurations. The GEM and the THGEM structures are represented in Figure 10, along with dimensions. The electron multiplication occurs within the holes. The operation principle of a GPM based on GEMs or THGEMs is also depicted in Figure 10: a reflective photocathode is deposited on the top electrode of the first element of the electron multiplier cascade, the photoelectrons are focused into the holes where charge multiplication occurs; the avalanche electrons drift towards the next multiplier elements, for further multiplication; the final avalanche-charge is recorded on a pixilated 2D readout electrode.

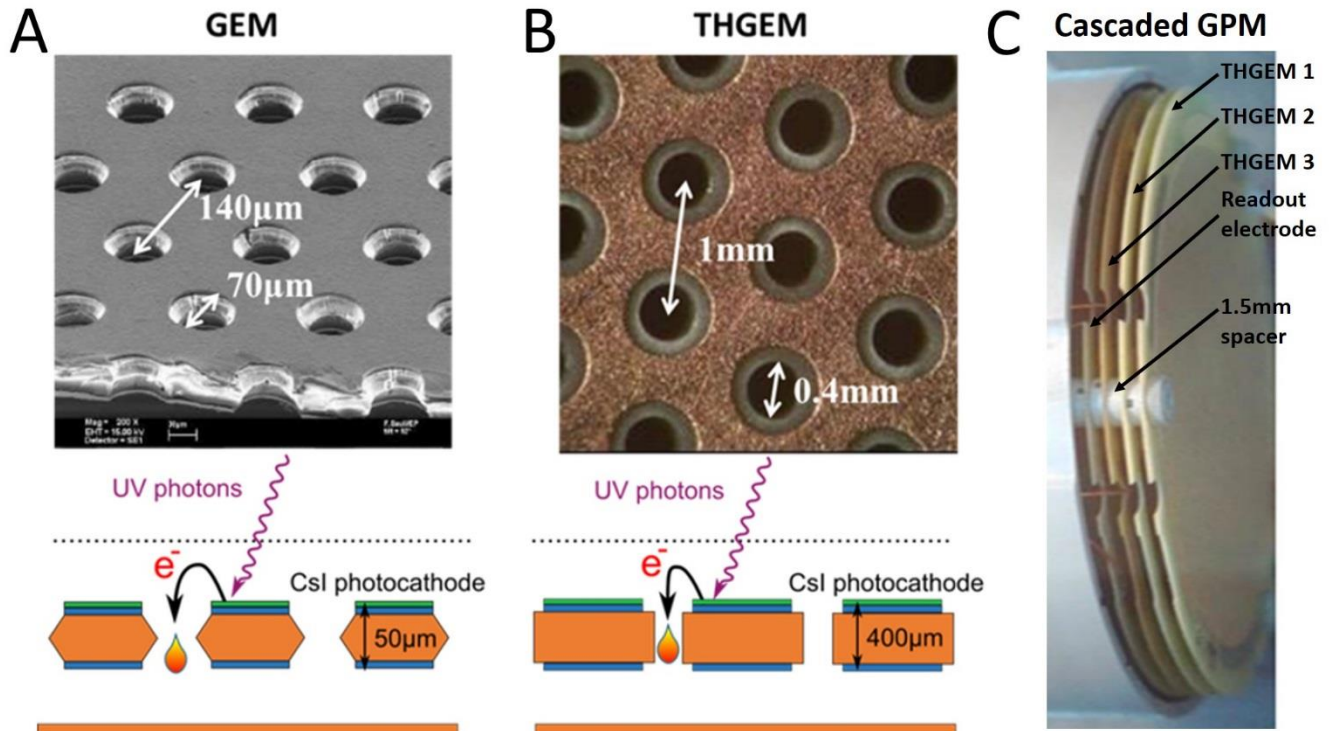


Figure 10: Representation of the GEM (figure A) and the THGEM (figure B) with a CsI photocathode for UV photon conversion. Photoelectrons are multiplied by an avalanche occurring within the holes. Figure C shows a picture of cascaded GPM comprises three THGEMs separated by 1.5 mm spacers and followed by a readout electrode.

In GEM detectors the charge multiplication occurs within micro etched holes (usually 50 μm in diameter) on a thin double-sided metal-clad insulator (typically 50 μm polyimide), due to a high electric field applied between both faces. Typically these structures are arranged in a cascaded configuration (e.g. Figure 10C); in cascaded-GEM GPMs, the first electrode is coated with a reflective CsI photocathode. It was shown that these GPMs can be operated with a single photon sensitivity regime (gains $>10^5$) [17, 67 and references therein].

The thick gas electron multiplier (THGEM) shown in Figure 10B is similar to a GEM but with ~ 10 -fold expanded dimensions, with an hexagonal arrangement of sub-millimeter holes, mechanically drilled through a printed-circuit board-like (PCB) material with a double-sided copper clad. Following the drilling process, a small rim is chemically etched in the copper around the holes, to reduce discharge probability. The holes are typically 0.4 mm in diameter and the thickness of the PCB-like material is 0.4 or 0.8 mm. The THGEM operation principle is similar to that of a GEM; a high electric potential applied between both electrode faces creates a strong electric field within the

holes. the emerging dipole field attracts the photoelectrons, that are amplified in the high-field region in the hole. Signals are recorded usually on a readout anode. THGEM electrodes are very robust, compared to GEM, both electrically and mechanically. They can be mass-produced, at relatively low-cost, over large areas (presently $>1\text{m}^2$).

THGEM-based multipliers and gas photomultipliers are presently being intensively investigated by numerous groups for applications in room-temperature (calorimetry [68], neutron imaging [69], Cherenkov Ring Imaging [70, 71]) and in cryogenic conditions, for photons and charge detection in noble-liquid detectors [45, 72, 73, 74, 75], for neutrino physics [76], dark matter searches [77], medical Compton camera [78, 79], Homeland Security [92, 80, 81 and references therein]. Except the large-area cryogenic LEM (THGEM-like) detectors developed for dual-phase LAr TPCs in neutrino experiments [76] and the large-area RT UV-GPMs for RICH [71], most detector prototypes have been small in size and served so far as a proof of concept purposes for liquid argon or liquid xenon detectors.

3.2.1 Photo-detection efficiency of a GPM

The single-photon photo-detection efficiency of a CsI-coated THGEM GPM (PDE_{GPM}), operating in a gas medium depends on the CsI QE (Equation 13), the effective area of the photocathode (not covered by holes) (A_{eff}), the extraction efficiency of photoelectrons into the gas mixture (ϵ_{extr}), the single-photoelectron collection efficiency into the THGEM holes (ϵ_{coll}) and the probability of detecting an incoming photon signal above electronic noise ($\epsilon_{\text{S/N}}$) [52].

Equation 14

$$PDE_{\text{Det}} = QE \cdot A_{\text{CsI}} \cdot \epsilon_{\text{ext}} \cdot \epsilon_{\text{col}} \cdot \epsilon_{\text{S/N}}$$

The reference value of the CERN-RD26 collaboration for CsI QE at 175 nm is $\sim 25\%$ [43]. A typical value of A_{eff} is 0.77 and a typical value of the overall extraction efficiency ($\epsilon_{\text{extr}} \cdot \epsilon_{\text{coll}}$) is 0.6-0.8 (see Figure 81 in appendix 8.2). Assuming $\text{prob}(\text{signal}>\text{noise})=0.95$ for sufficiently high gain and low-noise electronic, the PDE_{Det} would be 11-14%. Note that further decrease of the PDE_{Det} occurs due to the

transmission of photons through the window ($t_w=0.90$) and through the mesh ($t_m=0.85$) of the GPM.

4 Experimental setup and methodology

4.1 LXe cryostat

The experiments were conducted using the Weizmann Institute Liquid Xenon system (WILiX) [82], comprising a super-insulated cryostat, a gas handling and purification system, and a 250-liter xenon gas storage/recovery reservoir (see Figure 11 and Figure 12). The cryostat, shown schematically in Figure 13A, comprises of a 510 mm diameter \times 390 mm high outer vacuum chamber (OVC) and a 157 mm diameter \times 81 mm high stainless steel inner vacuum chamber (IVC). Experiments were carried out either with a plain-volume LXe radiation converter-scintillator or with a converter consisting of \sim 5500 Tefzel capillaries (outer diameter (OD)=1.6 mm, inner diameter (ID)=1.0 mm, length=70 mm, see Figure 13B) filled by LXe. Tefzel was selected because it is a highly hydrogen-enriched polymer, with good reflectivity properties in the UV (similar to Teflon). Hydrogen largely improves the spatial resolution for neutrons by more efficient transfer of the neutron energy near the point of neutron interaction [83], resulting in a factor of 3 better position resolution compared to plain LXe converter.

Xenon gas introduced into the IVC condenses on the finned end of a temperature-controlled copper cold finger, thermally connected to the Brooks Automation PCC J-T cryocooler (maximum cooling power 28 W at 128 K). A Cryo-con Model 24C temperature controller is used to control the temperature of the cold finger, with a control loop of a Pt100 temperature sensor and a 50 W cartridge heater. LXe droplets forming on the cold finger are funneled towards the IVC wall. The liquid fills the Tefzel capillaries from below, up to a quartz window viewed by the GPM, and siphoned out through a commercial parallel-plate heat exchanger (GEA model GBS100M). Xenon gas flowing out of the heat exchanger passes through a mass-flow controller (MKS model Mass-flow 1479A) to a double-diaphragm recirculation pump (KNF model N143SV.12E), through a SAES MonoTorr hot getter model PS4-MT3 and then returns to the IVC through the heat exchanger in which \sim 95% is re-liquefied (see Figure 11). The Xe flow rate was 3.5 standard liters per minute (slpm) — the nominal flow rate of the getter.

In order to minimize the heat exchanges between the IVC and the exterior, the OVC is evacuated by a turbo–molecular vacuum pump followed by rotary scroll pump, to a vacuum of $\sim 10^{-5}$ Torr. To improve thermal insulation, the IVC was wrapped by several layers (>10) of a super insulator (thin aluminized Mylar foils, sandwiched with insulating fabric sheets) absorbing infra-red radiation.

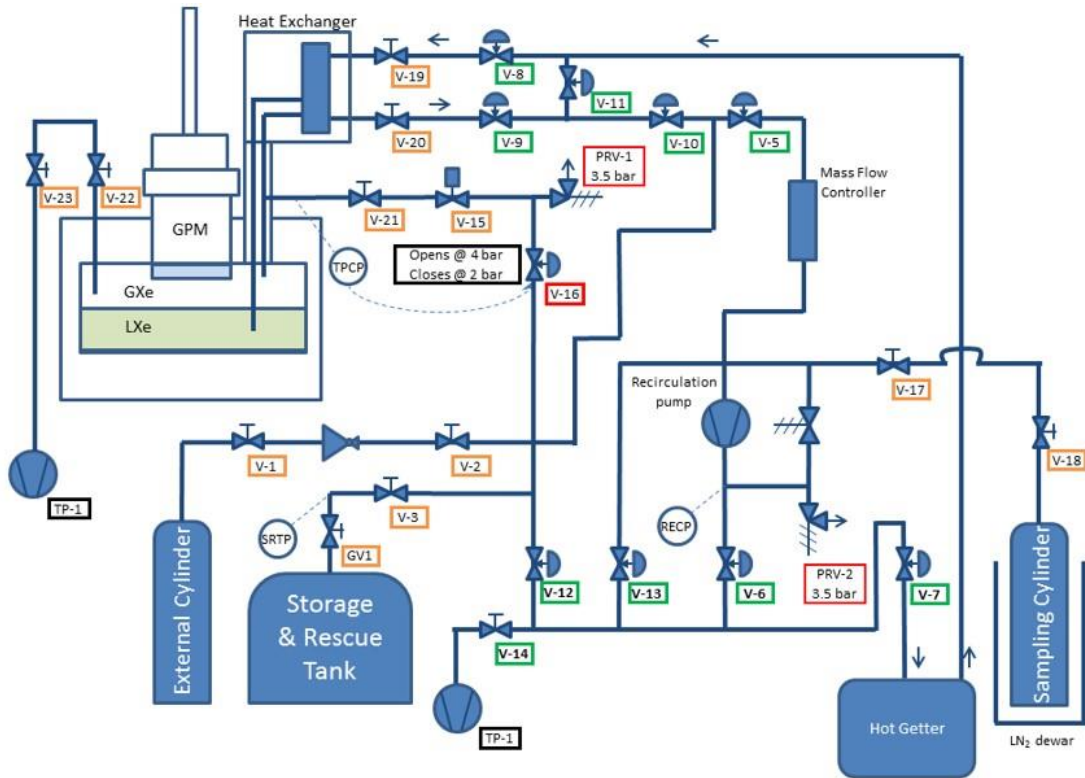


Figure 11: Schematic diagram of the Xe purification and recirculation system.

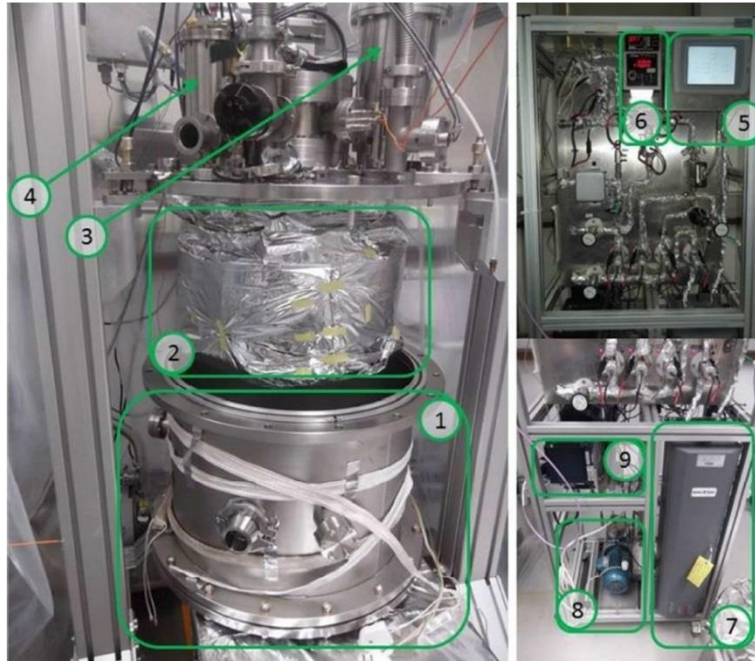


Figure 12: 1) Outer Vacuum Chamber (OVC, shown open in the picture), 2) Inner Vacuum Chamber (IVC) wrapped with a super insulator, 3) Heat Exchanger, 4) PCC cryocooler housing, 5) Gas system control screen, 6) OVC, IVC pressure gauges and xenon flow regulator, 7) xenon gas purification system (SAES MonoTorr Purifier), 8) KNF double diaphragm circulation pump and 9) process variable acquisition and control rack.

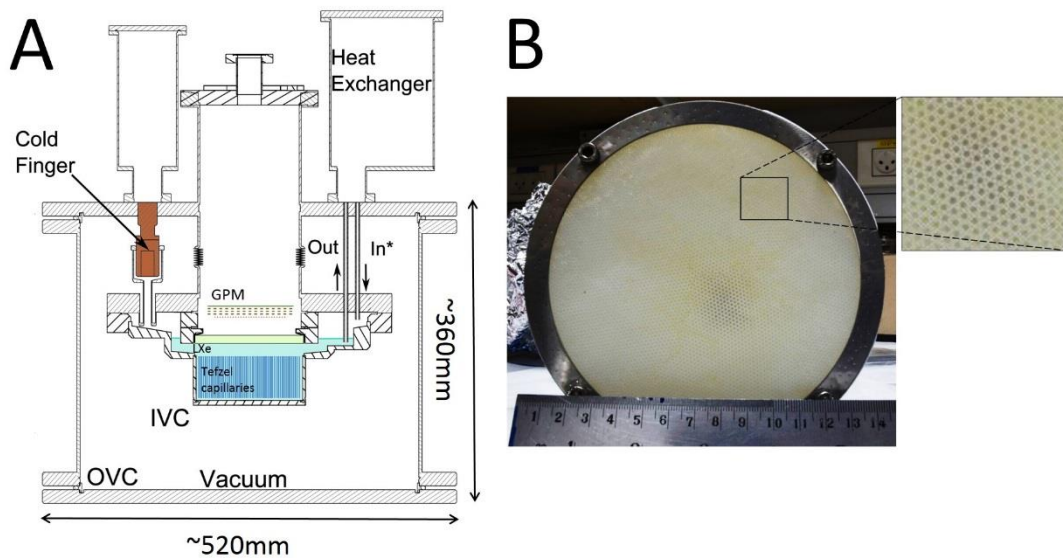


Figure 13: Figure A: Schema of WILiX, including the GPM assembly. Figure B: Radiation converter composed of ~5500 Tefzel capillaries (OD=1.6mm, ID=1.0mm, length=70mm) assembled in a Teflon holder. The Tefzel capillaries are immersed within LXe and viewed by the GPM.

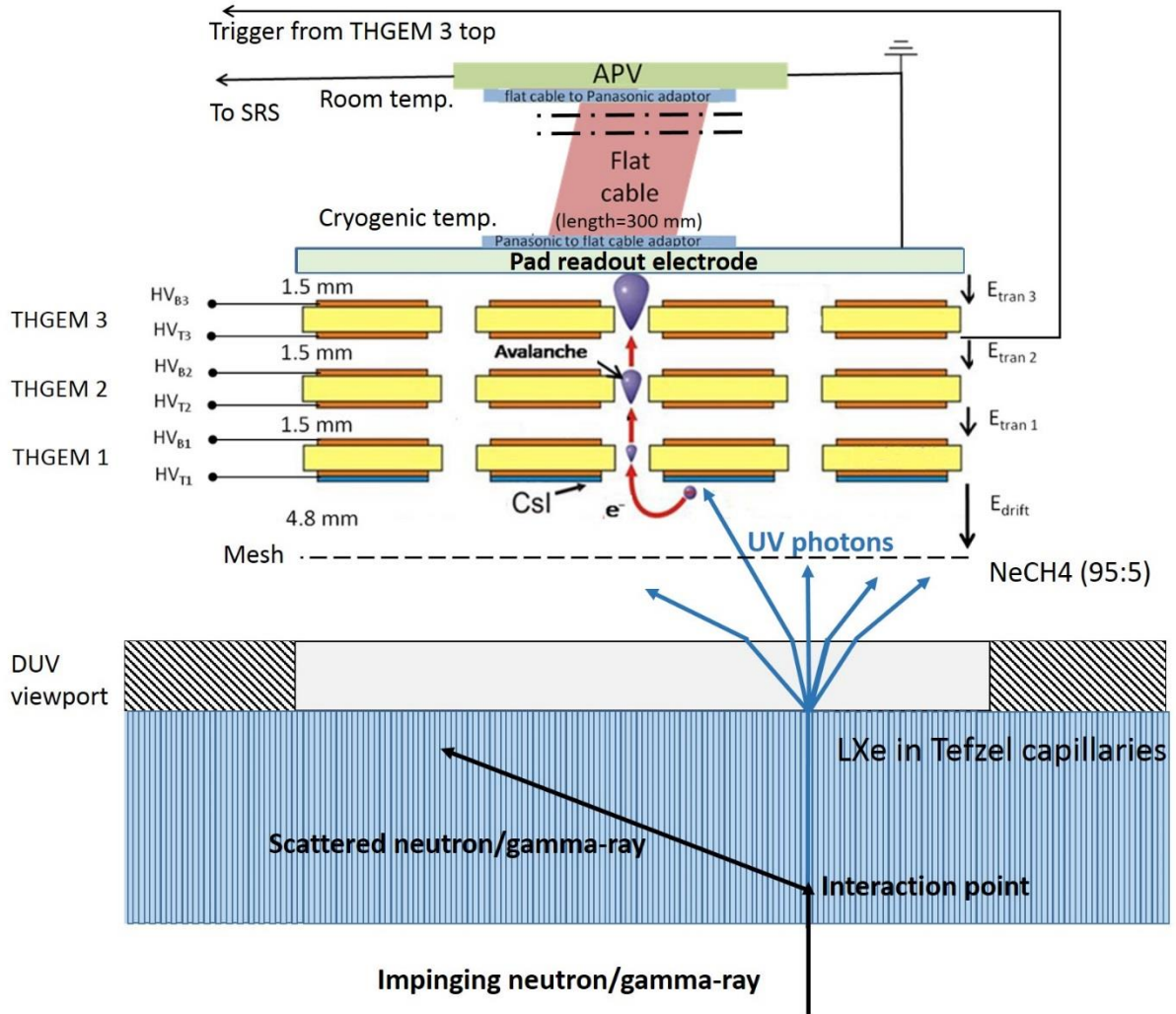


Figure 14: Schematic view of the GPM setup; a cascade of 3 THGEM electrodes, the top one coated with a reflective CsI photocathode, followed by a 2D readout electrode. Signals from individual pads are transmitted through a flat cable into an APV hybrid chip, processed with SRS electronics (see text).

4.2 Cryogenic GPM

The GPM setup, shown schematically in Figure 14, consisted of a cascaded structure of three THGEM electrodes, with a CsI photocathode deposited on the first, followed by a segmented readout electrode comprising 61 hexagonal pads (see layout and pad dimensions in Figure 15). Details about evaporation and characterization of cesium iodide photocathode are brought in 8.1 in the appendices. The GPM was viewing the converter through a DUV-grade fused silica viewport (clear diameter 136.7 mm, MPF part number: A0650-7-CF).

In the current experimental setup, the CsI photocathode was located 32 mm away from the LXe converter. In retrospect, better resolution results would have been

achieved with smaller distance between the photocathode and the converter (see paragraph 5.3.5).

The 0.4 mm-thick THGEM electrodes, Cu-clad and Au-plated on both sides, were made of FR4 with an active diameter of 100 mm; the holes were arranged in a hexagonal pattern, with a hole diameter $d = 0.4$ mm, pitch $a = 0.8$ mm (between hole centers) and an etched hole rim $h = 50$ μm . The Cu layer thickness (after etching) was 64 μm . The THGEM electrodes were produced by ELTOS SpA, Italy. The final processing stages, including gold-plating, cleaning and baking were done in the CERN MPGD workshop. The THGEM electrodes were tested for leak current and discharge "hot-spot" prior to installation in the GPM (see 8.3 in the appendices). The transfer gaps between the stages, as well as the induction gap between the last THGEM and the segmented readout electrode were 1.5 mm wide. Each of the THGEM faces, as well as the mesh mounted 4.8 mm from THGEM1, had separate HV bias, provided through low-pass filters by CAEN type N471G HV power supplies.

The GPM was operated along this study with Ne/5%CH₄ at a gas flow of 20 sccm, at pressures ranging from 356 to 485 torr and a typical temperature of 210 K. Ne/CH₄ was chosen because it provides both a high gas gain at relatively low voltages [84] and high photoelectron extraction efficiencies from the CsI photocathode [52, 85]. The GPM pressure control was done by pumping the GPM gas output and a proportional valve connected to a mass flow controller (MKS model 247B) and a baratron pressure gauge (MKS model 121A-16303, serial: 016123793) and MKS controller (type 250). The relatively low operating pressure, as well as the low CH₄ concentration (5%), were chosen as they allowed for a lower discharge rate compared to the conditions used in [45], namely a pressure of 356 torr with Ne/20%CH₄. We attribute this change in stable conditions to the accumulation of discharge history on the particular THGEM electrodes used for the same studies.

The voltage applied to the THGEM electrodes was asymmetric in all cases, with equal voltages across the second and third stages and with the highest possible voltage across THGEM1 to maximize the photoelectron extraction efficiency from the photocathode [52] and to improve the overall stability. The transfer and induction fields were kept at 0.5kV/cm in all conditions; the GPM was operated in a flow mode (20 sccm) or in sealed mode.

The quantum efficiency (QE) of the particular CsI photocathode used in this study was measured to be 22% at 175 nm before transferring it from the evaporation system to the GPM, and 8% after unloading it from the GPM, seven months later. The degradation in QE was likely the result of water outgassing from the top part of the GPM chamber (Figure 13), which was at room temperature throughout the experiment (while the photocathode temperature was ~ 210 K).

4.3 Readout electronics and typical signals

The segmented readout electrode contained 61 hexagonal pads (see layout and dimensions in Figure 15A). Hexagonal pads, and not conventional square pads, were chosen since they provide the most efficient and compact division of the round surface available with equal sided polygons [86]. Each of the 6 mm (pad-border length) pads was connected to an individual channel of the front-end hybrid APV 25 chip [87], via a Panasonic header connector (type: AXK6SA3677YG) (see Figure 15B) mounted on the pad electrode. Although the APV25 chip has 130 available channels we decided to use only 61 pads in this prototype. The APV25 chip was not designed for cryogenic temperature operation (~ 200 K); therefore, the pad signals were transferred to a remotely-placed APV 25 chip through a 30 cm long ribbon flat cable (3754/80 80 conduct 0.64 mm pitch) using two dedicated PCB adaptors (see Figure 16A): 1. Panasonic-to-flat cable adaptor, using a PCB with Panasonic socket AXK5SA3277YG and SBH41-NBPB-D17-ST-BK connectors, and 2. Flat cable-to-Panasonic adaptor, using a PCB with Panasonic header (type: AXK6SA3677YG) and SBH41-NBPB-D17-ST-BK connectors. The flat cable (placed inside the GPM gas vessel) was wrapped with a thin Cu ground-shielding foil and an Al foil. The APV25's ground was well connected to the electrode ground by Copper braid. The APV25 chip was connected to the external SRS (Scalable Readout System [88]) via a 1 m-long homemade vacuum-rated micro-HDMI-to-HDMI cable and feedthrough. Triggers for the SRS system were extracted from the top THGEM3 electrode (see Figure 14) through a coaxial cable into a Canberra 2006 charge sensitive preamplifier located outside the GPM chamber. These trigger signals were shaped by a timing filter amplifier (Ortec model 474) followed by leading edge discriminator (PS model 730) and then fed into the SRS trigger input.

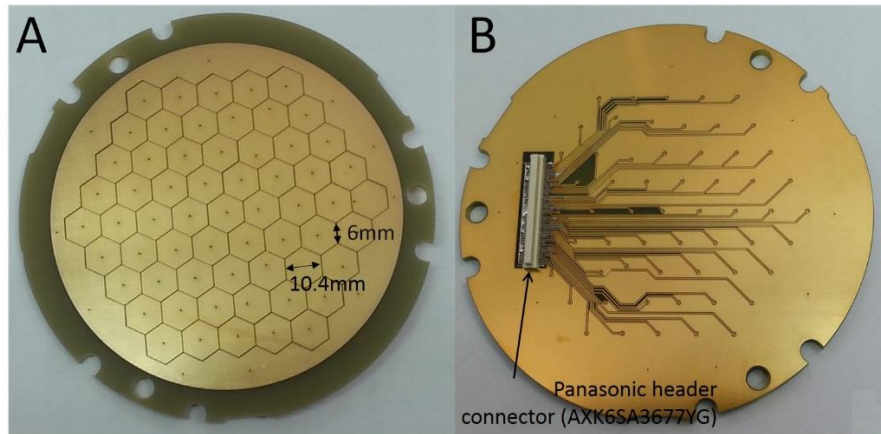


Figure 15: Segmented 61 pixel hexagonal-pad readout, top (A) and bottom (B). Pad side is 6 mm and its width is 10.4mm. The pitch between the pads is 0.2mm.

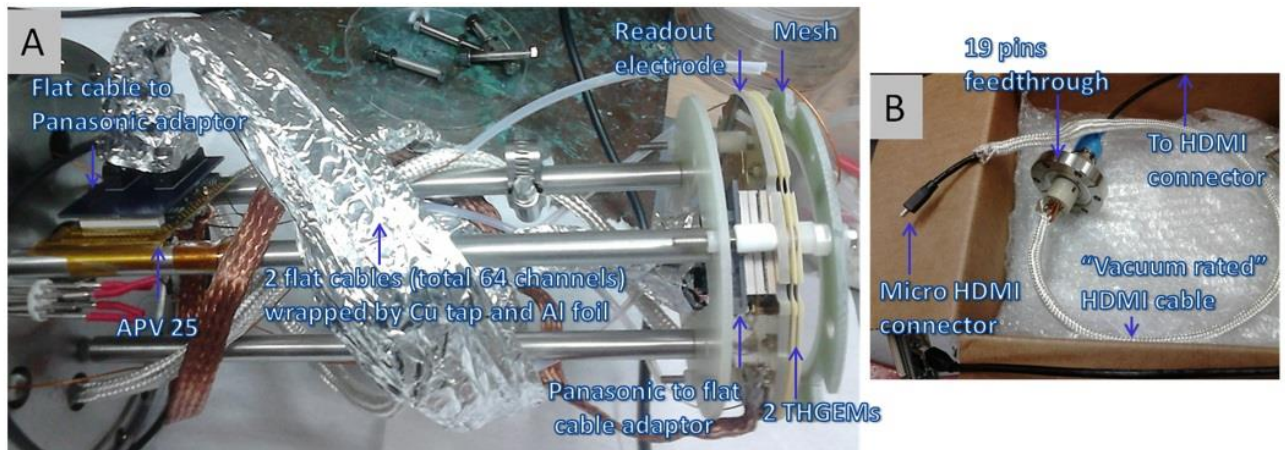


Figure 16: A- Picture of the GPM detector (although only two THGEMs are shown here, the experiments were performed with three THGEMs). B- Picture of the micro-HDMI to HDMI feedthrough.

The SRS electronics permits saving, for each event, the charge collected in each pad, enabling offline analysis. Typical charge spectra, in each of the 61 readout pads, are shown in Figure 17: A) electronic noise and B) ^{60}Co gamma-rays. One can set a threshold on the charge (charge threshold) and check, event by event, how many pads exceeded this threshold. In a similar way one can set a threshold on the number of "firing" pads (pads threshold), and for example exclude events with lower number of "firing" pads (for improving resolution, but at the cost of losing some detection efficiency).

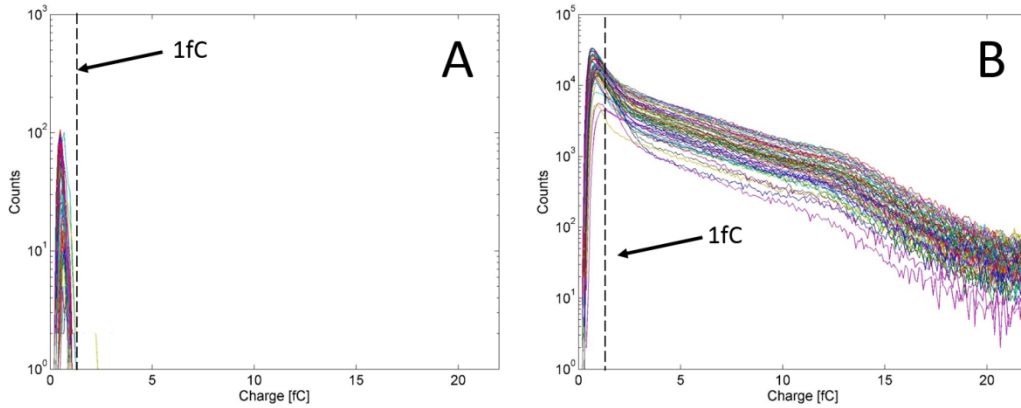


Figure 17: The charge spectrum, measured on each of the 61 readout pads. (A) Electronic noise and (B) gamma-rays from ^{60}Co . The gain in this measurement was 4×10^4 .

A typical *single event*, as measured in the hexagonal pads electrode, is shown in Figure 18 for various scenarios. In these figures the color bar represents the charge in each pad in fC. The charge depends on the number of PEs and on the gain. Note that the figures were measured with different gains ($\sim 0.6\text{-}4 \cdot 10^4$).

- Figure 18A: The GPM irradiated with a narrow X-ray from ^{55}Fe , pointing to the central pad. X-ray photons interacting with NeCH_4 gas, yielded a few microns range photoelectrons; these were multiplied by the cascaded-THGEM; and as a result, only the central pad got a signal.

- Figure 18B: The GPM irradiated by hydrogen pulsed UV-lamp through a window ($\phi=38\text{mm}$). UV-induced photoelectrons from a ~ 40 mm diameter CsI area are multiplied by the cascaded THGEM, inducing signals in multiple pads. The number of pad hits is a function of the initial number of UV photons per pulse.

- Figure 18C: An ^{241}Am α -source located inside the GPM vessel; the source irradiated the detector perpendicularly to its axis, ionizing the NeCH_4 gas within the drift gap (between the drift mesh and the first THGEM). The alpha-particles were stopped within a few centimeters in the gas, and the resulting ionization electrons were multiplied by the THGEM, inducing signals on several pads along the alpha track. Note the higher-ionization Bragg peak at the end of the track.

- Figure 18D: An ^{241}Am α -source immersed within the LXe volume (without capillaries), viewed by the GPM through a window (\emptyset 36mm). The large number of alpha-induced scintillation photons yielded ~ 250 photoelectrons/event - multiplied by the THGEM cascade and resulting in signals on most of the pads.

- Figure 18E: External irradiation, with ^{60}Co gamma source, of LXe-filled Tefzel capillaries. Gamma-ray induced electrons in LXe deposit only part of their energy within the active volume. Alternatively, gamma-ray interacting with the capillary material would create predominantly Compton electrons; some of them reach the active LXe volume, leaving there part of their energy. Total internal reflection within the capillaries, guides part ($\sim 15\%$) of the radiation-induced scintillation photons towards the photocathode; the extracted PEs are multiplied by the THGEM cascade.

- Figure 18F: External irradiation, with $^{241}\text{AmBe}$ neutron/gamma source, of LXe-filled Tefzel capillaries. Gamma-rays, emitted from the source may induce electrons in LXe or capillaries (as explained for Figure 18E). Neutrons, emitted from the source, can transfer small amount ($> \sim 3\%$) of their energy to Xe nucleus in a single elastic collision. Furthermore, energy transfer, up to the neutron's original energy, may occur in inelastic neutron collisions in which the induced gamma-rays may be absorbed and deposit their energy in the LXe. Alternatively, neutrons interacting with the capillary material may lose large fraction of their energy, in a single collision, by knocking out a proton; some of them reach the active LXe volume, leaving there part of their energy. Total internal reflection within the capillaries, guides part ($\sim 15\%$) of the radiation-induced scintillation photons towards the photocathode; the extracted PEs are multiplied by the THGEM cascade.

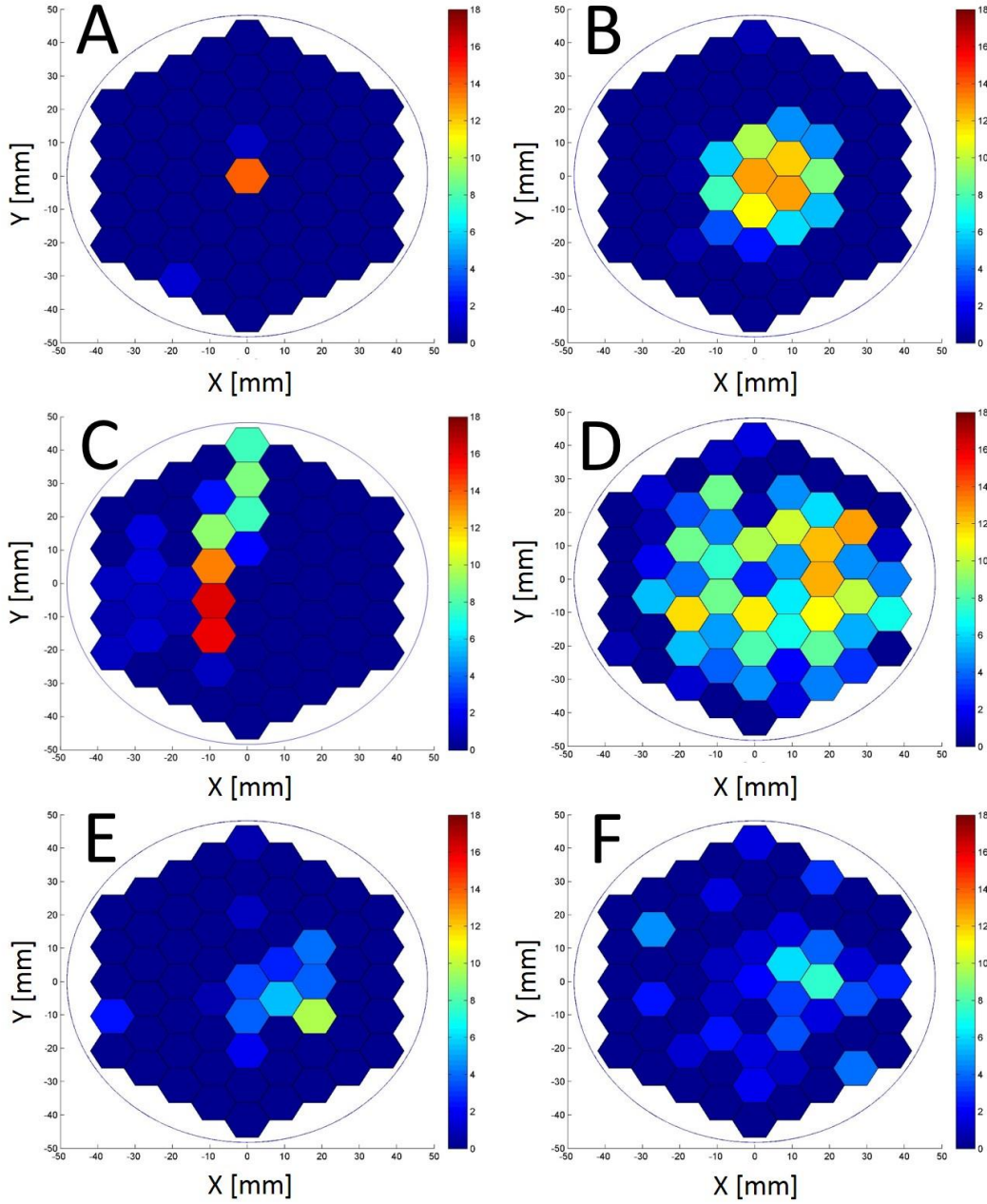


Figure 18: Typical single events, as measured with the hexagonal pad electrode. Color bar represents the charge in each pad in fC. A: Irradiating the GPM with a narrow X-ray from ^{55}Fe , pointed to the central pad. B: Hydrogen UV-lamp illuminating the GPM through a window ($\phi=38\text{mm}$). C: An ^{241}Am α -source within the GPM vessel, located on the detector's side (red pads indicate the Braag peak at the tracks end). D: An ^{241}Am α -source, immersed in the LXe volume (without capillaries) and viewed by the GPM through a window ($\phi=36\text{mm}$). E: An external ^{60}Co gamma source, irradiating the LXe-filled Tefzel capillaries. F: An external $^{241}\text{AmBe}$ neutron/gamma source, irradiating the LXe-filled capillaries. The measurements were done with the GPM operated at different gains ($\sim 0.6\text{-}4 \cdot 10^4$) in $\text{Ne}/\text{CH}_4(95:5)$.

For imaging, the COG of the "firing" detector's readout pads was calculated, event-by-event, according to Equation 15. Then, a 2D histogram of the COG values was plotted. In Equation 15, \vec{P}_j is a $[x,y]$ position vector of the center of pad j and $Q_{i,j}$ is the charge collected in pad j in event i . Similar equation was used for imaging

simulations while in this case $Q_{i,j}$ denoted the number of PEs arriving to pad j in event i . Note that in cases, with small numbers of PEs in each pad ($< \sim 3\text{PE}/\text{pad}$), calculating the simple un-weighted COG, by setting $Q_{i,j}=1$, would avoid artifact bias of the COG due to the large standard deviation of the exponential distribution of the avalanche process.

$$\text{Equation 15} \quad \overrightarrow{COG}_i = \frac{\sum_{j=1}^{j=61} \overline{P}_j \cdot Q_{i,j}}{\sum_{j=1}^{j=61} Q_{i,j}}$$

In addition to the COG histogram simulated with an object, another one was simulated without an object (flat image). The ratio image is calculated according to Equation 16, and indicates the transmission of the incident radiation through the object. The ratio image corrects for the non-homogeneity of the detector response vs. point of interaction.

$$\text{Equation 16} \quad \text{Ratio} = \frac{\left(\frac{\text{Image}_{object}}{\text{Number of impinging}_{object}} \right)}{\left(\frac{\text{Image}_{flat}}{\text{Number of impinging}_{flat}} \right)}$$

4.4 Setup for point-like UV-photon imaging (GPM only) at room temperature

Prior to cryogenic operation, the spatial resolution of the GPM with its pad readout was tested at room temperature in a dedicated chamber outside of the LXe cryostat. The detector was illuminated through a fused-silica window, (clear diameter 38 mm) by a point-like UV source (spontaneous-discharge H₂ lamp). The number of photons per pulse (from one to several thousands) was set using a series of ORIEL optical filters (nominal optical densities of 0-4.5) placed in front of the lamp, down to a single-photon level. The number of photoelectrons per UV flash was derived from the pulse-height spectra recorded by the GPM. The trigger to the SRS electronics was provided by the electrical discharge pulse of the lamp.

The measurements were done twice; once with a double-THGEM GPM while not maintaining a constant extraction efficiency, by changing the field on the first THGEM, and then with a triple-THGEM GPM while maintaining a constant extraction efficiency

4.5 Setup for gain measurements

The gain of a THGEM is proportional to $\exp(E/\rho)$, where E is the electric field in the THGEM holes and ρ is the gas density. The gas density is a function of temperature and pressure. Decreasing gas density would increase the THGEM gain but also increase the discharges probability. Gain measurements in pulse mode, with 3-THGEM GPM installed in WILiX, were performed at room and cryogenic temperatures with Ne/5%CH₄, aiming at finding a stabile (in terms of discharges rate), high gain, working point. A DC D₂ lamp shined UV light through a fused silica window near the top of the GPM port. The lamp provided single-UV photons at a rate of a few hundred Hz that reached the CsI photocathode by reflection from the chamber walls. The voltage applied to the THGEM electrodes was asymmetric in all cases, with equal voltages across the second and third stages and with the highest possible voltage across THGEM1 to maximize the photoelectron extraction efficiency from the photocathode [52] and to improve the overall stability. The transfer and induction fields were kept at 0.5kV/cm in all conditions; the GPM was operated in a flow mode (20 sccm) or in sealed mode.

Furthermore, gain curve (current mode) and extraction efficiencies in He/CF₄ and He/CH₄ mixtures were also investigated [89], only at room temperature, since they may present a possible alternative to Ne-based mixtures for potential higher gains, with lower applied voltages and lower costs. In these measurements, a 1000Å CsI photocathode was deposited on the top of a gold plated THGEM electrode. Photoelectrons were extracted from the CsI film by incident 185 nm VUV photons emitted by an Oriel Hg(Ar) VUV lamp.

The extraction efficiency experimental setup is shown in Figure 21A. In these measurements the photoelectron currents were measured operating the photocathode in vacuum and in the gas. Then, the ratio $I_{\text{gas}}/I_{\text{vacuum}}$ was calculated for various He/CF₄ and He/CH₄ mixtures as a function of the electric field applied in the region above the photocathode.

The experimental setup for the gain measurements is shown in Figure 21B. A mesh, mounted 6 mm from the THGEM top, and THGEM top had the same bias. The potential on the THGEM bottom set the transfer field for the avalanche electrons to

reach the grounded anode, mounted 2.3 mm below the THGEM bottom. The gain was obtained by the ratio between the current measured in the induction electrode after multiplication in the THGEM's holes (using the setup presented in Figure 21B) and the photocurrent extracted from the photocathode to the mesh above it without gas multiplication (as measured with the setup presented in Figure 21A).

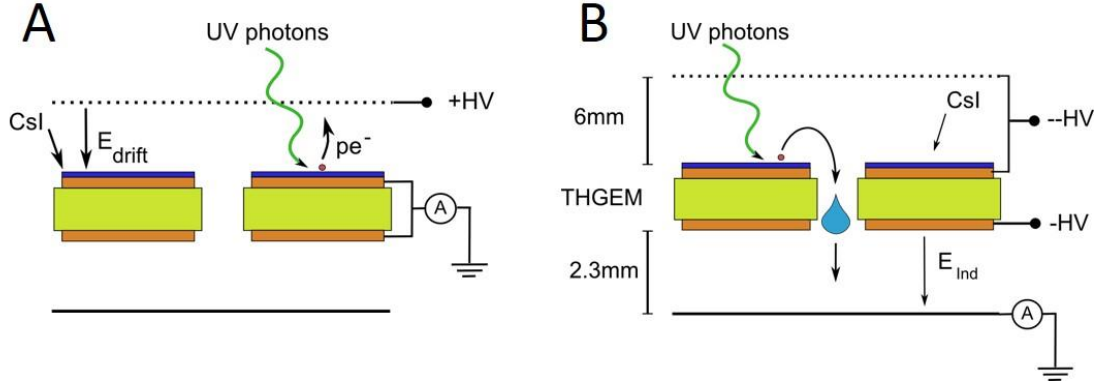


Figure 21: Scheme of the experimental setups used for extraction efficiency (A) and gain measurements (B).

4.6 Setup for gamma-ray imaging (GPM+LXe converter)

Two types of gamma-ray imaging experiments were performed with the full system (GPM+LXe converter), using either a broad beam partially blocked by a Pb edge absorber, or a narrow collimated beam directly irradiating the detector. Both experiments were done using a disc-shaped ^{60}Co source (active part: 1 mm-thick, $\text{\O}3.6$ mm, sealing: double-encapsulated 15.88 mm-thick $\text{\O}6.35$ mm), emitting $3.7 \cdot 10^7$ γ/s of 1.17 and 1.33 MeV over 4π . The detector was operated with Ne/5% CH_4 at gain of 4×10^4 at 485 torr and 208 K (broad-beam experiments) and 356 torr and 211 K (narrow-beam experiments). The flow was kept at 20 sccm throughout all measurements.

The broad-beam experiments comprised a 12 mm-thick Pb plate (see Figure 22A), covering half of the detector's active area; it was located at the OVC bottom, 191 mm below the capillary-converter, and 822 mm above the open (uncollimated) ^{60}Co source (see Figure 22B).

In the narrow-beam experiments the source was placed inside a Pb collimator ($\text{\O}3$ mm hole, height = 150 mm, see Figure 23A), positioned on-axis 197 mm below the

capillary-converter bottom (Figure 23B). The calculated beam diameter at the capillaries bottom and top was ~ 7 mm and ~ 8 mm, respectively.

Data were recorded with the SRS system, triggered by the pulses from THGEM top3 (see electronic scheme in Figure 24).

The flat images (without an object in the beam), used for image normalization, were measured with an open source, located 1093 mm from the capillary-converter bottom.

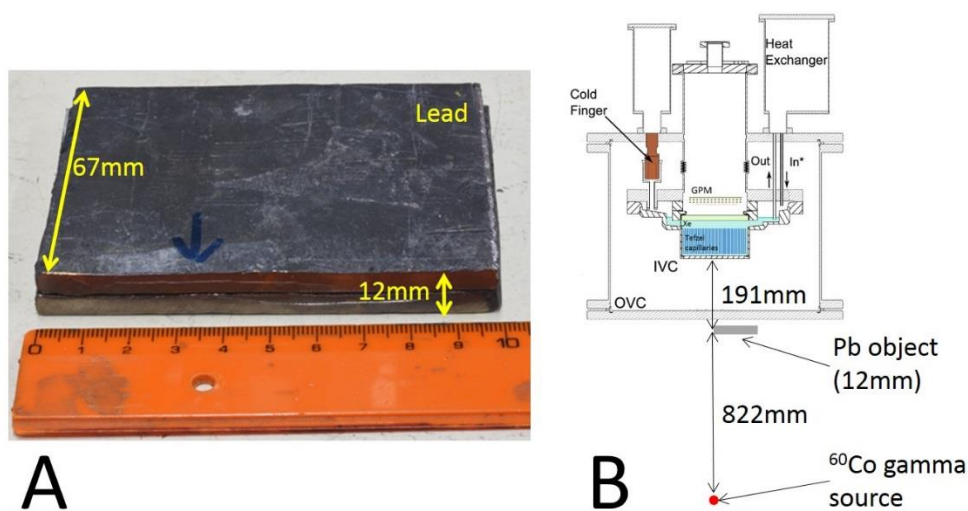


Figure 22: A- The Pb- edge object (thickness of 12mm). B- The measurements setup.

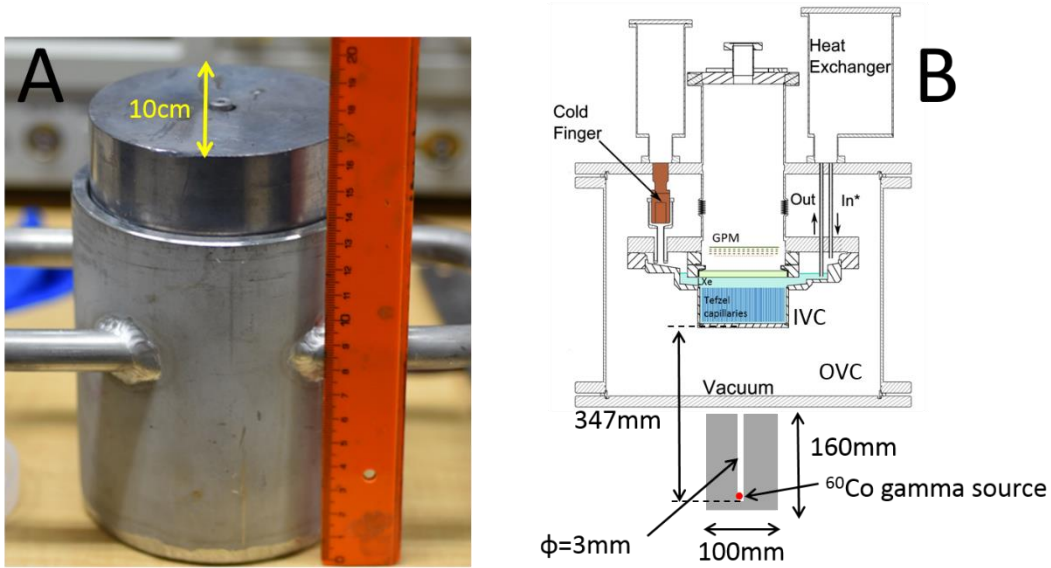


Figure 23: A- The gamma collimator is a lead cylinder ($\phi=100$ mm, height=160 mm) with a hole ($\phi=3$ mm, height=150mm). B- The measurement setup.

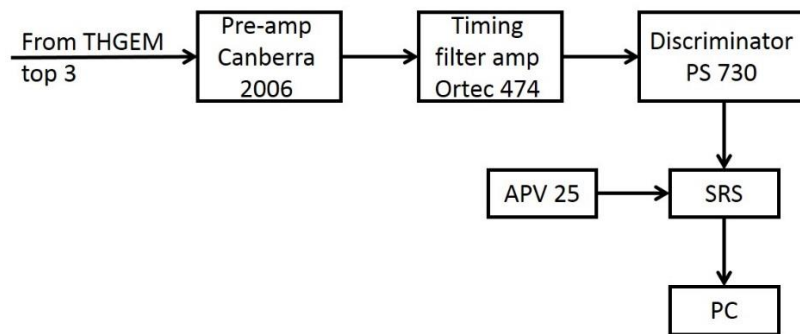


Figure 24: Electronic setup for imaging experiments

4.7 Setup for imaging by mixed neutron and gamma field (GPM+LXe converter)

On the absence of a pure neutron source, mixed-field imaging experiments were performed using an AmBe neutron and gamma source. The active part ($\phi 10$ mm, height=10 mm, 96 mCi) of the AmBe source is encapsulated ($\phi 18$ mm, height=18 mm) and emits $2.2 \cdot 10^5$ n/s over 4π , in a typical energy spectrum (0-11MeV, see Figure 44); $\sim 1.5 \cdot 10^5$ 4.4MeV γ /s are emitted over 4π , via the ${}^9\text{Be}(\alpha, n; \gamma){}^{12}\text{C}$ reaction [90]. The 5.4 MeV alpha is stopped within the source's capsule. In all measurements, the AmBe source was wrapped with a thin Pb layer, absorbing the intense 59.5keV gamma line, emitted by the ${}^{241}\text{Am}$ isotope.

Some TOF measurements were tempted, despite the very short neutron flight path, for demonstrating fast-neutron spectroscopy and neutron/gamma discrimination (see TOF electronic schema in Figure 25). The 4.4 MeV gammas, measured in a detector located close to the source (LaBr in our case), yielded the "start" (trigger) signal; the neutrons, detected in the GPM, provided the "stop" signal to the TAC. Since the LaBr detector rate is much higher than that of the GPM the actual start signal was taken from the GPM after a suitable delay. This reduces significantly the "busy" time of the Time-to-amplitude Converter (TAC).

The relatively low AmBe-source activity and the low gamma/neutron coincidence probability (small solid angle), did not permit performing "neutron-only" imaging measurements in these conditions. Hence, we performed two types of measurements; 1. TOF measurements, in which we proved the detector ability to separate neutrons from gamma-rays and 2. Pb-edge imaging with mixed neutrons and 4.4MeV gammas from the AmBe source.

4.7.1 Time-of-flight measurements

TOF measurements were done with the GPM, using a LaBr detector for detecting the 4.4 MeV gamma-rays emitted in coincidence with the neutrons. In a first step, the 511 keV and 1274 keV gamma-rays emitted simultaneously from ^{22}Na source were used in order to set up the electronics and determine the time resolution of the system. In a second step, measurements were performed with gammas and neutrons from the AmBe source; it was located 83 cm from the capillaries-converter bottom and 6 cm from the LaBr detector. The signals from the top electrode of the GPM's THGEM3 (see Figure 14) and the signals of LaBr detector were preamplified, fed into timing filter amplifiers (TFA, Ortec model 474), constant fraction discriminator (CFD, Ortec model 473A) and to the TAC (Ortec model 467) (see Figure 25). The time spectra were measured with a Multi-Channel Analyzer (MCA, Amptek pocket MCA 8000A). The GPM was operated here at a gain of 7.6×10^4 under 365 torr Ne/5%CH₄ at 212 K, with a flow of 3 sccm.

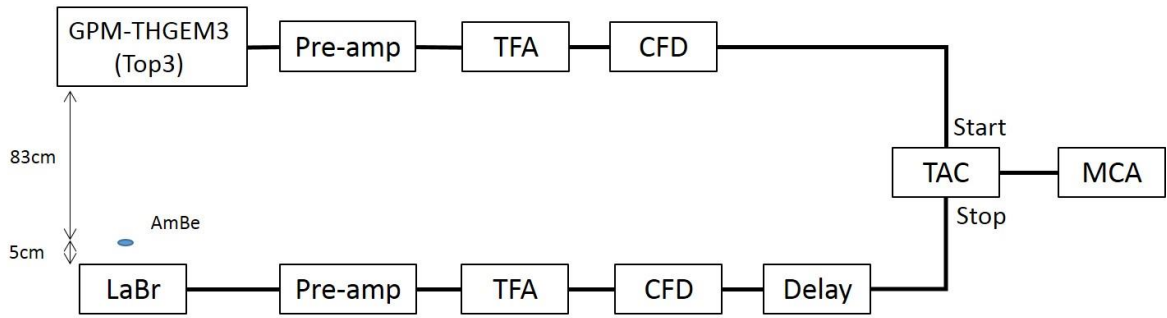


Figure 25: TOF electronic scheme. The signals from the top electrode of the GPM's THGEM3 and of the LaBr detector are pre-amplified and processed by timing filter amplifiers (TFA), constant fraction discriminators (CFD) and a time-to-amplitude converter (TAC). The time spectrum is measured by the Multichannel Analyzer (MCA).

4.7.2 Edge imaging with mixed neutron & gamma field

Imaging of a 12 mm thick Pb edge (object covering half of the detector's area) was performed with the object located below the OVC, 191 mm from the capillaries bottom, and 500 mm above the collimated AmBe source. The collimator role, in this case, was to reduce the neutron background created by neutrons scattered by surrounding materials, by irradiating only the active area of the detector. The source was placed within a $\varnothing 25$ mm bore in a paraffin-filled barrel ($\varnothing 380$ mm, height=710 mm), 300 mm from the barrel's top (see Figure 26). The barrel was covered by a 10 mm Pb lid, perforated at the center ($\varnothing 30$ mm), absorbing gamma-rays emitted by neutron interactions inside the barrel. The neutron-beam diameter, at the capillary-converter bottom, was ~ 60 mm. The GPM was operated here at a gain of 2.4×10^4 under 365 torr Ne/5%CH₄ at 212 K, with a flow of 20 sccm.

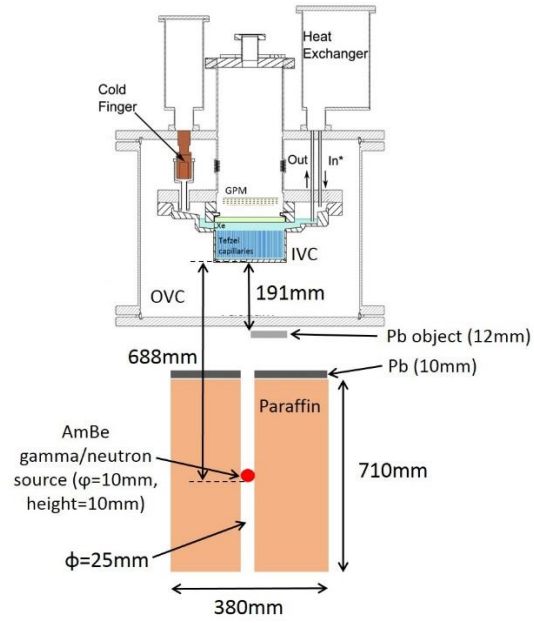


Figure 26: Measurement setup of the Pb- edge imaging with mixed neutrons and 4.4MeV gammas. The AmBe source ($\phi=10\text{mm}$, height=10mm) was placed within a hole ($\phi=25\text{mm}$) in a paraffin-filled barrel ($\phi=380\text{mm}$, height=710mm), 300mm under the barrel's top. The barrel was covered by a 10mm Pb lid.

5 GEANT4 simulations for converter optimization and predicted performance

5.1 Methodology

An comprehensive computer-simulation study was performed, using GEANT4 toolkit (version 9.3.2) [91], aiming at the optimization of a large-size "general" LXe converter geometry (plain-volume LXe one and that of Capillaries filled with LXe) - adequate for future large-area radiographic detectors (see Figure 27A) [83, 92]. Another set of simulations was done for the specific, 100 mm in diameter detector geometry used in our experiments, in which the WILiX cryostat parameters were defined in details, with plain LXe converter and with that of Tefzel capillaries filled with LXe (see Figure 27B). We used the standard GEANT4 model for gamma-rays and standard neutron high-precision GEANT4 models for neutrons with energy below 20 MeV. A benchmark was done by comparing simulation results to a time of flight (TOF) measurement of neutrons through graphite, performed with a liquid scintillator (NE-213).

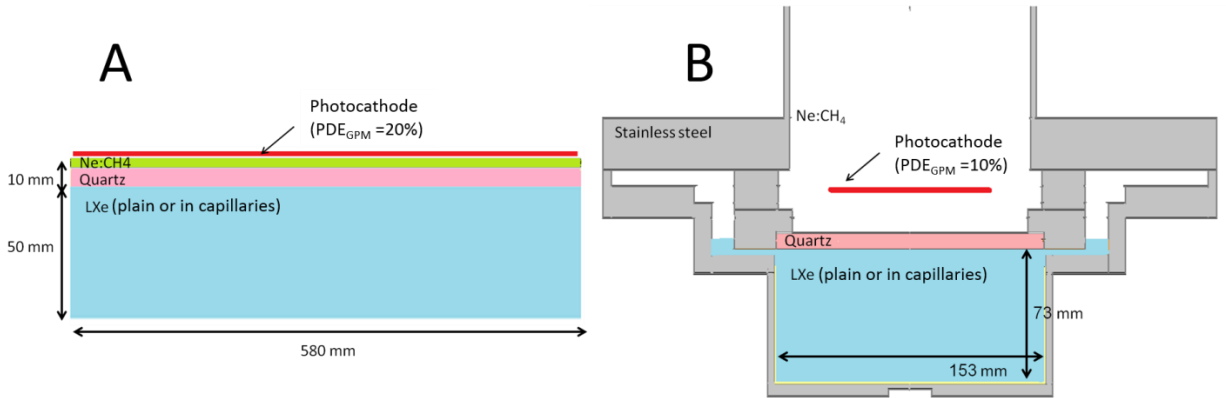


Figure 27: A- the "general" detector geometry for initial simulations. A 580x580x50 mm LXe sensitive volume with or without capillaries, viewed via a 10mm thick quartz UV-window and a photocathode representing a GPM ($PDE_{GPM} = 20\%$). B- Detailed WILiX cryostat geometry. A LXe cylindrical volume ($\phi = 153$ mm, height = 73 mm) with or without capillaries, viewed via a 10 mm thick quartz UV-window and a photocathode ($PDE_{GPM} = 10\%$). The OVC is also defined in the simulations but not shown in the figure. See text for details.

The calculations included all steps in the detection process, namely: gamma and neutron interaction probabilities; total deposited-energy distribution in LXe; total scintillation yields and their spatial distributions within the LXe volume; UV-photon transmission through the window; photon detection efficiency (on the photocathode surface); spatial

distribution of the photoelectrons emitted from the photocathode and their center of gravity (COG) calculation (defining the spatial resolution of the detector).

5.2 Optimization of the LXe converter

The first set of simulations aimed at optimizing the type and performance of various LXe converter types. The main interest has been the optimization of detection efficiency and spatial resolution, for gammas and neutrons in the relevant energy range of 2-15 MeV– derived from the proposed detection concept. These simulations were performed for the large “general” detector geometry, without surrounding materials to avoid effects of scattered radiation from surrounding materials into the LXe convertor.

Two converter configurations were considered:

- A large area plain 580×580×50mm LXe sensitive-volume convertor. A GEANT4 snapshot of this concept is depicted in Figure 28 (right).
- An array of 50 mm long and 1 mm diameter holes, drilled with a hexagonal pattern with a pitch of 1.2 mm in a block of Teflon, Tefzel or Polyethylene with Teflon coating - filled with LXe. Hydrogen-rich capillaries, such as polyethylene or Tefzel, allow efficient transfer of neutron energy close to the point of interaction by reducing the neutron multiple scattering, and thus improving the spatial resolution. Teflon and Tefzel were chosen due to their low refractive index compared to that of LXe, at 178 nm ($n_{\text{LXe}}=1.61$ versus $n_{\text{Teflon}}=1.34$ and $n_{\text{Tefzel}}=1.5$ [93]). A specular total internal reflection was assumed for the photon transmission through the capillary holes [94]. A GEANT4 snapshot of this concept is depicted in Figure 28 (left).

The LXe volume/capillaries are viewed by a 10mm thick UV-window, followed by a 5mm Ne-based gas gap and a CsI photocathode.

The light from the converters was viewed via a 10 mm thick quartz UV-window by the THGEM-GPM (see Figure 27A). The CsI photocathode is deposited on the THGEM’s top face, located 5 mm away from the UV-window.

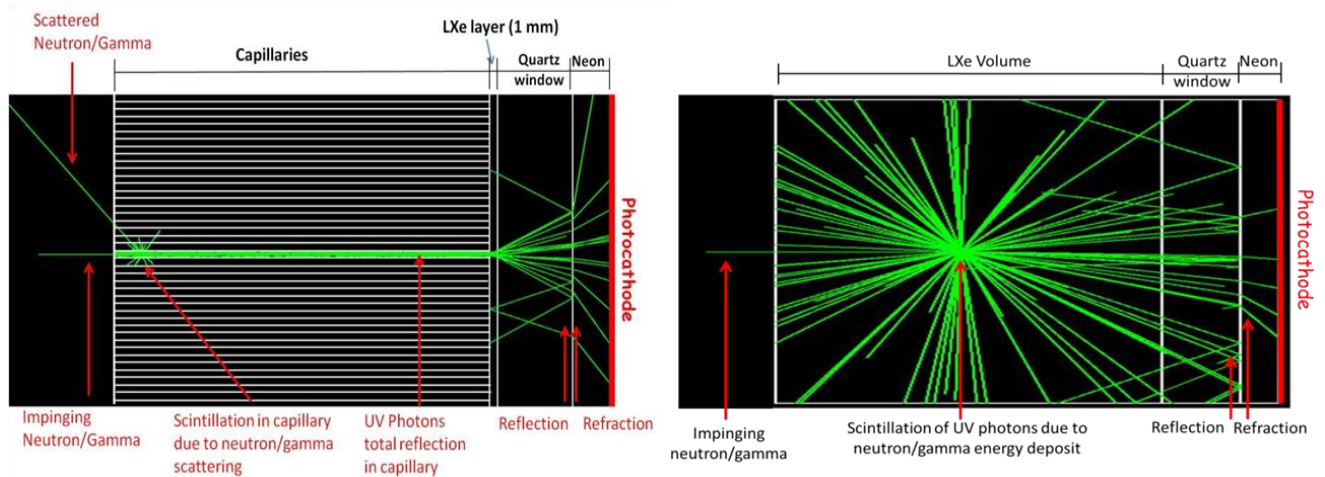


Figure 28: Snapshots of GEANT4 simulation runs (side view): the green lines are tracks of neutral particles (either incident neutron/gamma or UV-photons). Left figure: LXe-filled capillaries (50 mm long and inner diameter of 1 mm) made of Teflon, Tefzel or Polyethylene with Teflon coating; a LXe-filled 1mm gap; a 10mm thick UV-window; a 5mm Ne-based gas gap and a photocathode surface (of the GPM). (Taken from [92]). Right figure: plane 51 mm long LXe volume; a 10mm thick UV-window; a 5mm Ne-based gas gap and a photocathode surface. (Taken from [83]).

A UV-photon detection efficiency (PDE_{GPM}) of 20% was assumed for the GPM. The scintillation light yields of 8.8 photons/keV and 20 photons/keV, for neutron-induced nuclear recoils and gamma-induced electron recoils, respectively, used in our simulations were taken from [22]. The incident neutron and gamma-ray beams, of $1.4 \times 1.4 \text{ mm}^2$, impinged at the center of detector's active volume. For the optimization purpose, we used sub-millimeter pads.

5.2.1 Deposited Energy Spectra

Figure 29 and Figure 30 depict the spectra of deposited energy in the various LXe radiation-converter configurations, computed for gamma and neutron interactions in the relevant energy range 2-14 MeV.

Gamma-ray spectra

For gamma-ray interactions in plain LXe volume (Figure 29A) one can clearly see the photo-peak, as well as single- and double- escape photo-peaks from the dominant pair-production process. A small, but visible, peak at 511 keV on the low energy side of the gamma spectra originates from pair production and annihilation

processes in the 10 mm thick quartz window. In comparison to a plain LXe volume, the introduction of capillaries (of the geometry described above) causes the following effects: Only 55% of the incident beam particles interact directly with LXe. Gamma-ray induced electrons/positrons created in LXe will deposit only part of their energy within the active volume. Incident particles that interact directly with the capillaries' material create predominantly Compton electrons, of which some reach the active LXe volume and deposit there part of their energy. Hence, we do not see the full or escape photo-peaks except in the case of low-energy gamma-rays where the probability to stop an electron/positron within the active LXe is still relatively high.

Neutron spectra

Figure 30A depicts energy spectra from neutron interactions in plain LXe volume. In a single elastic collision with Xe nucleus, the neutron can transfer not more than about 3% of its energy to Xe (see section 2.2.3). Thus, for a relatively small thickness of LXe, most of the elastic scattering events will deposit small amount of neutron energy per interaction. For example for 2 MeV neutrons the maximum energy transferred to Xe nucleus is about 60 keV. However, one can observe that there are small number of neutron induced events with deposited energy extending up to the incident neutron energy. This is due to inelastic neutron collisions, where the resulting gamma-rays can add their energy to Xe recoil energy. In rare cases, the neutron may deposit higher energy than its incident energy. This may happen when inelastic collisions are followed by neutron capture. In such cases the absorption of the capture gamma-rays will add to the energy of the neutron.

The introduction of Teflon capillaries did not change significantly the absorbed energy spectrum. However, for capillaries made of materials that contain hydrogen, such as Tefzel or polyethylene, the neutron spectra extended to higher values due to the contribution of knock-on protons, which may receive large fraction of the neutron's energy in a single collision.

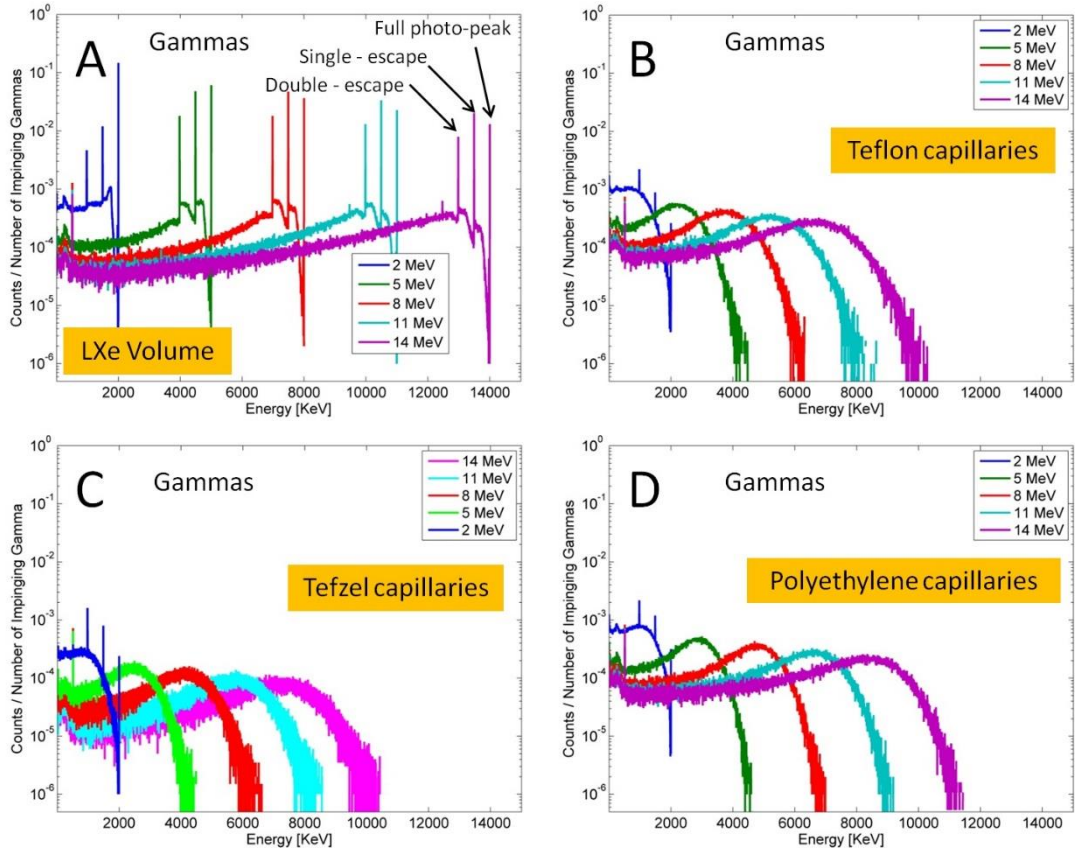


Figure 29: Computer-simulated spectra of deposited energy in $580 \times 580 \times 50$ mm LXe sensitive volume by gamma photons for a) plain-LXe converter, b) Teflon capillaries, c) Tefzel capillaries and d) Polyethylene capillaries. The simulations were made for gamma-ray beam energies of 2, 5, 8, 11 and 14 MeV. The incident beam area of $1.4 \times 1.4 \text{ mm}^2$ was impinging at the center of detector's active volume.

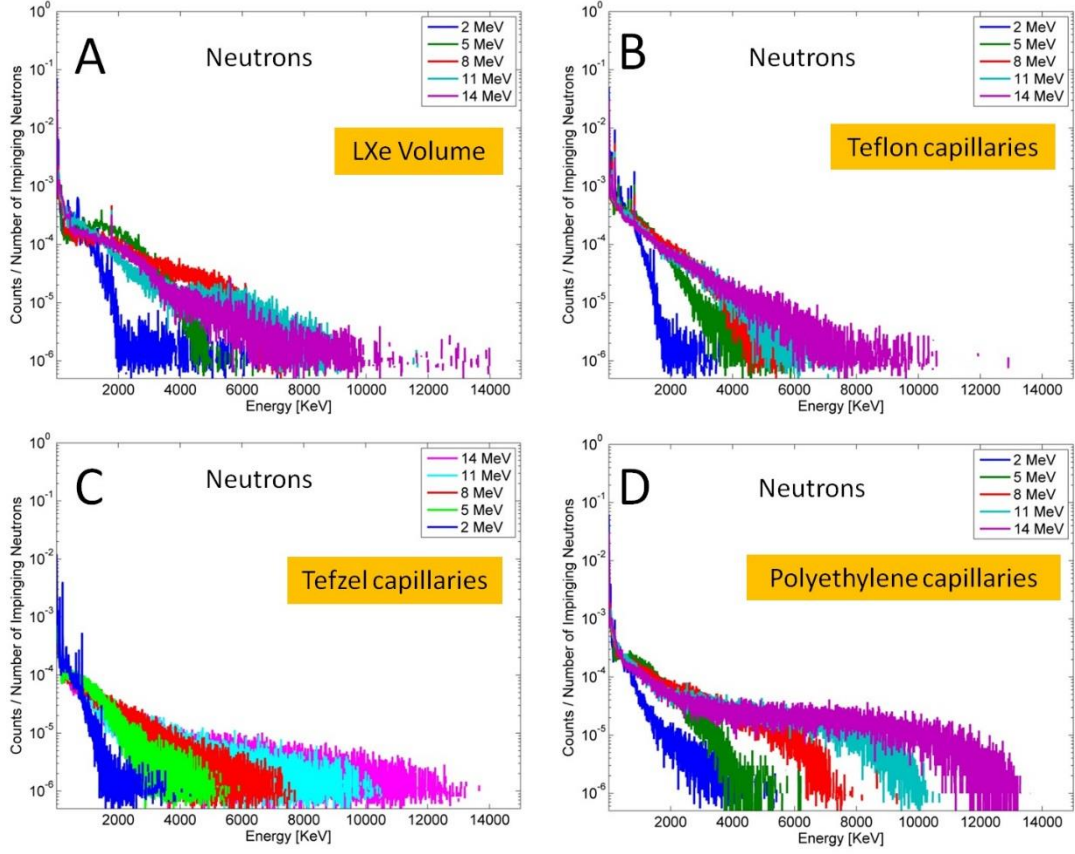


Figure 30: Computer-simulated spectra of deposited energy in $580 \times 580 \times 50$ mm LXe sensitive volume by neutrons for a) plain-LXe converter, b) Teflon capillaries, c) Tefzel capillaries and d) Polyethylene capillaries. The simulations were made for neutron energies of 2, 5, 8, 11 and 14 MeV. The incident beam area of 1.4×1.4 mm² was impinging at the center of detector's active volume.

The average gamma-ray and neutron energies deposited in the active volume, available for light production, are shown in Table 3. It includes all possible modes by which the incident particle can leave its energy to scintillation in LXe.

Table 3: Average deposited energy, in the various large-detector configurations ($580 \times 580 \times 50$ mm), for selected gamma and neutron beam energies.

Energy of impinging beam [MeV]	Average deposited energy in LXe volume setup [keV]		Average deposited energy in Teflon capillaries setup [keV]		Average deposited energy in Tefzel capillaries setup [keV]		Average deposited energy in Polyethylene capillaries setup [keV]	
	gamma	neutron	gamma	neutron	gamma	neutron	gamma	neutron
2	1310	220	700	240	740	200	820	170
5	3590	900	1820	620	1970	620	2230	620
8	5930	1100	3020	760	3260	840	3680	1020
11	8100	750	4150	720	4510	910	5020	1340
14	10030	730	5170	810	5640	1120	6200	1740

For gamma-rays, only the plain LXe converter exhibits peaks (full photo-peak, single and double escape) in the spectrum. The introduction of capillaries causes significant modification in the spectrum, since the gamma-ray induced electrons/positrons created in LXe deposit only part of their energy within the scintillator volume. Thus, the pulse height distribution expected with a capillary converter will not show peaks. In case of DDEGR, where we use only two energies (4.43 MeV and 15.1 MeV), this should not present a problem since the two gamma-ray energies are sufficiently distant from each other, as demonstrated in Figure 45C.

Deposited energy neutron spectra are continuous in all converters. The addition of hydrogenous media in the form of Tefzel or polyethylene capillaries extends the spectra to larger deposited energy values. As we intend to perform neutron spectroscopy by TOF, the pulse height analysis of neutrons is of less relevance here.

5.2.2 Detection Efficiency

The detection efficiency is defined here as the number of particles (neutron/gamma) interacting in the LXe sensitive volume, resulting in at least one photoelectron, detected by the GPM, normalized to the total number of particles impinging on the detector. The detection efficiency of gammas and fast neutrons, computed for the different converter variants over the relevant energy range, are shown in Figure 31. Neutron detection efficiency of the early version of TRECOR, the TRION detector (30 mm thick scintillation-screen + intensified CCD) [11, 12], is also shown for comparison. The detection efficiency is rather constant over the whole energy range, of the order of 20% and 30%-40% for fast neutrons and gammas, respectively. For gammas, due to the large energy deposition by Compton electrons and their resulting high scintillation yield (see Figure 29 and Table 3), the detection efficiency is equal to the conversion efficiency; namely, every gamma interacting in LXe generates at least one photoelectron detected by the GPM.

Detection efficiencies of gammas in Teflon and Tefzel converters are roughly the same. The low density of polyethylene causes some reduction in gamma-ray

efficiency. The plain-LXe converter provided the highest detection efficiency, e.g. of ~45-55% for 2-14MeV gammas.

For neutrons, a significant number of events deposit very small amount of energy in LXe (see Figure 30 and Table 3). Furthermore, the small number of scintillation photons emitted per keV of deposited energy by neutron-induced Xe recoils (8.8 photons/keV) will result in a lower detection probability. Detection efficiencies of neutrons in the Teflon-capillaries and the plain LXe volume configurations are roughly the same, over the whole energy range.

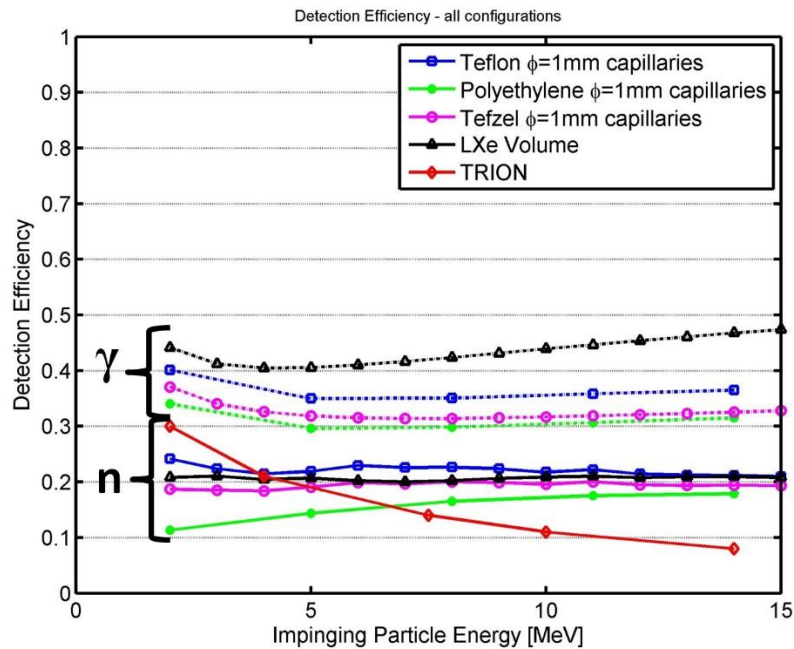


Figure 31: Detection efficiency as a function of energy of the impinging neutrons (solid lines) and gammas (dashed lines) simulated for the detector of Figure 27A with a plain-LXe convertor and that of Teflon, Tefzel and Polyethylene capillaries. Converter thickness: 50mm. Neutron detection efficiency, as calculated in [12] for the TRION detector, is shown for comparison.

One can notice that the neutron efficiency for polyethylene capillaries is significantly lower for low neutron energies. It is thus interesting to investigate the contribution of the knock-on protons to the detection efficiency. The proton-induced scintillation yield is about 8-fold higher (per keV of deposited energy) compared to that of Xe nuclear recoils [22] In addition, due to its higher energy transfer, (see Figure 32)) it deposits larger energy within the LXe compared to Xe nuclei recoils. Hence, the

scintillation light yield per interaction and the resulting detection efficiency are expected to improve. For that purpose, in the analysis of the simulation results, we separated the deposited energy induced by proton originating from the Polyethylene capillary walls (and passing through 10 μm of Teflon coating), from that of the recoil Xe nuclei.

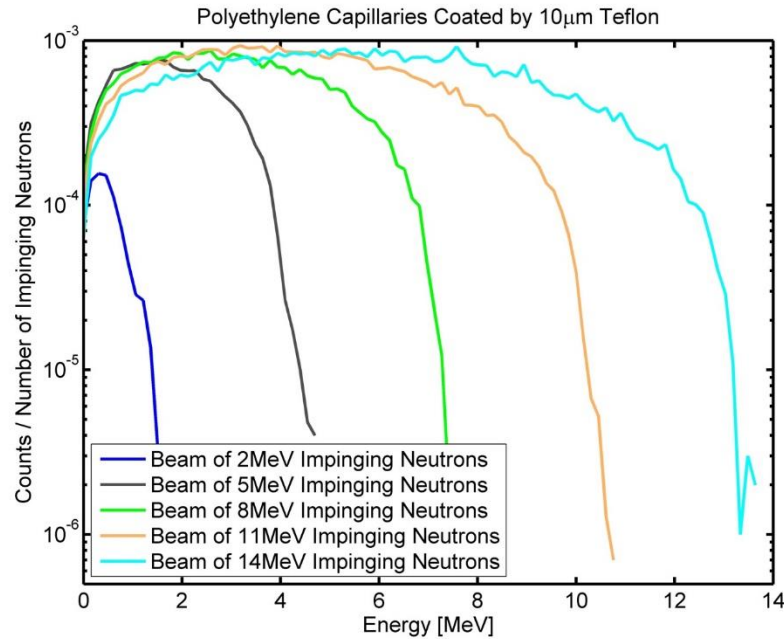


Figure 32: Simulated energy distributions of protons, released from the Polyethylene wall by interacting neutrons (2, 5, 8, 11 and 14 MeV), penetrating into the LXe capillaries.

Table 4 summarizes the efficiencies (energy integral of the distributions of Figure 32) due to protons only. As can be observed, most of the knock-on protons are trapped in the capillary wall; therefore, their contribution to the total detection efficiency is insignificant. Our conclusion is that the reduction of efficiency at low neutron energy is caused by the lower average deposited energy available for production of light (see Table 3).

Using capillaries do not improve the detection efficiency, compared to detection efficiency of plain LXe, but its conspicuous advantage is in term of neutrons spatial resolution, as described in the following section.

Table 4: Calculated number of protons penetrating into LXe normalized to the number of impinging neutrons.

Energy of impinging neutrons [MeV]	Number of detected protons/ Number of impinging neutrons [%]
2	0.08
5	1.37
8	2.66
11	3.98
14	4.94

5.2.3 Spatial resolution

As described above, the reconstruction of the original position of the impinging particle is obtained by calculating the COG of the cloud of photoelectrons detected by the position-sensitive GPM, using Equation 15. Examples of single-event snapshots, simulated in GEANT4 runs, are illustrated in Figure 33 from the detector's front-side (as seen by the photocathode); they show the results of single neutrons and gammas impinging on the LXe sensitive volume, yielding nuclear and electron recoils, respectively, recorded through their resulting scintillation light. The examples of the radiation-induced recoils are shown in a plain LXe-volume and in capillaries drilled in Teflon and Polyethylene, filled with LXe (represented as 1 mm diameter circles). The initial positions of the impinging particles are indicated by white arrows. The green lines and spots are neutral particles (i.e. neutrons, gammas or the emitted UV-photons). The transport of the UV-photons, in the plain LXe volume, was suppressed, in order to enable better viewing.

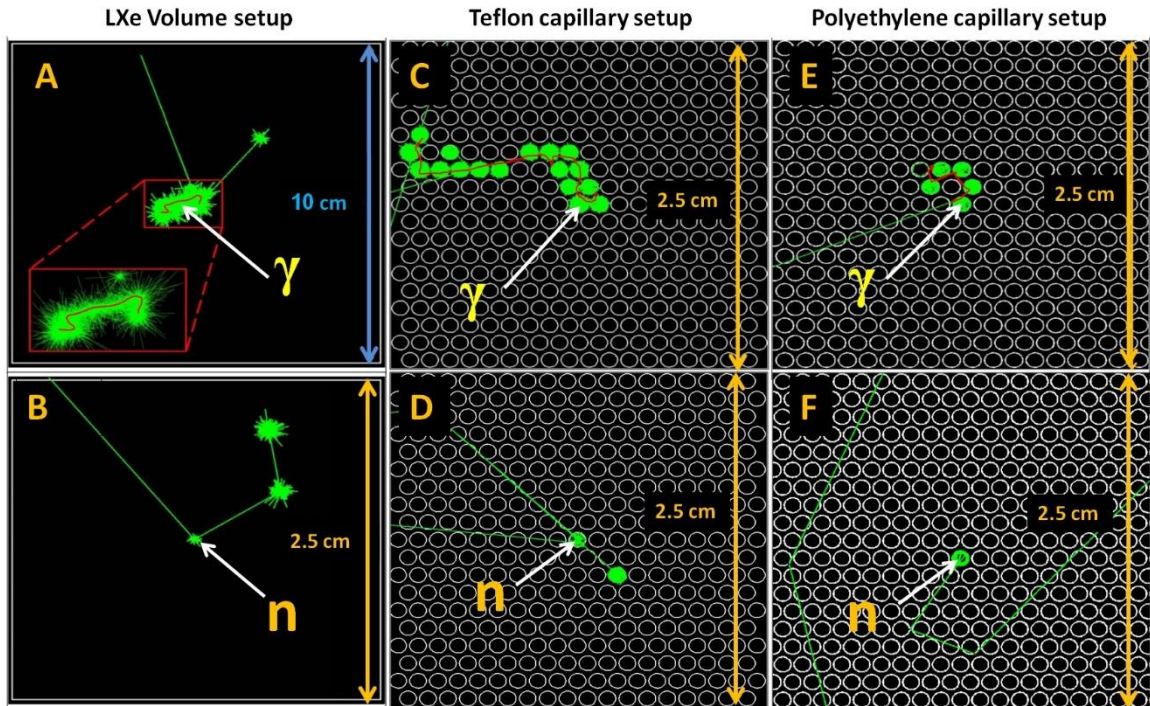


Figure 33: Examples of snapshots of typical GEANT4 runs, seen from the detector's front-side, for impinging neutrons and gamma-rays in a plain LXe converter (figures A, B), LXe in Teflon capillaries (figures C, D) and LXe in Polyethylene capillaries (figure E, F). The scintillation light (green spots) is created by radiation-induced recoils stopped in LXe. The Compton-electron tracks appear in red. The white arrows indicate the radiation-impact locations. While the UV-photon transport is confined within capillaries, their transport in the plain LXe volume was suppressed to enable better viewing. See text. Note different dimensions scale.

As illustrated in Figure 33, the uncertainty of reconstructing the original position of the impinging gamma radiation is mostly due to the long range of Compton electrons. The maximum energy of the ejected Compton electron varies from 88% to 98% of the initial gamma energy for the gamma-ray energy range of 2-15 MeV. Their range in LXe reaches several mm (see Figure 3B); they induce large scintillation-photon yields in several contiguous capillaries or within a few mm of LXe volume. This is well illustrated in upper figures of Figure 33; the interactions of the Compton electron (in red) and the scintillation photons (in green) occur within the capillaries and in the LXe volume along the Compton-electron track.

Figure 33B and Figure 33D illustrate cases in which the neutron is scattered a few times at distant points (three points in fig B and two capillaries in fig D). Reconstruction of the neutron-induced interaction position, for these multiple-scattering processes in the LXe, are difficult due to the large spread of the scintillation

light. On the contrary, Figure 33F shows an ideal situation where the impinging neutron is directly scattered within the capillary, then scattered again few times in the polyethylene support, losing its energy there without scintillation. Reconstruction of the original position of the impinging neutron in this case is straightforward.

Figure 34 illustrates the spatial distribution of the detected photoelectrons on the GPM's photocathode, for three of the radiation-converter setups. The color scale relates to the total number of detected photoelectrons. Each of the figures depicts the photoelectrons cloud resulting from a particular single event, its calculated COG (denoted as "cg" in the figure) and the original impact location (denoted as "i" in the figure) (as explained below).

In the case of *neutrons*, the geometrical spread of the detected photoelectron distributions in the detector with LXe in Teflon capillaries and in the plain LXe volume converter is larger than that with the LXe-filled Polyethylene capillaries one. This is due to a larger number of multiple-scattering interactions in the former configurations.

In the case of *gamma* irradiation, the geometrical spread of the detected photoelectron distributions in the plain LXe converter is the largest one; nevertheless, the original position of the interacting particle is calculated with a rather small uncertainty due to the large number of photoelectrons.

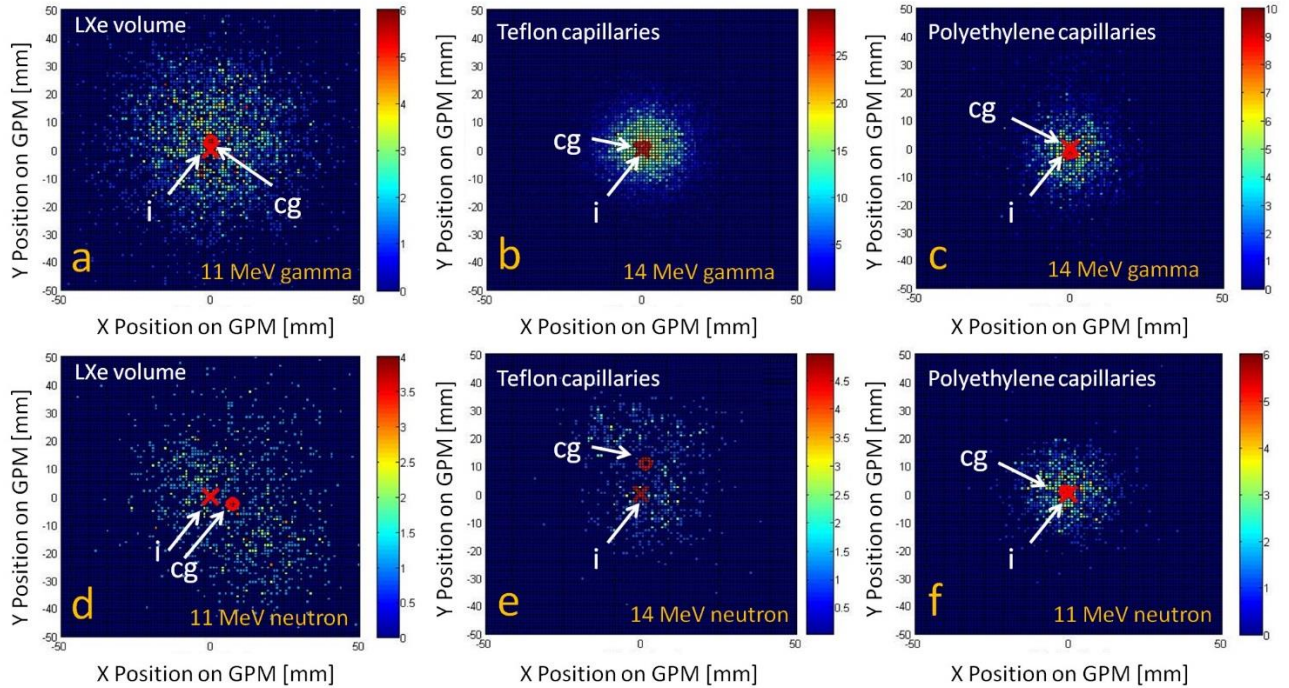


Figure 34: Examples of 2D spatial distributions of single-event induced photoelectrons originating from the GPM's photocathode (detected photoelectrons), simulated for three LXe converter geometries of Figure 27A, for gamma-rays (a, b and c) and neutrons (d, e and f). The color scale indicates the number of detected photoelectrons in each position; (i) is the original radiation-impact location; (cg) is the computed center-of-gravity of the detected photoelectrons cloud.

The detector's spatial resolution was obtained in each configuration by computing event-by-event, the COG (Equation 15) of the detected-photoelectrons distributions on the GPM's photocathode surface. Sub-millimeter pad size was assumed. The distributions, resulting from $2\text{-}20 \cdot 10^6$ impinging particles, are shown in Figure 35. The summary of the FWHM values of the COG distributions is shown in Figure 36.

For the neutrons, the simulated photoelectrons' spatial distributions, and consequently the resolutions, depend on the capillaries' substrate material; this is due to the large differences between the neutron total cross sections in Xe, Teflon, Tefzel and Polyethylene, affecting the neutron's mean-free-path in the converter and the amount of energy transferred to scintillation in LXe. On the other hand, the gamma-induced spatial distributions are almost independent on the capillaries' material, since gamma rays interact mostly with LXe.

Therefore, one may conclude that, while no advantages are reached with the use of capillaries as scintillation-light guides in term of spatial resolution for gammas, they largely improve the spatial resolution for neutrons by more efficient transfer of neutron energy near the point of neutron interaction.

As expected, for neutrons, the narrowest spatial distribution of the COG was obtained with the Polyethylene or Tefzel capillaries (FWHM of ~ 2.5 mm), due to higher energy transfer to the capillary materials close to the point of interaction and higher photons statistics in case of scintillation from knock-off-protons. The broadest COG spatial resolution was obtained in the plain LXe Volume (FWHM of ~ 8 mm).

The large number of photoelectrons emitted in most gamma interactions, and the shorter Compton–electron range in LXe compared to that of the neutron's range, resulted in narrower COG distributions for gammas. Furthermore, the small cross sections for gamma interactions in Teflon, Tefzel and Polyethylene, make these materials “transparent” to gammas, hence similar spatial resolutions were obtained for gamma in all four different detector configurations (FWHM of 3-5mm).

The deterioration of the spatial resolution with the gamma energy is caused by the increase of the Compton-electron range [95].

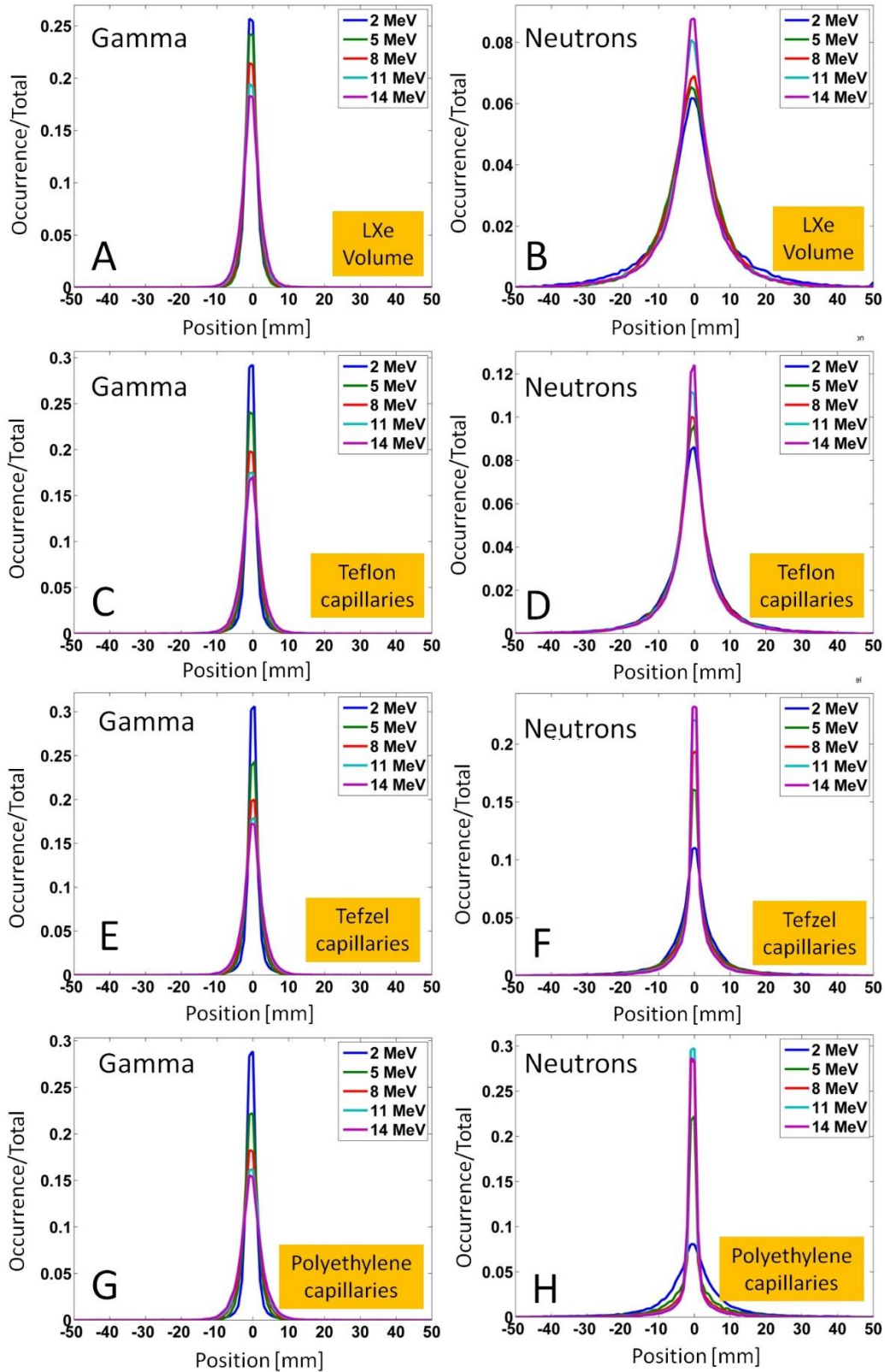


Figure 35: Computed center-of-gravity distributions of photoelectrons from the GPM's photocathode resulting from gamma- and neutron-induced scintillation light in detectors of Figure 27A with different radiation converter configurations. Converter thickness: 50 mm; energy range: 2-14 MeV. The distribution areas are normalized to 1.

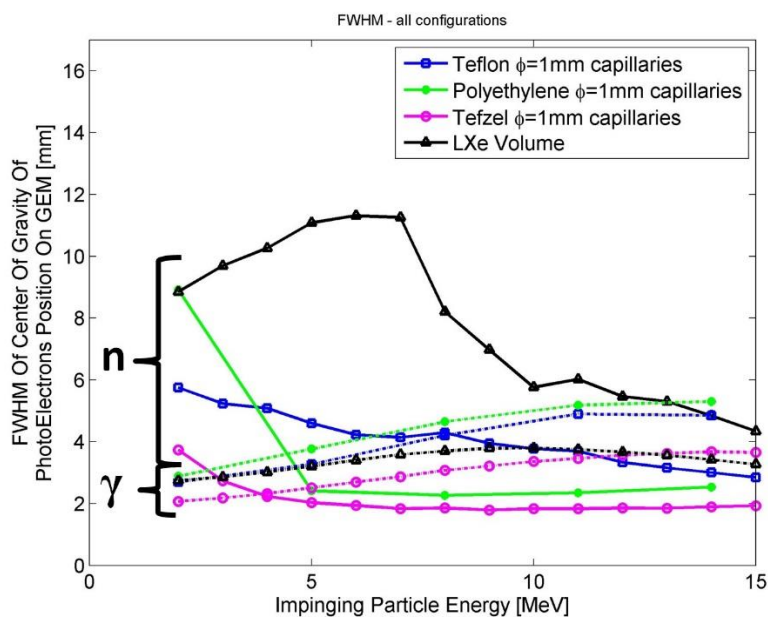


Figure 36: Computed FWHM values of the photoelectrons' center-of-gravity distributions on the GPM's photocathode (of Figure 35), as a function of energy of the impinging neutrons (solid lines) and gammas (dashed lines) for detectors of Figure 27A with different, 51 mm long radiation converter configurations (indicated in the figure).

5.2.4 Effect of beam impinging point

Another set of simulations was done in order to study the effect on FWHM and detection efficiency due to various impinging points on the Tefzel capillaries. 5 MeV neutrons were simulated to imping the detector, with an infinitesimal width beam. The simulations, were done for impinging points in various distances from the center of the capillary (see Figure 37), around $1 \cdot 10^6$ neutrons in each location.

FWHM and detection efficiency results are shown in Figure 38 as a function of the beam distance from capillary's center.

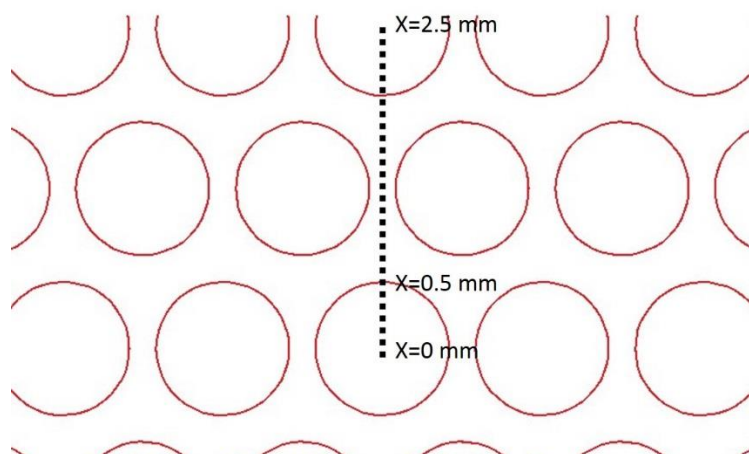


Figure 37: Schematics of the Tefzel capillaries with line indicating the various impinging points

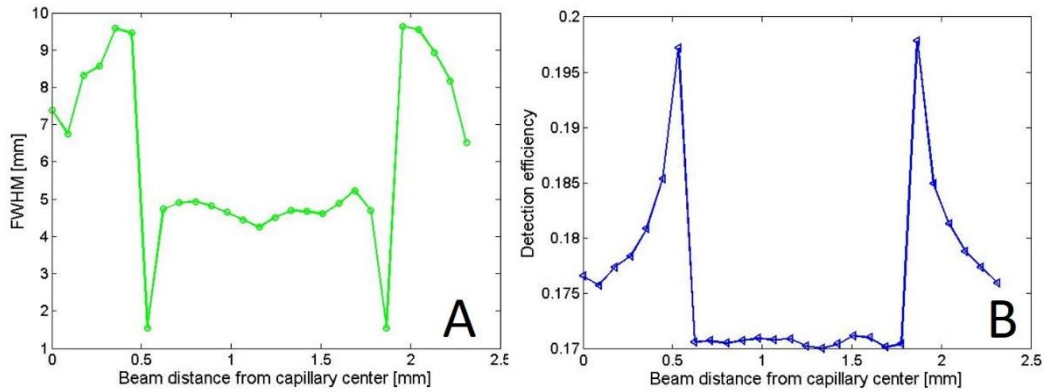


Figure 38: FWHM (fig A) and detection efficiency (fig B) as a function of the beam distance from capillary's center.

5.2.5 Capillary - dimensions optimization

In paragraph 5.2.2 (Figure 31) we demonstrated that detection efficiencies of neutrons in the Tefzel- or Polyethylene capillaries and in the plain LXe volume setups are roughly the same, over the whole energy spectrum. On the other hand, the spatial resolution, obtained for fast-neutrons in the Tefzel or Polyethylene capillaries setups is considerably narrower compared to that of the plain LXe configuration - due to efficient neutron energy losses by collisions with H atoms.

The H atoms content in Polyethylene (14% H) is higher than in Tefzel (3% H). However, the relatively low melting temperature of Polyethylene probably prevents coating the inner walls of capillaries by a Teflon reflector. Hence, the best practical detector configuration, based on Geant4 simulations, is one with Tefzel capillaries. The Tefzel capillaries' dimensions (e.g. inner and outer radii) were optimized for neutron and gamma irradiation, by Geant4 simulations, performed on commercially available capillary dimensions [96]. The results of the FWHM values of the COG distributions of neutron- and gamma-induced photoelectrons' position on the UV detector, and its detection efficiency, are shown in Figure 39 and in Table 5, respectively, for different capillary sizes and neutron and gamma energies. The optimal capillaries' dimensions (out of the commercially available existing selection in Table 5) are an inner radius of 0.51 mm and outer radius of 0.79 mm. For these dimensions, the calculated neutrons' detection efficiency is ~ 0.18 (2-10 MeV neutrons) and that for gammas is ~ 0.3 (4.4 and 15.1 MeV gamma). The calculated FWHM spatial resolution for fast-neutrons is ~ 1.5

mm (for 2-10 MeV neutrons) and that for gammas ~ 2.4 mm (at 4.4 MeV) and ~ 3.5 mm (at 15.1 MeV).

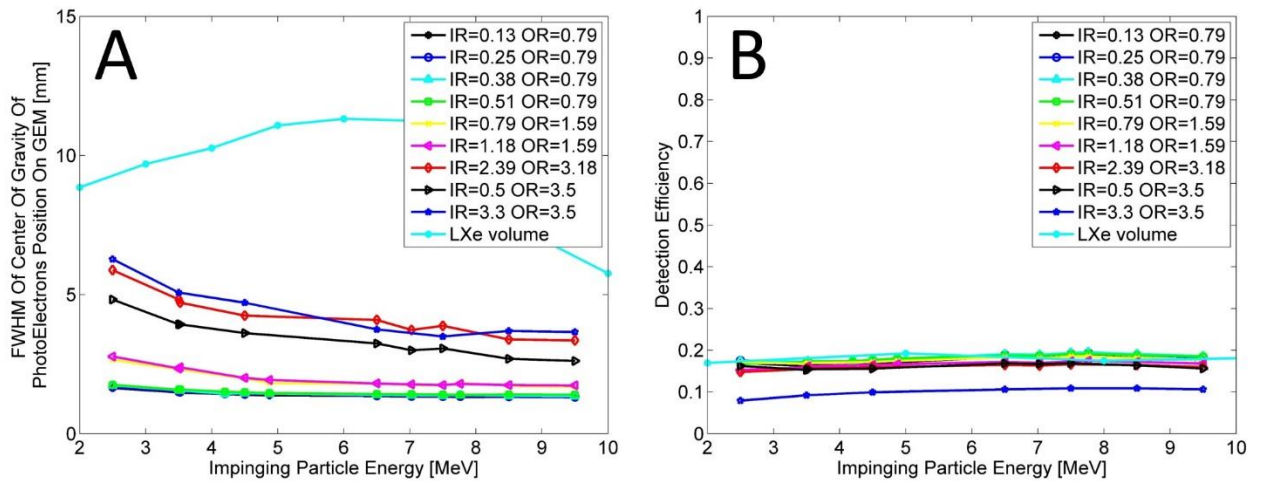


Figure 39: FWHM of the COG distributions of photoelectrons position on the GEM (figure A) and detection efficiency (figure B) for different neutron energies, calculated in the detector of Figure 27A for different capillaries sizes. The FWHM of the COG distribution (black solid lines in Figure 36) and the detection efficiency (black solid lines in Figure 31) of plain LXe volume, with no capillary, are shown for comparison.

Table 5: FWHM of COG distribution of photoelectrons position on GEM, and detection efficiency for the two calculated gamma energies, in the detector of Figure 27A for different capillaries sizes. The best commercially-available Tefzel's dimensions, in terms of detection efficiency, are in the gray line.

Inner Radius [mm]	Outer Radius [mm]	FWHM [mm]		Detection Efficiency	
		4.4 MeV	15.1 MeV	4.4 MeV	15.1 MeV
0.13	0.79	2.7	2.9	0.24	0.19
0.25	0.79	2.6	3.1	0.25	0.21
0.38	0.79	2.6	3.2	0.27	0.25
0.51	0.79	2.4	3.5	0.29	0.30
0.79	1.59	2.7	3.6	0.26	0.25
1.18	1.59	2.9	4.3	0.29	0.33
2.39	3.18	3.6	5.1	0.26	0.33
0.50	3.50	2.6	3.1	0.20	0.19

5.2.6 Simulation of radiographic images – elemental differentiation

Simulations were also carried out in order to evaluate the expected performance, of large detectors ($580 \times 580 \times 50$ mm) equipped with both, the plain LXe volume radiation-converter and of the LX-filled Tefzel capillaries one, having the optimal dimensions (see section 5.2.5), for gamma and neutron radiography and elemental

differentiation. The plain-LXe configuration was chosen as worst case scenario since its spatial resolution, particularly for neutrons, is the lowest. The Tefzel capillaries configuration was chosen as best-case scenario since its spatial resolution, particularly for neutrons, is the highest. Nine objects ($20 \times 20 \times 20 \text{ mm}^3$ for gammas and thicker ones, $20 \times 20 \times 60 \text{ mm}^3$ for neutrons) of various materials were considered: Lead, Tungsten, Uranium, Polyethylene, Graphite, Aluminum, PETN (an explosive), Iron and silicon; they were “irradiated” by uniform discrete energy gamma beams obtainable from the $^{11}\text{B}(d,n\gamma)^{12}\text{C}$ reaction (4.4 MeV and 15.1 MeV, ~ 1600 gammas/ mm^2 for each energy) and by neutrons (continuous spectrum of 2-10MeV, ~ 2800 neutrons/ $(\text{MeV} \cdot \text{mm}^2)$). The transmitted radiation was “measured” by the GPM detector. The simulated gamma-ray pulse-height spectra are shown in Figure 40 for the plain LXe volume and LXe/Tefzel converters. One can observe that compared to the absorbed-energy gamma-ray spectra (see Figure 29 A and C) the peaks here are smeared due to poor light collection. Nevertheless, the two gamma-rays are well separated and the pulse-height spectrum can be used for elemental differentiation. Neutron spectra will be measured (in a real system) by TOF spectroscopy, which is expected to provide very good energy resolution.

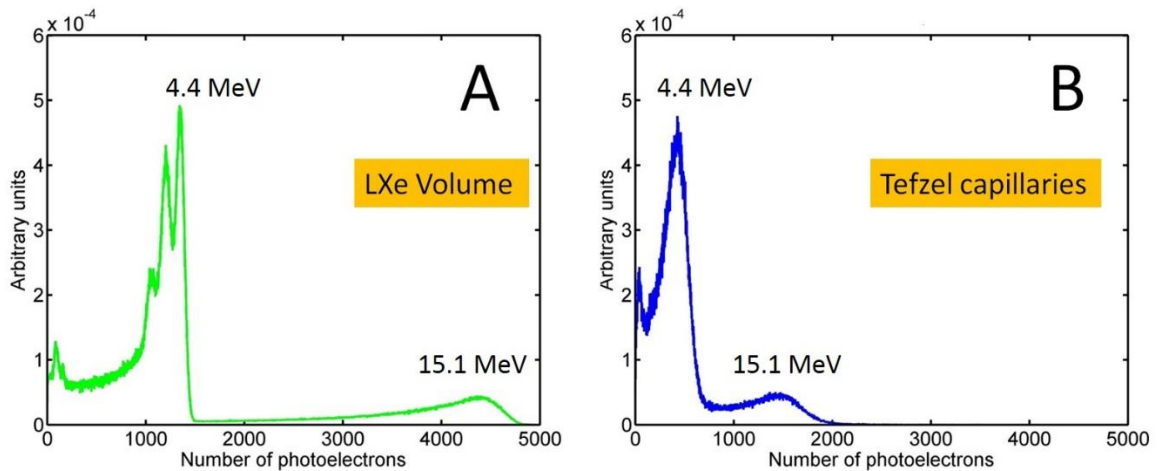


Figure 40: Simulated gamma-ray (4.4 MeV and 15.1 MeV) pulse height spectrum for A- plain LXe volume and B-LXe/Tefzel converters.

Typical simulated-radiography results, performed with this large detector, are shown in Figure 41, for selected 4.4 MeV gamma and neutrons of 9-10MeV. The images were enhanced using Lucy-Richardson deconvolution and median filter algorithms, by MATLAB (version R2011b [97]).

The rectangular objects' shapes can be easily seen in the gamma radiography images with both convertors (Figure 41-A and B), and in the neutron radiography with the Tefzel convertor (Figure 41-D); the images simulated with the plain-LXe convertor (Figure 41-C) are deformed, due to the lower spatial resolution for neutrons with this convertor (see Figure 36).

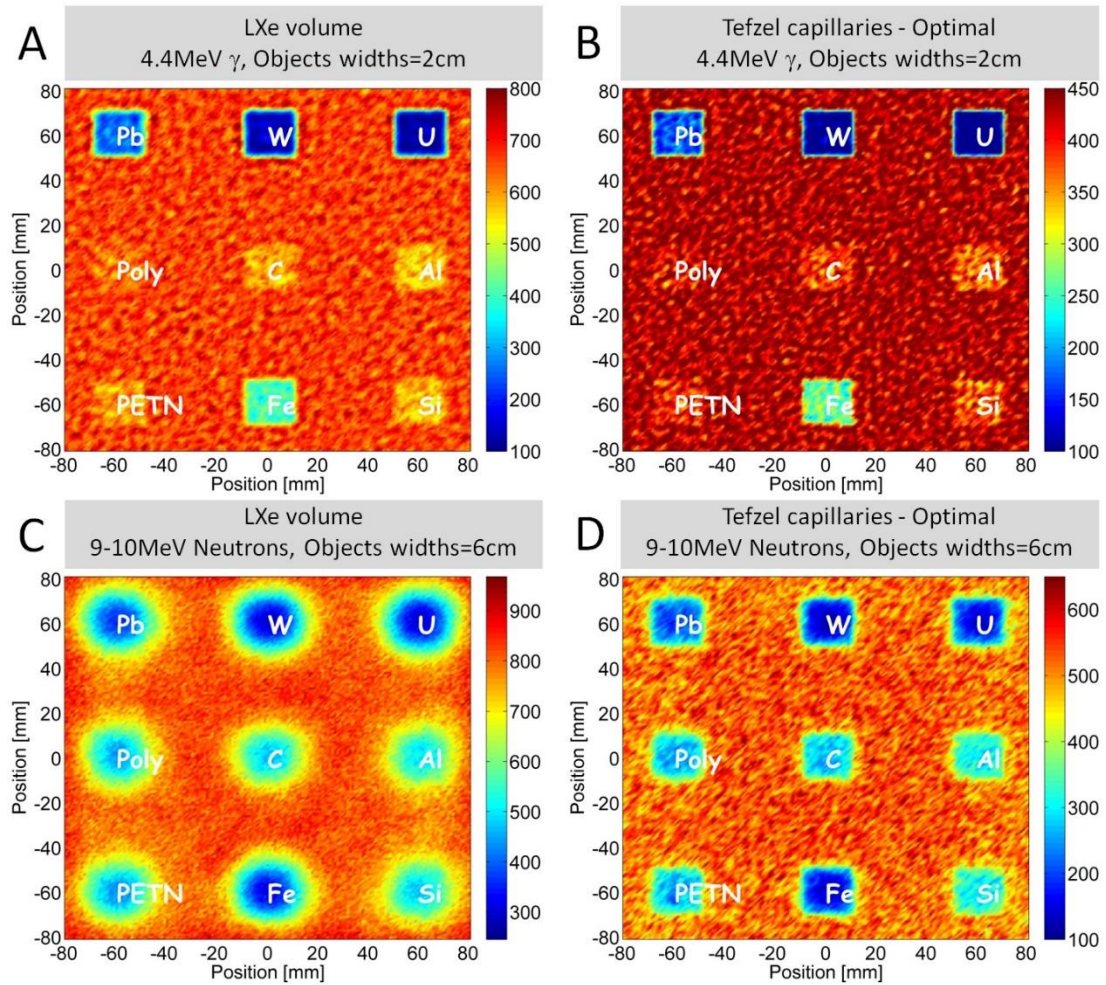


Figure 41: Typical simulated radiography results with a large detector with plain LXe converter (figures A and C) and with LXe/Tefzel-capillaries converter of the optimal geometry (figures B and D), for objects of various materials. The figures show images for selected gamma energy (4.4MeV, figures A and B), and selected neutron energy range (9-10MeV, figure C and D). See text for details.

Simulations of material differentiation by dual-discrete-energy **gamma** radiography (DDEG [7]) were performed using R_{value} - defined, for each element, as the ratio between mass attenuation coefficients of gammas in the two selected energies (Equation 17):

$$(Equation 17) \quad R_{Value}(E_1, E_2) = \frac{\ln(I_\gamma(E_1)/I_\gamma^0(E_1))}{\ln(I_\gamma(E_2)/I_\gamma^0(E_2))} = \frac{\mu_\gamma(E_1)}{\mu_\gamma(E_2)}$$

Where here E_1 is 15.1MeV, E_2 is 4.4MeV, I_γ^0 is the impinging gamma flux, I_γ is the transmitted flux and μ_γ is the mass attenuation coefficient. Materials with low, medium or high Z would result in different R_{value} “regions”, independently of the object density or thickness; hence it would enable rough material differentiation. Table 6 shows R_{value} for the different materials considered here, calculated from the simulations, and the theoretical ones, obtained from tabulated values [28]. The R_{value} numbers calculated from the simulations of both converters are in good agreement with the theoretical ones, for the three R_{value} -regions examined (low ($R_{value} \sim 0.6$), medium ($R_{value} \sim 0.9$) and high Z ($R_{value} \sim 1.35$)).

Table 6: Theoretical and calculated R_{value} numbers. The “error” columns relate to $\frac{R_{Value}^{Theory} - R_{Value}^{Simulation}}{R_{Value}^{Theory}}$.

Material	R_{value}				
	Theory	LXe volume simulation	Error	Tefzel capillaries simulation	Error
Pb	1.34	1.37	-1.9%	1.37	-1.9%
W	1.33	1.32	0.4%	1.33	-0.2%
U	1.35	1.37	-1.5%	1.33	1.4%
Polyethylene	0.56	0.53	5.3%	0.54	2.7%
Graphite	0.59	0.55	5.5%	0.55	6.1%
Al	0.73	0.72	1.4%	0.79	-8.0%
PETN	0.61	0.67	-10.5%	0.67	-10.2%
Fe	0.96	0.98	-2.3%	0.97	-0.9%
Si	0.75	0.75	0.0%	0.72	4.1%

Fast-neutron resonance radiography (FNRR [9]) exploits the differences in neutron's cross-sections with energy, of different elements, to identify specific elements within inspected items. For example, the neutron total cross-section for carbon has resonances

in the energy range of 7.7-8.83 MeV and dips in the range of 6.85-7.2 MeV [31]. A simplistic procedure of dividing the image received with neutrons of 6.85-7.2 MeV by the one with neutrons of 7.7-8.83 MeV would emphasize materials containing high carbon concentration, e.g. graphite (see Figure 42-A for plain LXe converter and Figure 43-A for Tefzel capillaries convertor). Similarly, the neutron cross-section for oxygen has resonances in the energy range of 3.26-3.79 MeV and dip in the 2.31-2.37 MeV range. Dividing the image recorded with neutrons of 2.31-2.37 MeV by the one with neutrons of 3.26-3.79 MeV would emphasize materials containing high oxygen concentration, e.g. a PETN explosive in our case (see Figure 42-B for plain LXe converter and Figure 43-B for LXe/Tefzel capillaries convertor). The Tefzel capillaries convertor is similar to the plain LXe converter in terms of neutron's detection efficiency (see Figure 39B) but provides ratio-images of better resolution.

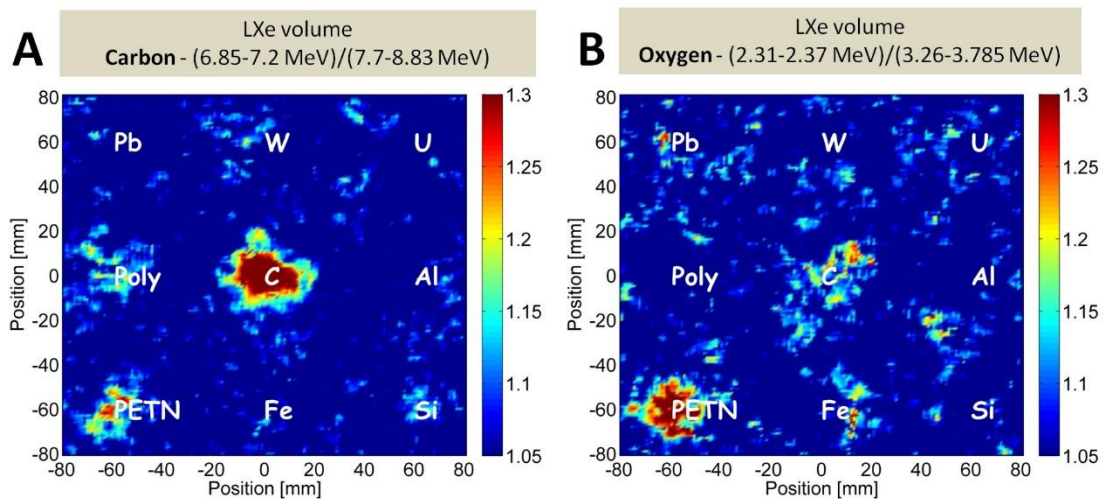


Figure 42: Simulation results of a detector with plain-LXe converter. Material differentiation using fast-neutron resonance radiography. (A) ratio between two images recorded with neutrons of 6.85-7.2 MeV and 7.7-8.83 MeV, emphasizing the graphite object. (B) ratio between two images recorded with neutrons of 2.31-2.37 MeV and 3.26-3.79 MeV emphasizing the oxygen-rich (explosive) object.

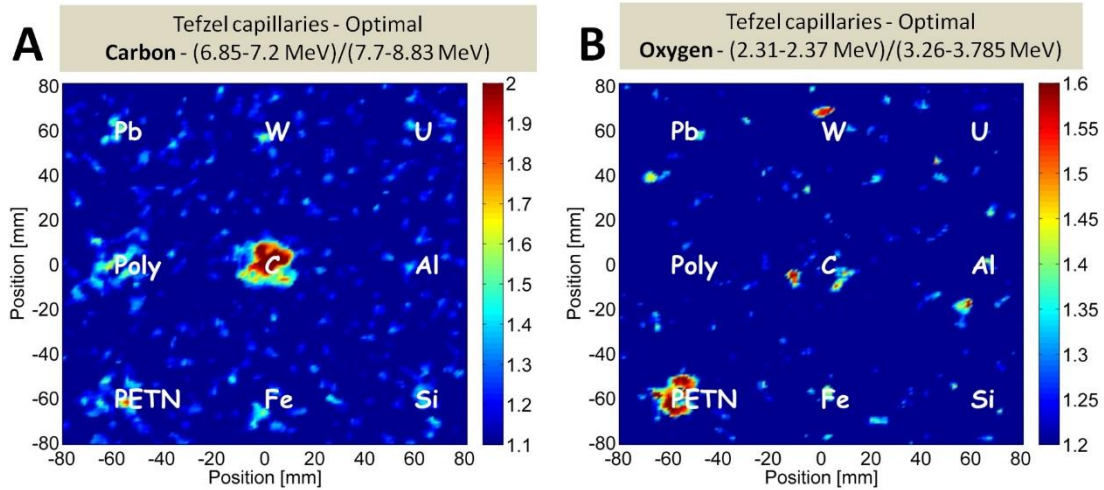


Figure 43: Simulation results of a detector with LXe/Tefzel capillaries converter of the optimal geometry. Material differentiation using fast-neutron resonance radiography. (A) ratio between two images recorded with neutrons of 6.85-7.2 MeV and 7.7-8.83 MeV, emphasizing the graphite object. (B) ratio between two images recorded with neutrons of 2.31-2.37 MeV and 3.26-3.79 MeV emphasizing the oxygen-rich (explosive) object.

5.3 Predicted performance of the small size laboratory detector prototype

Another set of simulations was done for the specific geometry of our experiments with the 100 mm diameter detector, with plain LXe and with Tefzel capillaries; they included a detailed definition of the WILiX cryostat parameters (see 4.1) (see Figure 27B and Figure 12). The simulations included, besides the LXe volume, all cryostat's surrounding materials: A cylindrical LXe volume (diameter 153 mm, height 73 mm) surrounded by quartz jar (to minimize UV reflections) and copper. A large quartz window (diameter 155.4 mm, height 9.4 mm) is in contact with LXe (the LXe level above the window bottom is 5.5 mm). In these simulations we assumed the lowest scintillation-light yield values estimated by [40] for neutron-induced nuclear recoils and gamma-induced electron recoils, namely, 4 photons/keV and 20 photons/keV, respectively (see Figure 7). A CsI photocathode (assumed modest $PDE_{GPM}=10\%$) is located 32 mm away from the window bottom (*Note that in the "general" detector geometry the distance between the UV-window and the CsI photocathode was only 5 mm (see paragraph 5.2)*). The IVC and OVC are made from stainless steel. The IVC wall thickness is 4.0 mm and its bottom (thickness of 7 mm) has a channel (25mm in diameter) in the center, with a residual thickness of 3.0 mm. The OVC wall thickness

is 4.8 mm and its bottom (thickness of 20 mm) has a 41.2 mm hole, covered by a 2 3/4" CF flange (diameter 69.3 mm thickness 12.7 mm). A segmented readout electrode, was defined, containing 61 hexagonal pads as used in the experiment (see 4.3).

Furthermore, neutron and gamma collimators mounted on the ^{60}Co and AmBe irradiation sources were defined. The AmBe collimator (cylinder of 60 cm in height and 40 cm in diameter with collimator hole of $\phi=1$ cm), contained mixture of Borax and water ($\text{Na}_2\text{B}_4\text{O}_7 \cdot 14\text{H}_2\text{O}$) and was coated by 1cm of lead. The ^{60}Co collimator (cylinder of 16 cm in height and 10 cm in diameter with collimator hole of $\phi=1$ cm) was made out of lead.

The continuous AmBe neutron spectrum (Figure 44), ^{60}Co gamma spectrum and gamma rays with energies of 4.4MeV, 15.1MeV (for simulating the gamma spectrum in future Dual-Discrete-Energy Gamma Radiography [7] accelerator experiments) were used as radiation source input data.

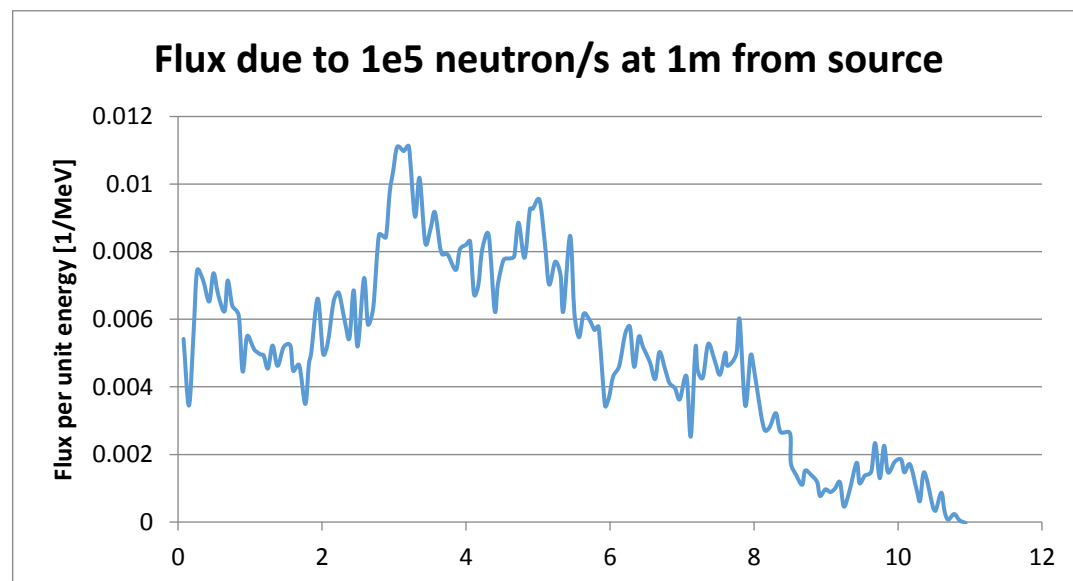


Figure 44: AmBe neutron spectrum (calculated from data from [98]).

Figure 45 shows the deposited energy, the scintillation generated photocathode photoelectron spectra ($\text{PDE}_{\text{GPM}}=10\%$) and the charge spectra after charge amplification in the GPM, simulated for LXe-filled Tefzel capillaries for the relevant gamma energies. On the deposited energy spectrum (Figure 45A) one can clearly see the full-energy photo-peaks, as well as single- and double- escape photo-peaks from the dominant pair-production process. A small, but visible, peak at 511 keV on the low energy side of the gamma spectra originates from pair-production and annihilation

processes in the 10mm thick quartz window. For the 15.1MeV gamma-ray, in LXe-filled Tefzel capillaries, no photo-peak is detected due to the following effects: only 55% of the incident beam particles interact directly with LXe. Gamma-ray-induced electrons/positrons created in LXe will deposit only part of their energy within the active volume. Incident particles that interact directly with the capillary material create predominantly Compton electrons, of which some reach the active LXe volume and deposit part of their energy there. Hence, we do not see the full or escape photo-peaks except in the case of low-energy gamma-rays where the probability to stop an electron/positron within the capillary active LXe volume is still relatively high. This is in comparison with a plain LXe volume, in which an intense full energy photo-peak, as well as single- and double-escape photo-peaks, are detected [83].

The photo-peaks in the photoelectron spectra (Figure 45B) are smeared due to a poor light collection. The avalanche process, which amplifies the charge (with exponential distribution for single PEs), further smears out the charge spectra (see the integrated charge spectra in Figure 45C). Nevertheless, the 4.43 MeV and 15.1 MeV gamma-rays relevant to our application are rather well separated and the pulse-height spectra can be used (with some loss of efficiency) for spectroscopic analysis of material differentiation. The charge spectra of 4.4MeV and 15.1MeV are shown again in Figure 45D, now with the actual branching ratio resulting from the $^{11}\text{B}(d,n\gamma)^{12}\text{C}$ reaction (i.e. the 15.1MeV spectrum is divided by 4). One can set a lower-level threshold to measure only the 15.1MeV gamma-rays. The contamination due to 15.1MeV gamma of the 4.4MeV spectrum is ~38% (ratio between B and A in Figure 45D). This large interference can be corrected for provided the shape of the 15.1 MeV charge spectrum remains constant.

As mentioned above, neutron-energy selection in future radiographic elemental analysis experiments will be done by TOF. However, for better understanding the physics of the detector we show, in Figure 46, the deposited energy, the photoelectron spectra and the charge spectra, as simulated for the selected neutron energies in our specific LXe-filled Tefzel capillaries prototype, taking into account PDEGPM=10%. The neutron's energy deposition spectra simulated in the small LXe-filled Tefzel capillaries prototype (Figure 46A) is similar to that of the large 580×580×50 mm LXe sensitive volume (Figure 30C). See spectra description in section 5.2.1.

The average numbers of PEs, calculated for the relevant gamma and neutron energies, are listed in Table 7 and Table 8, respectively.

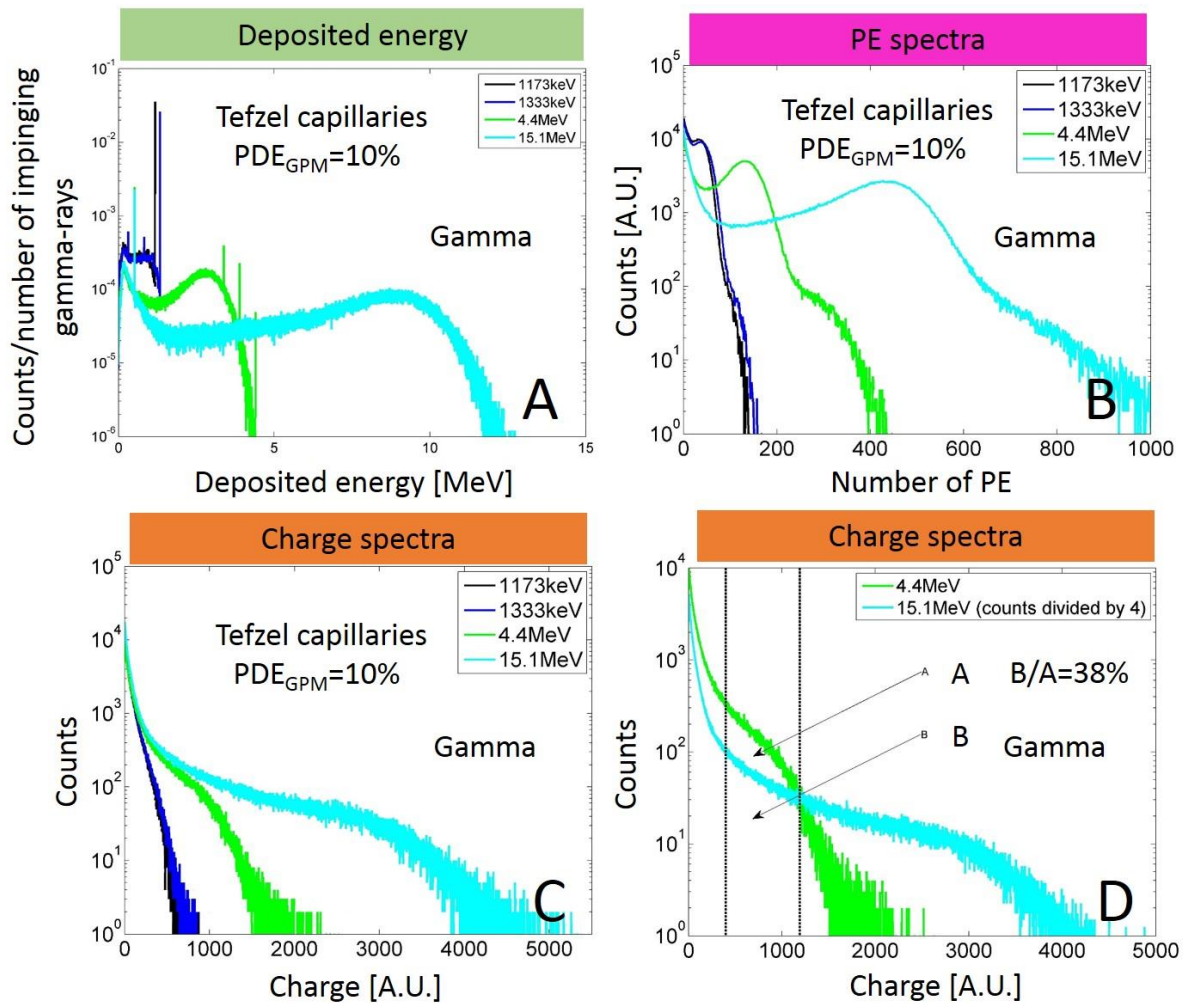


Figure 45: Deposited energy (A), photoelectron spectra (B) and integrated charge spectra (C), as simulated for LXe-filled Tefzel capillaries taking into account $PDE_{GPM}=10\%$ for the relevant **gamma** energies. Figure D shows again the simulated charge spectra of 4.4MeV and 15.1MeV with the actual branching ratios for gammas emitted from the $^{11}\text{B}(d,n)^{12}\text{C}$ reaction. The arrows show the area below the two spectra between the two dashed lines. The calculations were made for the specific, not optimal, geometry of our experiments where the CsI photocathode was located 32 mm away from the UV-window.

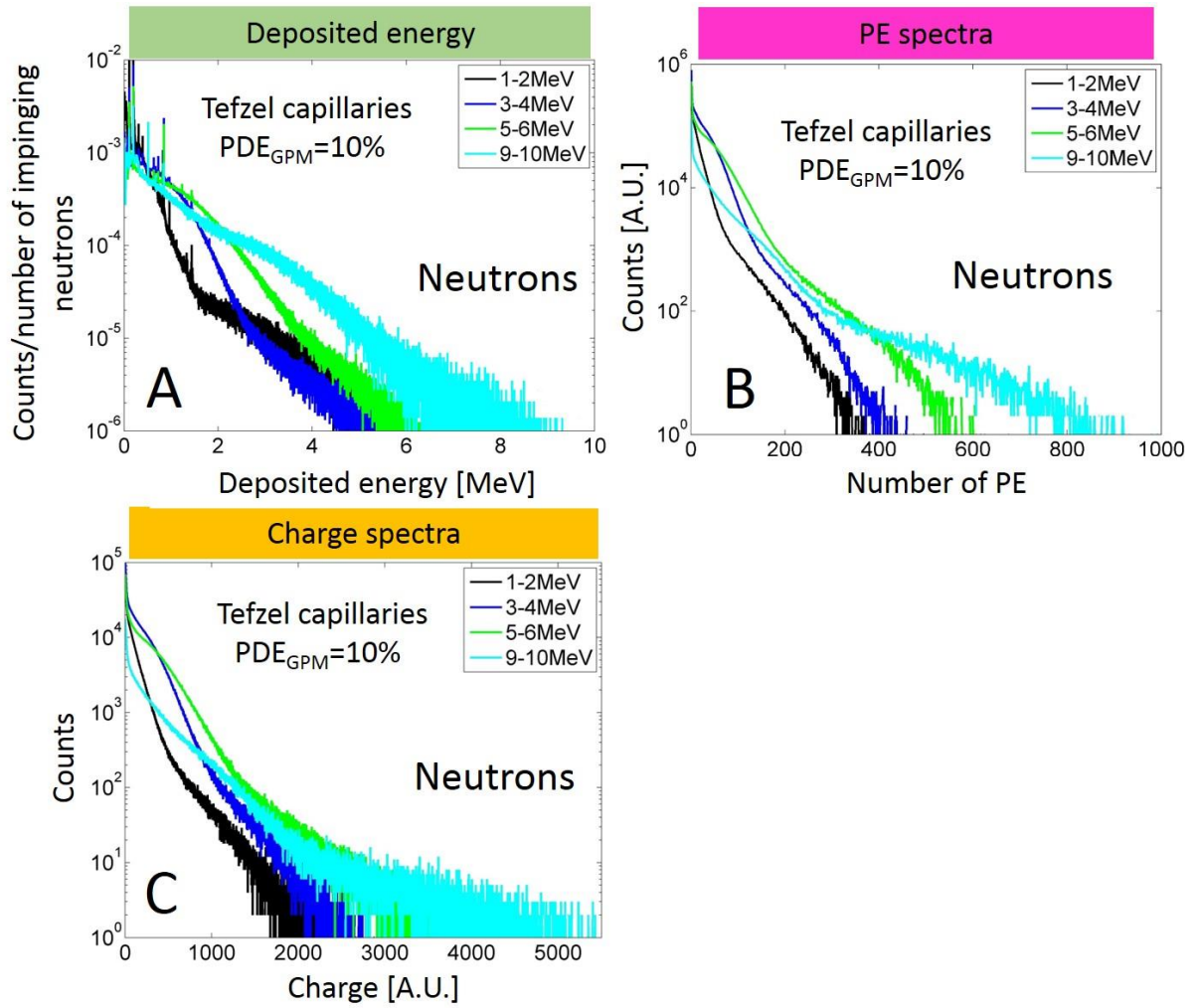


Figure 46: Deposited energy (A), photoelectron spectra (B) and integrated charge spectra (C), as simulated for LXe-filled Tefzel capillaries taking into account $PDE_{GPM} = 10\%$ for the selected **neutron** energies. The calculations were made for the specific, not optimal, geometry of our experiments where the CsI photocathode was located 32 mm away from the UV-window.

Table 7: Calculated average number of PE for the relevant gamma energies (for $PDE_{GPM} = 10\%$). The calculations were made for the specific, not optimal, geometry of our experiments where the CsI photocathode was located 32 mm away from the UV-window.

Gamma Energy [MeV]	Average number of PEs
1.1	28
1.3	31
4.4	98
15.1	297

Table 8: Calculated average number of PE for the relevant neutron energies (for $PDE_{GPM}=10\%$). The calculations were made for the specific geometry of our experiments where the CsI photocathode was located 32 mm away from the UV-window.

Neutron energy range [MeV]	Average number of PEs	Neutron energy range [MeV]	Average number of PEs
0-1	15	6-7	40
1-2	15	7-8	43
2-3	20	8-9	44
3-4	26	9-10	44
4-5	32	10-11	44
5-6	37	AmBe neutron spectrum	32

Imaging simulations

Simulations of the following experiments were performed for both sources that were available to us (^{60}Co gamma-ray source and Am-Be neutron source) and also for the radiations that will be emitted in the $^{11}\text{B}(d,n\gamma)^{12}\text{C}$ reaction:

- Gamma and neutrons imaging of a Pb-object-edge ($\sim 11\text{mm}$ in thick).
- Gamma imaging of a narrow beam ($\phi=3\text{mm}$).
- Imaging of bare neutron or gamma source (flat image).
- Simulations of neutron and gamma pencil beams.

As described in section 4.3, COG histograms are calculated, according to Equation 15, for simulations of imaging with and without an object and the ratio image is calculated according to Equation 16.

5.3.1 Simulation of gamma imaging of a Pb-edge absorber

The point spread function (PSF) of the imaging detector can be obtained by means of the edge spread function (ESF) evaluation technique [99]. Figure 47(A, B, C) shows object-to-flat COG-histogram-ratios, simulated for 1.33, 4.4 and 15.1 MeV gamma-rays emitted from a source positioned at a distance of 916 mm below the OVC bottom, as described above in section 4.6 (Figure 22). The edge Pb absorber (10.9 mm thick) covered half of the OVC. For demonstration purposes, the lower PE threshold in these figures was set to 30PEs, as increasing the threshold did not improve the FWHM any further (see Figure 49A). The color map indicates the transmission of the incident radiation, relative to the case of no object. One can clearly see the area in the detector, which was covered. Theoretically, the transmission of 1.33, 4.4 and 15.1 MeV gamma-

rays through 10.9 mm thick lead plate would be 50%, 59% and 50%, respectively. In practice, the simulated transmissions are somewhat larger: 61%, 67% and 65%, respectively; this is due to gamma-ray scattering by the imaged object positioned at a distance of ~190mm from the sensitive detector area.

The ESF is the average profile of the edge (see Figure 47(D,E,F)). In order to smoothen the statistical fluctuations, we fitted the edge profile with a logistic function (Equation 18) [100], which models the ESF with adequate accuracy (see Figure 47(D,E,F)).

$$\text{Equation 18} \quad \text{ESF}(x) = a_0 + \frac{a_1}{1 + \exp(-a_2(x - a_3))}$$

In Equation 18, a_0 is the curve's minimum value, a_1 is the curve's maximum value above a_0 , a_2 is the steepness of the curve, a_3 is the x-value of the sigmoid's midpoint.

The determination of the PSF is obtained by differentiating the logistic function fitted to the ESF (see Figure 48).

Figure 49A summaries the FWHM of the PSF, estimated by an object edge imaging, for few lower PE thresholds. The FWHM improves slightly with increasing of the lower PE threshold, with best value of ~9mm, ~5mm and ~6mm for gamma-ray energies of 1.33, 4.4 and 15.1 MeV, respectively.

Derivative of edge's ESF is not the exact real PSF due to 2D effects on the 1D ESF. In order to estimate the real PSF we performed simulations of an infinitesimally thin beam (pencil beam) which irradiates the detector in single point (see next section).

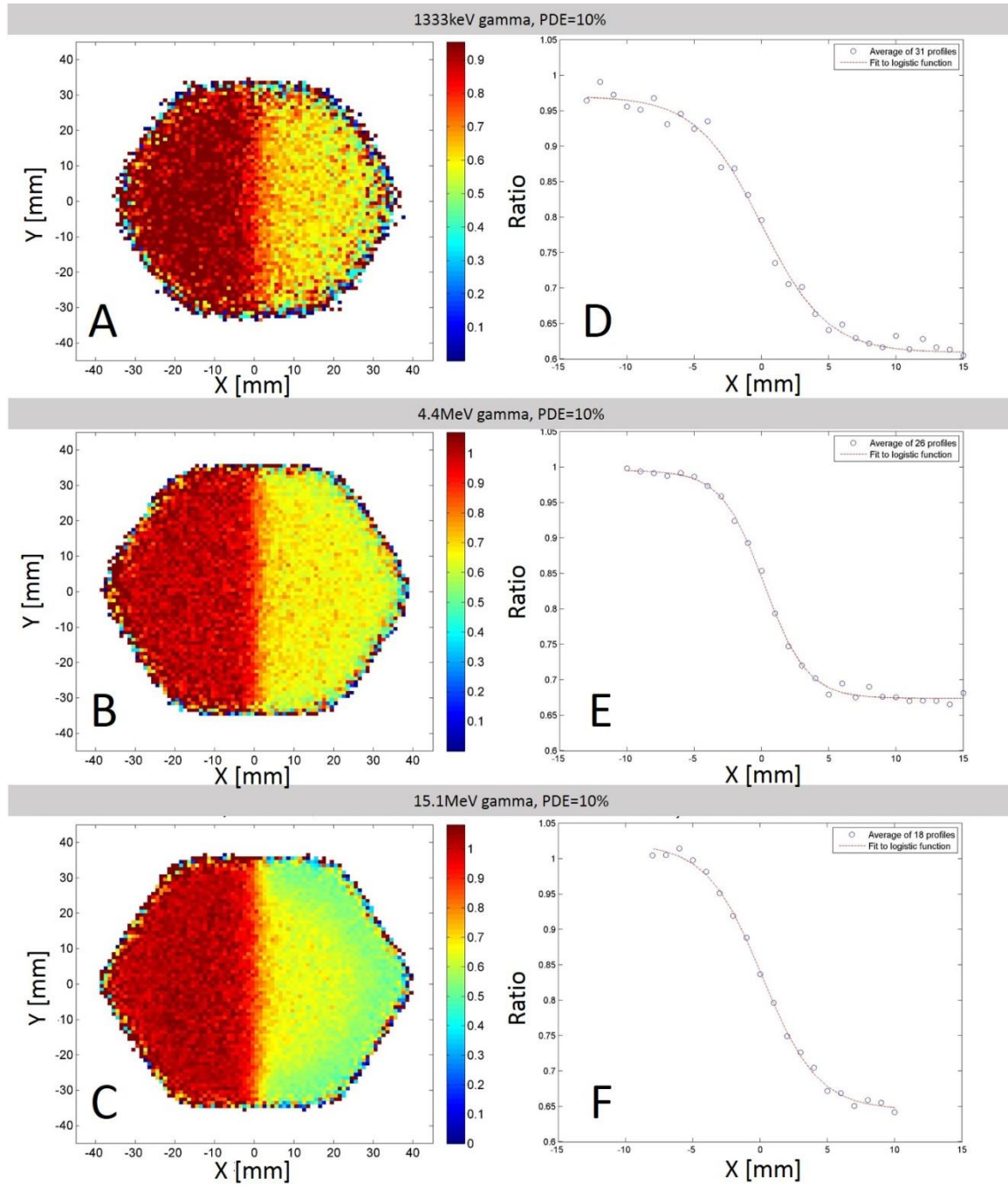


Figure 47: Simulation results of a 10.9mm thick Pb-object-edge gamma imaging, for gamma energies of 1.33, 4.4 and 15.1 MeV. Lower PE threshold was set to 30PEs. A, B and C: 2D image of object to flat COG-histogram-ratios. D, E and F: average edge profiles with fit to a logistic function.

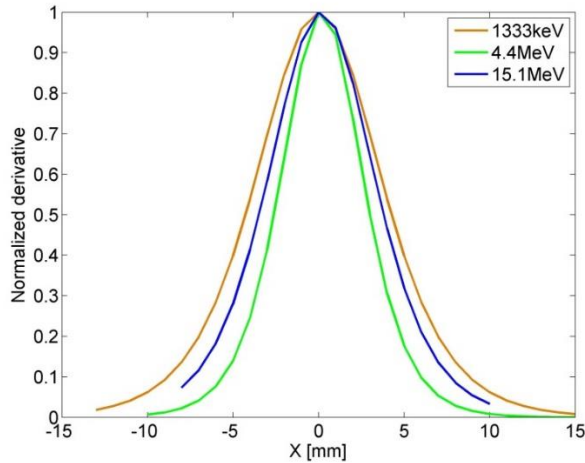


Figure 48: Simulated PSF distributions for 3 gamma energies obtained by irradiating 10.9mm thick Pb-object-edge; data derived from the logistic function fitted to the ESF curves of Figure 47.

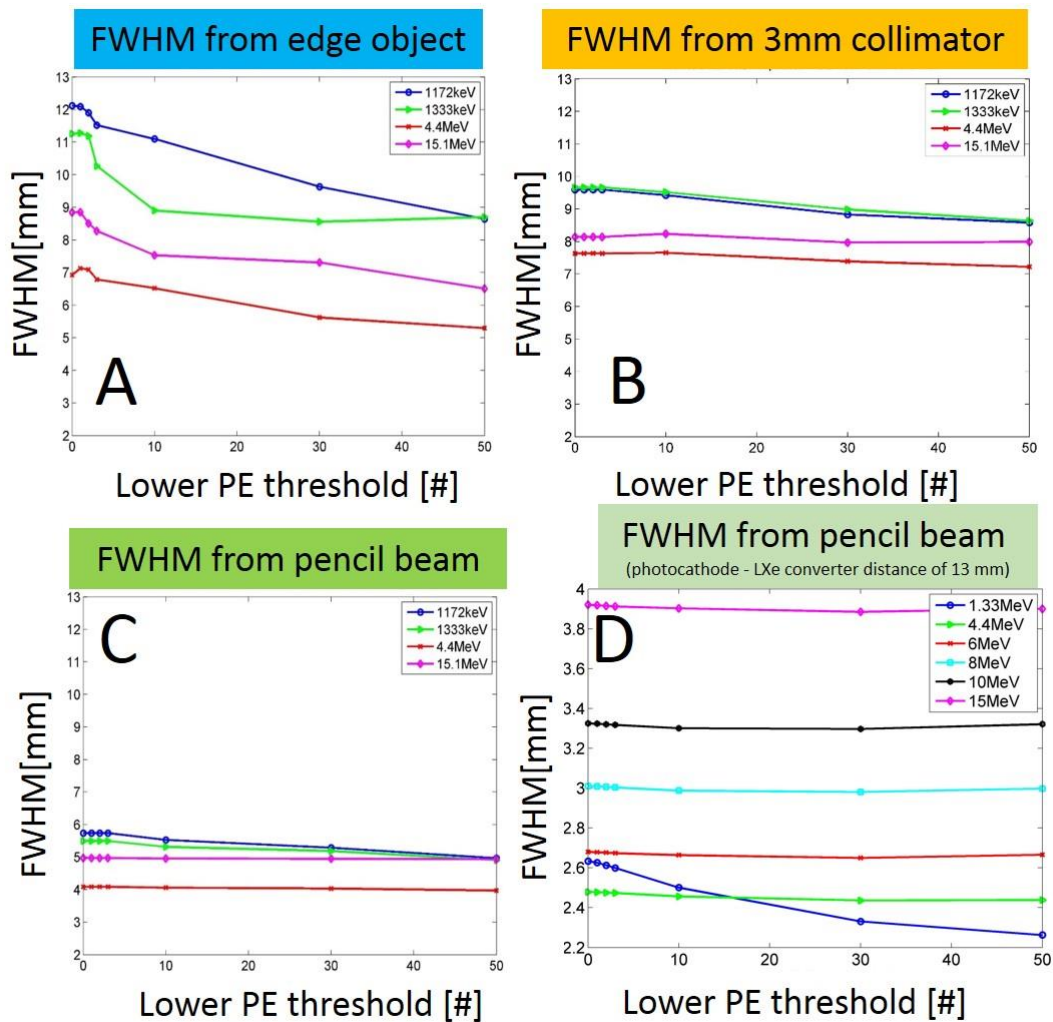


Figure 49: FWHM values of the PSF vs lower PE threshold, for the relevant gamma energies. The PSF was estimated from object-edge imaging (A), imaging of a 3mm diameter collimated beam (B), imaging of a pencil beam in the present experimental configuration (C) and imaging of a pencil beam in the photocathode - LXe converter distance of 13 mm (D); PDE_{GPM} value was estimated as 10%.

5.3.2 Simulation of gamma imaging of a narrow beam and a pencil beam

The gamma imaging properties were simulated with a collimated ^{60}Co source ("narrow beam"), in a geometry equal to that of the experiments described above; the CsI photocathode was located 32 mm away from the LXe converter and the source was located in a Pb cylinder ($\phi=100$ mm, height=160 mm, with a hole $\phi=3$ mm). It was positioned at the center of the OVC bottom, ~ 200 mm away from the capillaries-converter bottom. The distance between the source and the converter's bottom was 347 mm, resulting in a beam diameter of ~ 7 mm and ~ 8 mm, at the converter's bottom and top, respectively.

In addition, we simulated the ultimate PSF resolution by irradiating the detector center with a gamma pencil beam ("infinitesimally thin beam"). The simulations were performed for the present experimental configuration, in which the CsI photocathode was located 32 mm away from the LXe converter, and for a preferable configuration where the photocathode - LXe converter distance was 13 mm.

Figure 50(A, B, C) shows collimated narrow-beam to flat-image COG-histogram-ratios, calculated for 1.33, 4.4 and 15.1 MeV gamma-rays. In these figures the lower PE threshold was set to 30PEs. The color map indicates the transmission of the incidence radiation, relative to "flat irradiation" with an un-collimated source, located on the floor, at ~ 109 cm from the converter's bottom. Profiles through the center ($y=0$) of the distributions are shown in Figure 50(D, E, F), for narrow-beam with a Gaussian fit.

Similar simulation-results for the pencil beam are shown in Figure 51 and Figure 52, for the present experimental configuration (photocathode - LXe converter distance is 32 mm) and for a preferable configuration (photocathode - LXe converter distance is 13 mm), respectively. Here, the COG-histogram was not divided by the flat irradiation one since for pencil beam there is no need to correct for the non-homogeneity of the detector. Note that in the simulation of the preferable configuration, the pencil beam impinging point was averaged on various points on the capillaries.

Figure 49B, C and D summarizes the PSF FWHM values, estimated for narrow-beam and pencil-beam imaging, for few lower PE thresholds. The FWHM values did not vary significantly with the lower PE threshold; their values, for the narrow gamma beam, are ~ 9 mm, ~ 7 mm and ~ 8 mm for gamma-ray energies of 1.33, 4.4 and 15.1 MeV, respectively. For the gamma pencil beam, in the present experimental

configuration (photocathode - LXe converter distance of 32 mm), the estimated FWHM values are ~ 4 mm for 4.4 MeV and ~ 5 mm for the other energies (1.17, 1.33 and 15.1 MeV).

For the gamma pencil beam, in the preferable configuration (photocathode - LXe converter distance of 13 mm), the estimated FWHM values are ~ 3 mm for 1.33 and 4.4 MeV and ~ 4 mm for 15.1 MeV. Note that in these simulations, the pencil beam impinging point was averaged on various points on the capillaries plane.

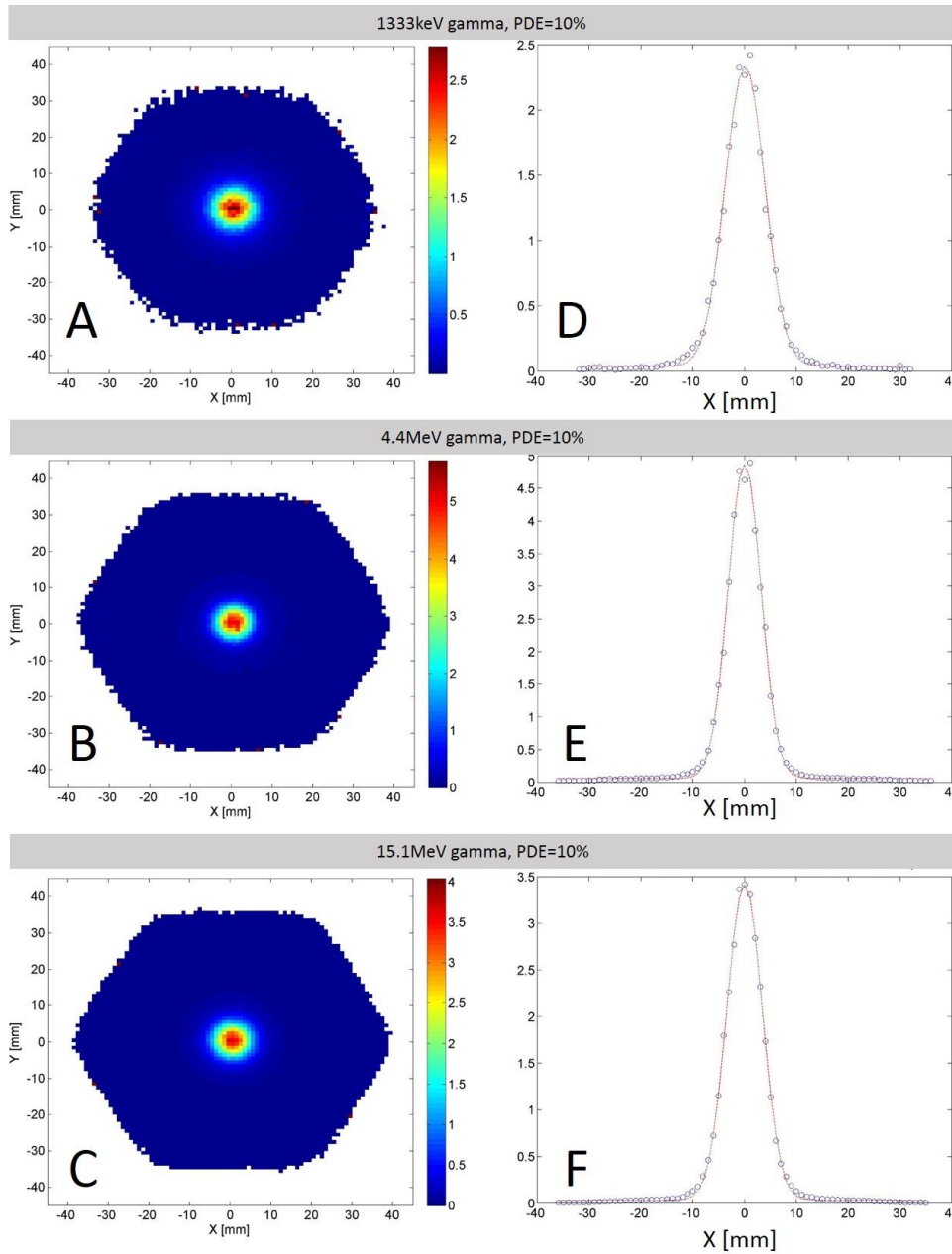


Figure 50: Simulation results of gamma imaging of a narrow beam, for gamma energies of 1.33, 4.4 and 15.1 MeV, calculated for the present experimental configuration (photocathode - LXe converter distance is 32 mm). Lower PE threshold was set to 30PE. A, B and C: narrow-beam to flat-image COG-histogram-ratios. D, E and F: profiles at ($y=0$) with fit to a Gaussian.

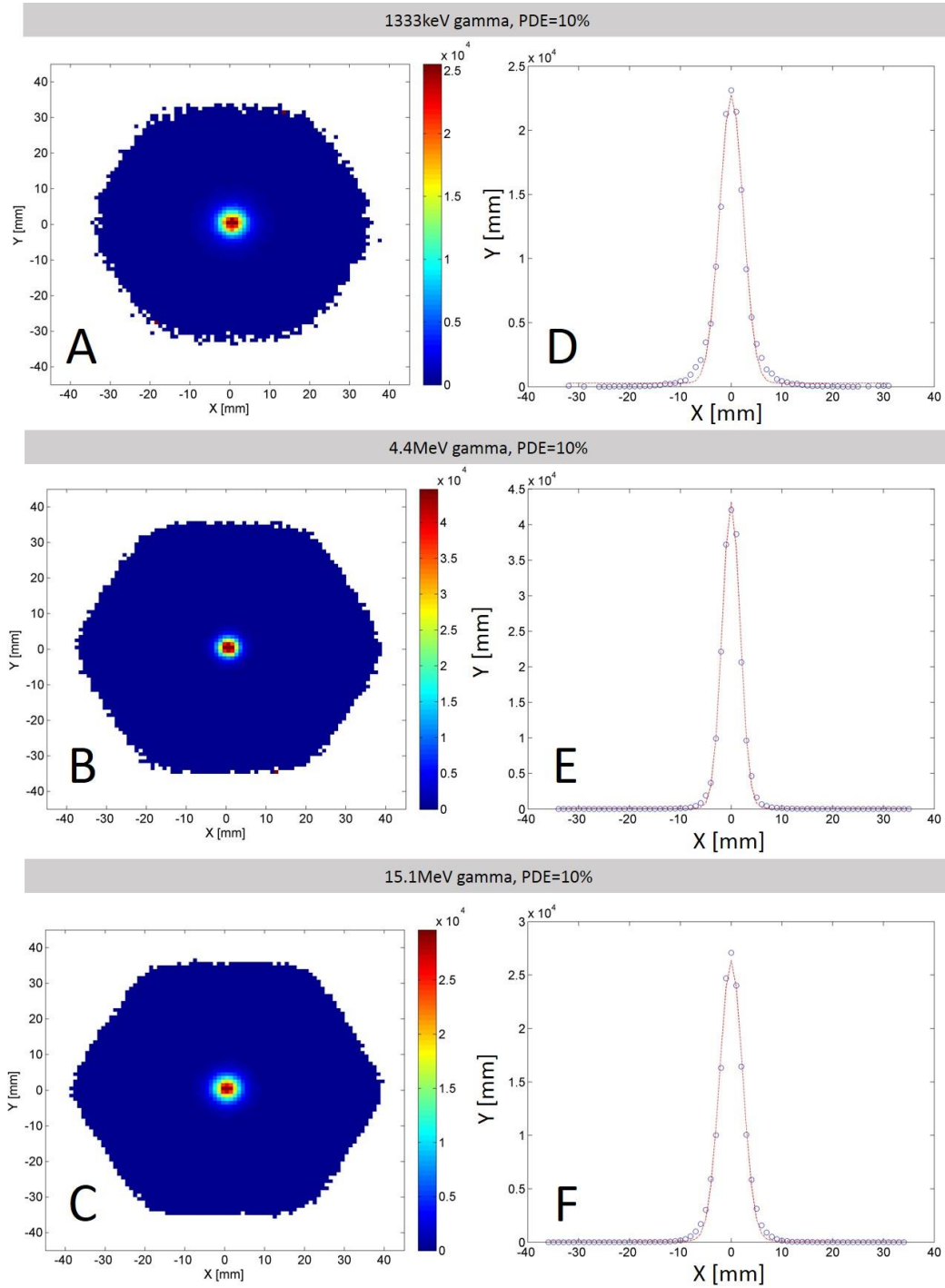


Figure 51: Simulation results of gamma imaging of a pencil beam, for gamma energies of 1.33, 4.4 and 15.1 MeV, calculated for the present experimental configuration (photocathode - LXe converter distance is 32 mm). Lower PE threshold was set to 30PE. A, B and C: pencil-beam COG-histogram. D, E and F: profiles at ($y=0$) with fit to a Gaussian.

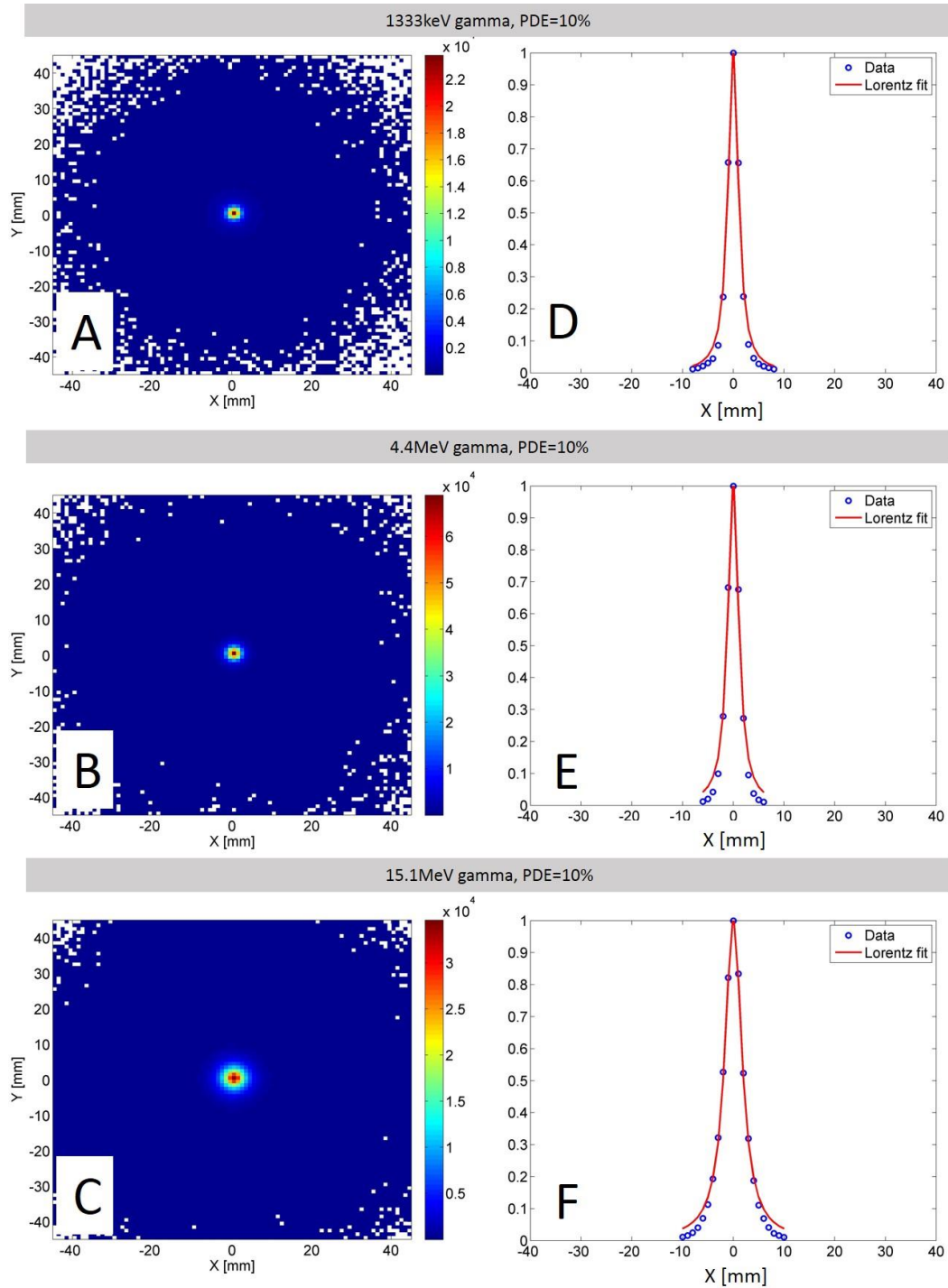


Figure 52: Simulation results of gamma imaging of a pencil beam, for gamma energies of 1.33, 4.4 and 15.1MeV, calculated for the experimental configuration and photocathode - LXe converter distance of 13 mm. Lower PE threshold was set to 30PE. A,B and C: pencil-beam COG-histogram. D, E and F: profiles at ($y=0$) with fit to a Lorentzian. Note that in these simulations, the pencil beam impinging point was averaged on various points on the capillaries.

5.3.3 Simulation of neutron imaging of a pencil beam

We simulated the ultimate detector response to a pencil beam of AmBe neutron's energies (0-11 MeV), irradiating the center of the bottom flange of the OVC (of Figure 13).

Figure 53(A, B, C) shows pencil-beam COG-histogram, calculated for few neutron-energy ranges. As for the gamma-rays, the COG-histograms were not normalized to flat irradiation since there is no need to correct for detector's non-homogeneity. The lower PE threshold was set to 30PEs, as increasing the threshold did not improve the FWHM significantly (see Figure 55A). The color map indicates the number of counts. Profiles through the center ($y=0$) of the distributions are shown in Figure 53(D, E, F), with a Lorentzian fit. In order to learn the effect of neutron scattering on the stainless-steel parts of the WILiX setup, similar simulations were done, without these parts.

Similar simulation-results for the pencil beam are shown in Figure 54, for a preferable configuration in which the photocathode - LXe converter distance is 13 mm. Note that in the simulation of the preferable configuration, the pencil beam impinging point was averaged on various points on the capillaries.

Figure 55A summarizes the PSF FWHM values, estimated for the pencil beam imaging for selected neutron energy-ranges and for few lower PE thresholds, for the present experimental configuration (photocathode - LXe converter distance of 32 mm). The FWHM values did not vary significantly with the lower PE threshold; their values are 11-15 mm for neutron energies of 1-11 MeV. Excluding, in the simulations, the stainless steel parts improved the FWHM only by ~1 mm.

The PSF FWHM values, estimated for the pencil beam imaging for selected neutron energy-ranges and for few lower PE thresholds, for a preferable configuration, in which the photocathode - LXe converter distance is 13 mm, are summarized in Figure 55C. Note that in these simulations, the pencil beam impinging point was averaged on various points on the capillaries. The FWHM values did not vary significantly for most energies with the lower PE threshold; their values are ~2 mm for neutron energies of 4-14 MeV.

The neutron pencil-beam results irradiating the present detector configuration are much worse than the values estimated for the "general" large detector (~2 mm, see magenta graph in Figure 36A). However the results of the preferable configuration are similar

to those estimated for the "general" large detector. The matter will be discussed in section 5.3.5).

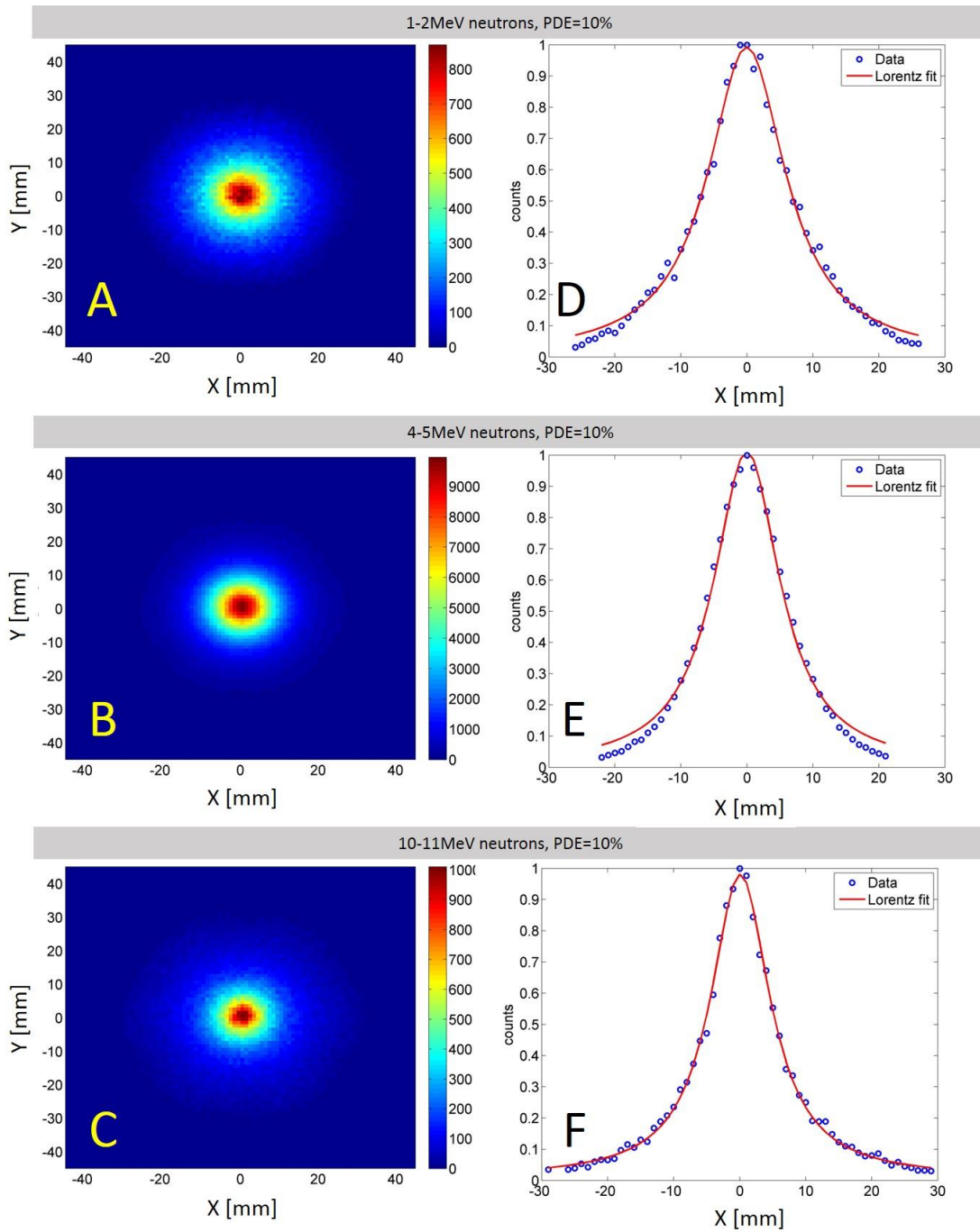


Figure 53: Simulation results of neutron imaging of a pencil beam, for selected neutron energy ranges of 1-2, 4-5 and 10-11 MeV, calculated for the present, not optimal, experimental configuration (photocathode - LXe converter distance is 32 mm). Lower PE threshold was set to 30 PE. A, B and C: pencil beam 2D COG-histograms. D, E and F: profiles at ($y=0$) with fit to a Lorentzian.

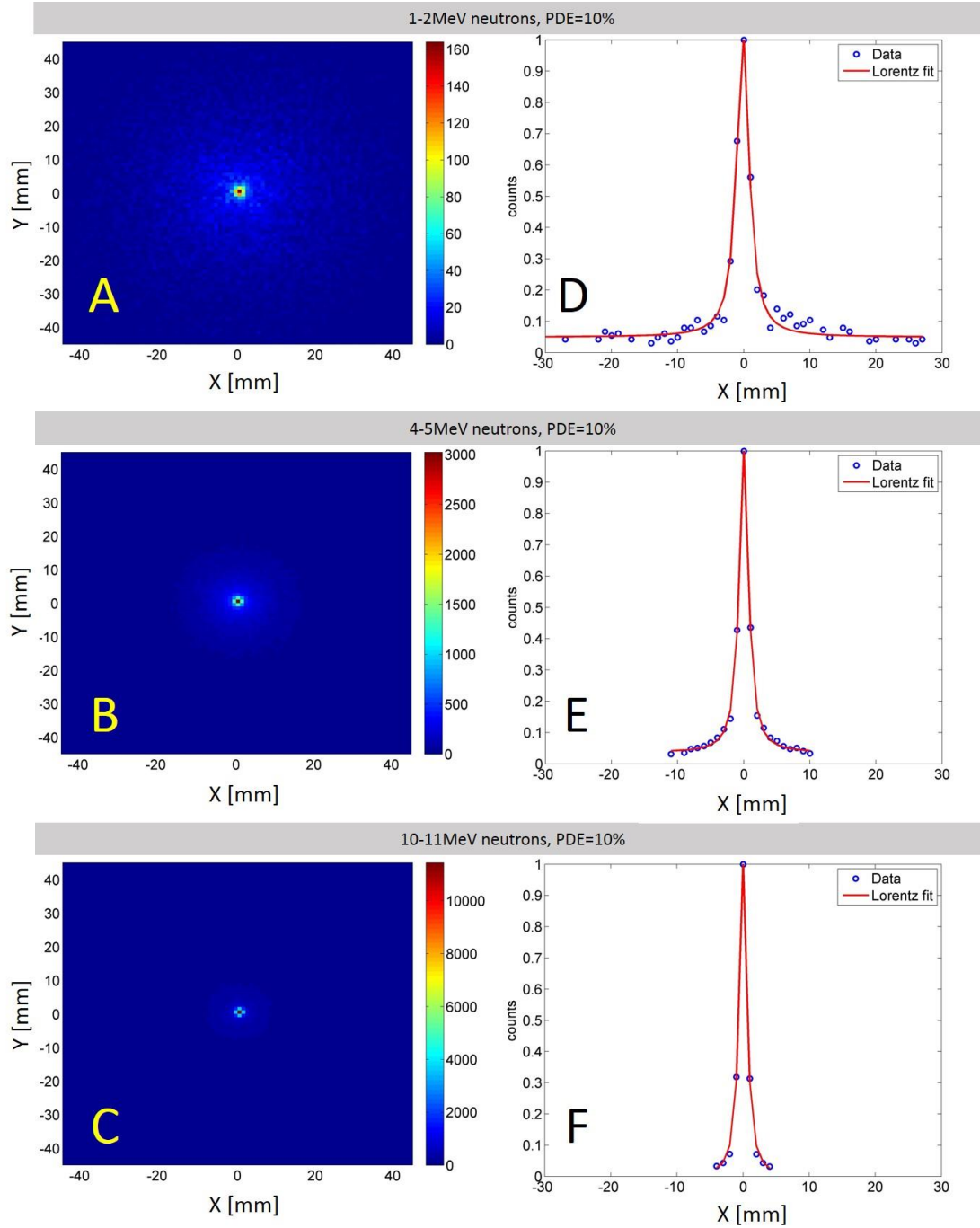


Figure 54: Simulation results of neutron imaging of a pencil beam, for selected neutron energy ranges of 1-2, 4-5 and 10-11 MeV, calculated for preferable experimental configuration (photocathode - LXe converter distance of 13 mm). Lower PE threshold was set to 30 PE. A, B and C: pencil beam 2D COG-histograms. D, E and F: profiles at ($y=0$) with fit to a Lorentzian. Note that in these simulations, the pencil beam impinging point was averaged on various points on the capillaries.

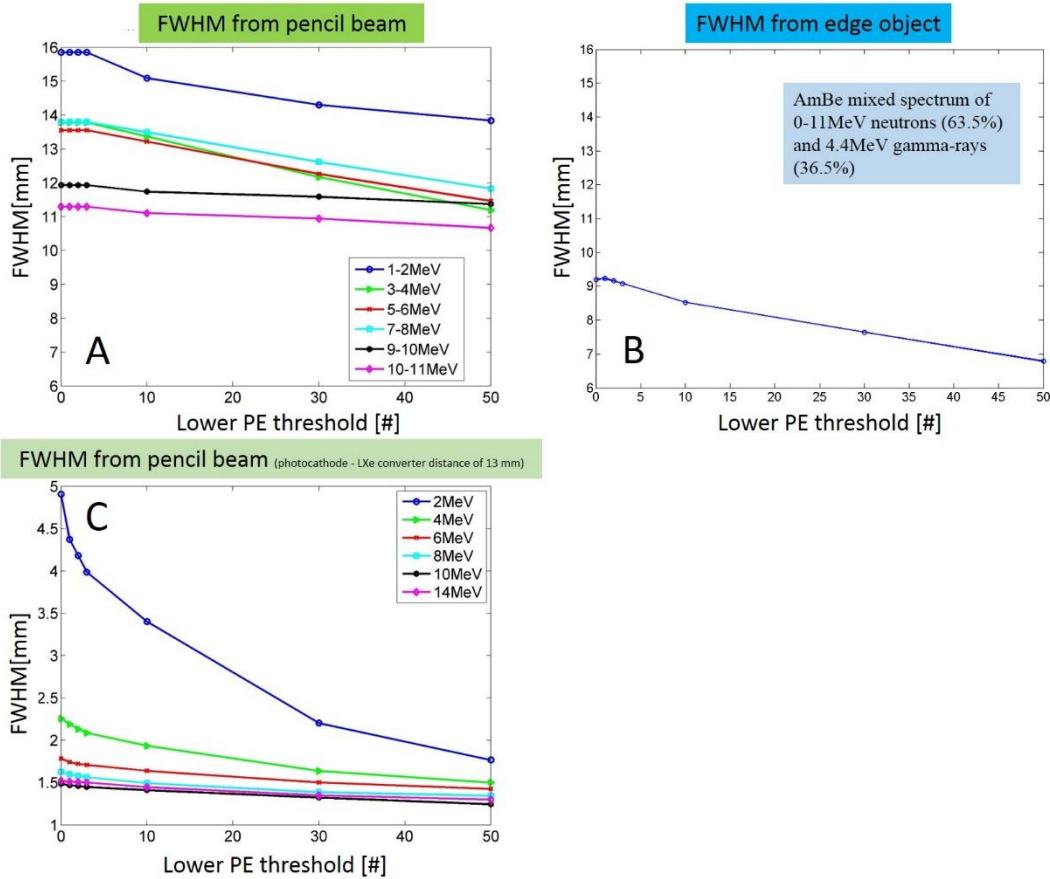


Figure 55: FWHM of the PSF, simulated for few lower PE thresholds, assuming $PDE_{GPM}=10\%$. A: estimated by neutron pencil beam of selected neutron energy ranges for the present experimental configuration. B: estimated by Pb object-edge imaging with AmBe mixed spectrum of 0-11 MeV neutrons (63.5%) and 4.4 MeV gamma-rays (36.5%) for the present experimental configuration. C: estimated by neutron pencil beam of selected neutron energy ranges for photocathode - LXe converter distance of 13 mm.

5.3.4 Simulation of mixed neutron and 4.4MeV gamma-ray imaging of a Pb edge absorber

Figure 56A shows object-to-flat irradiation COG-histogram-ratios, simulated for a mixed radiation field of an AmBe source (neutrons of 0-11 MeV and gamma-rays of 4.4 MeV; ratio gamma-to-total-neutrons: $R_{\gamma/n}=0.575$ [90]), irradiating a Pb-object edge (12 mm thick) covering half of the detector (as described in detail in section 4.7.2 above).

In these simulations, the lower PE threshold was set to 30PEs. The color map indicates the transmission of the incidence radiation, relative to case of no object. One can clearly see the covered area of the detector. The simulated transmission of the neutrons and gamma through the 12mm Pb is 0.7, in agreement with the theoretical value of ~ 0.69 .

The average profile of the edge, the ESF, is shown in Figure 56B along with a fit to a logistic function (Equation 18). The PSF, obtained by differentiating the logistic function fitted to the ESF, is shown in Figure 55B, for few lower PE thresholds. The FWHM slightly improves with increasing the lower PE threshold, with best value of ~ 7 mm. This value is close to that expected for a combination of 63.5% of neutrons, with $\text{FWHM} \approx 12$ mm (see Figure 55A), and 36.5% of 4.4 MeV gamma-rays, with $\text{FWHM} = 4$ mm (see Figure 49C).

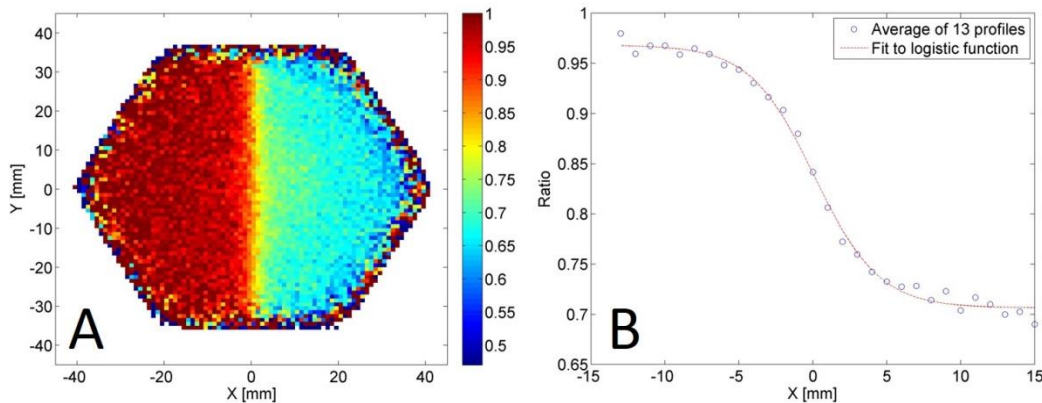


Figure 56: Simulation results of a 12mm thick Pb object-edge imaging, with mixed field of 0-11 MeV neutrons and 4.4MeV gamma-rays. Lower PE threshold was set to 30PEs. A: object to flat COG-histogram-ratios. B: average edge profiles with fit to a logistic function.

5.3.5 Comparison between simulation FWHM results of the "general" large detector and the small size laboratory detector prototype

As mentioned above (section 5.3.3), the FWHM simulation results for irradiating the current small experimental setup in WILiX with 1-11 MeV neutron pencil-beam (11-15 mm, see Figure 55A) are much broad than the values estimated for the "general" large detector (~ 2 mm, see magenta graph in Figure 36A). The main reason for this FWHM difference is statistical effect of the PEs population. The number of the PEs in the small detector configuration is smaller than that in the "general" detector due to the following: 1. the distance between the CsI photocathode and the UV-window in small detector configuration is relatively large (32 mm) compared to the distance in the "general" detector (5 mm), reducing dramatically the number of scintillation photons reaching the photocathode, 2. the neutrons scintillation light yield and photon detection efficiency, assumed in the small detector setup simulations (neutrons scintillation light yield of 4 photons/keV and $\text{PDE}_{\text{GPM}} = 10\%$) were smaller compared to these values

assumed in the "general" detector simulations (neutrons scintillation light yield of 8.8 photons/keV and $PDE_{GPM}=20\%$); Another reason for the FWHM broadening is the dependence of the FWHM on the impinging point of the gamma/neutron beam on the capillaries (see 5.2.4). In the "general" detector simulations, wide beam was simulated, while in the small detector pencil beam simulations the beam was infinitesimal and impinged the center of the capillary.

6 Results and discussion

6.1 Point-like UV-photon imaging at room temperature

As noted above, this experiment involved only the GPM, operated at room temperature with Ne/5%CH₄; it was irradiated with a point-like UV-source, as described above (section 4.4). For different numbers of PEs (obtained by adjusting the UV photon-flash intensity), spectra of the total charge were recorded from all the GPM pads, event-by-event (i.e. for each lamp discharge) (see Figure 57). As expected the charge spectrum takes the shape of a Gaussian-like for large number of PEs, while for few PEs the shape is of a decaying exponent.

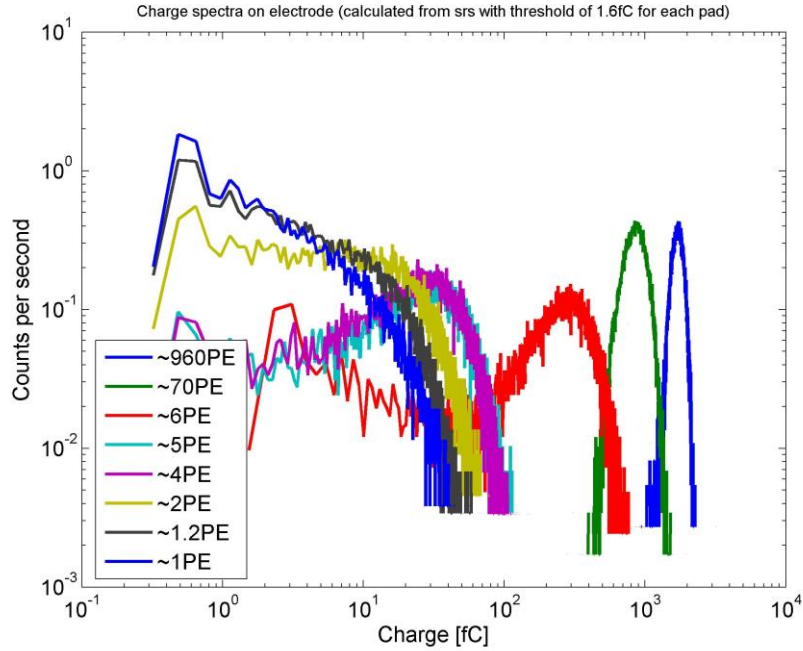


Figure 57: Spectra of the total charge collected in all 61 pads of the readout electrode, for different numbers of photoelectrons per UV-lamp burst. In these measurements, the extraction efficiency from the photocathode was maintained constant. Triple-THGEM GPM; Ne/5%CH₄; $p=1000$ mbar (flow mode); $T=298K$.

COG histograms were calculated according to Equation 15, with charge threshold of 1.6 fC in each pad. A number of 2D COG histograms, measured with a double- THGEM GPM for different number of photoelectrons, are shown in Figure 58. Similar histograms were measured with a triple-THGEM GPM. The broadening of the COG distribution with the decreasing number of photoelectrons is evident. The spots in Figure 58F are in the hexagonal-pads' centers, representing the fact that in each event only single photoelectron was measured, hence only a single pad gave a signal.

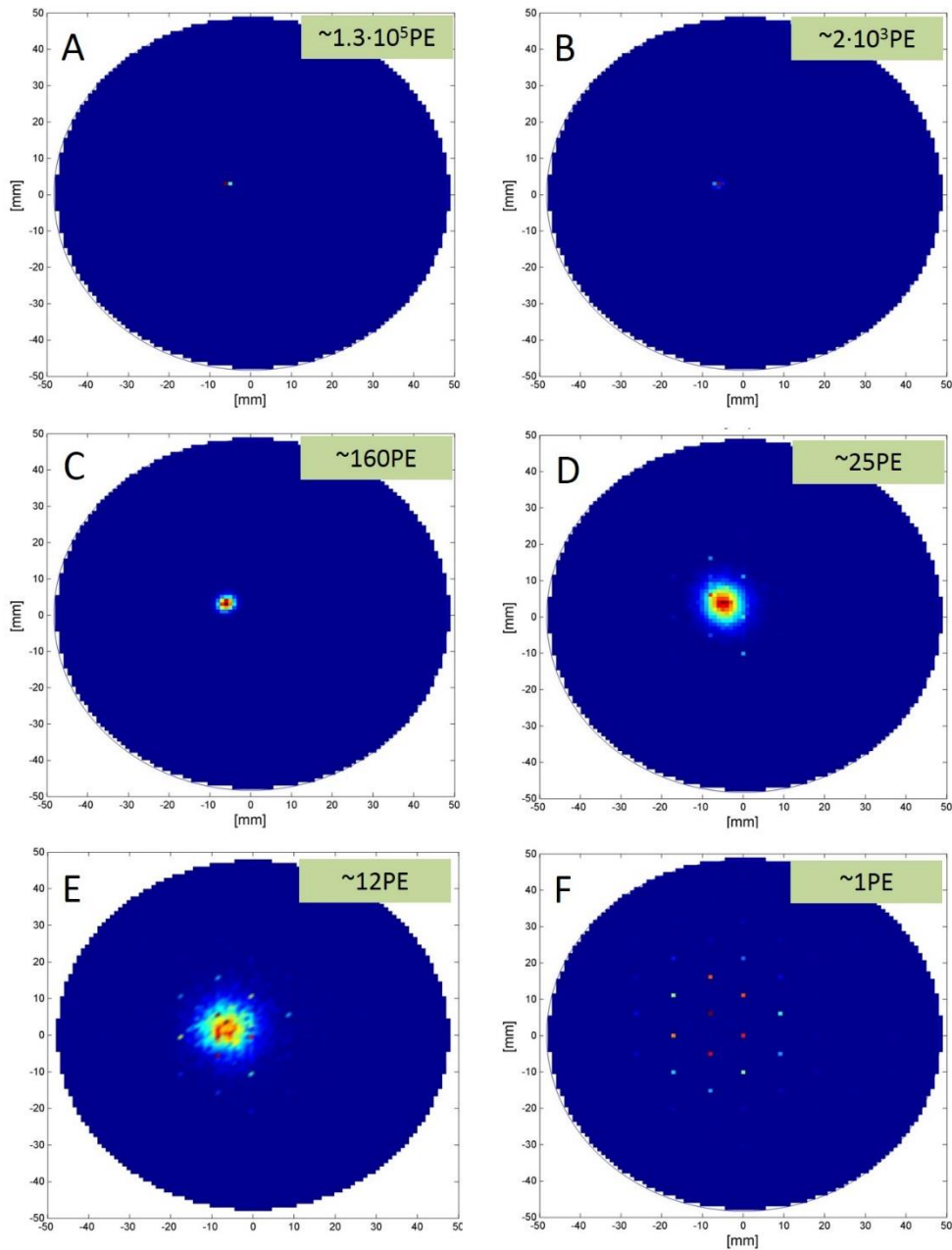


Figure 58: 2D COG histograms, measured with a double-THGEM GPM for different numbers of photoelectrons, resulting of the detector irradiation with UV-photon flushes. The colors represent the number of events. The broadening of the distribution with the decreasing number of photoelectrons is significant. The spots in figure F, in the hexagonal-pads' centers, represent the fact that in each event only a single photoelectron was measured, illuminating a single pad.

Position profiles along the center of the 2D COG histograms, determined for various numbers of PEs, are shown in Figure 59, for data recorded with double-THGEM (A) and triple-THGEM (B) GPMs. The FWHM values, calculated from these measured profiles, versus number of PEs, are shown in Figure 60, and listed in

Table 9, along with GEANT4 results. Note the good agreement between simulation and experiment results. The results of both, verified and constant extraction efficiencies, are similar since only the number of PEs per event influence the profile's width.

The statistics of the number of PE significantly affects the distributions widths, below ~ 100 PEs per pulse.

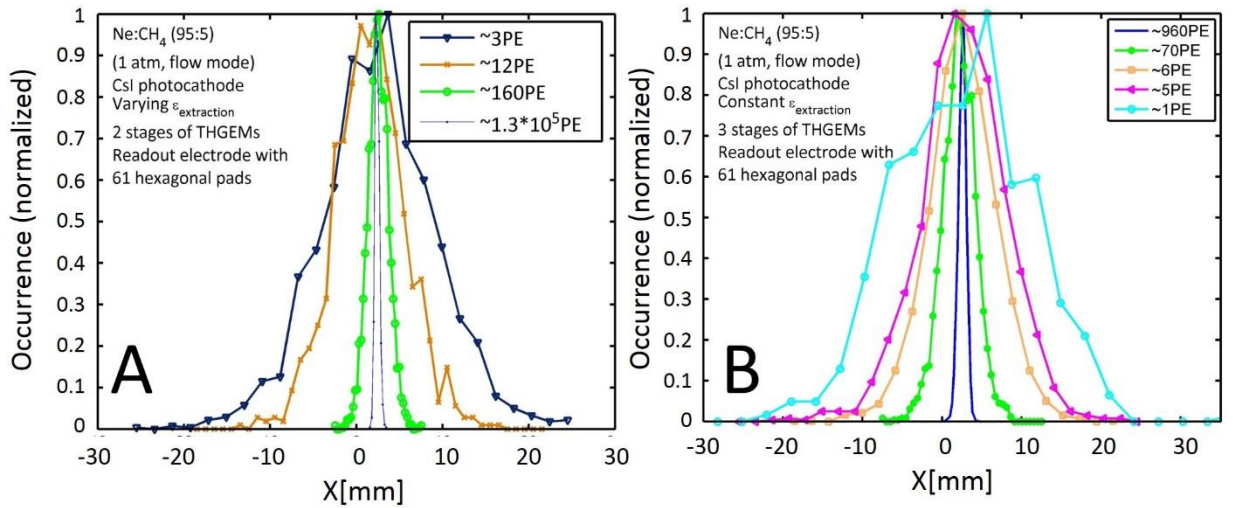


Figure 59: Profile along the x -axis of the COG histograms measured with varying extraction efficiency in double-THGEM GPM (figure A) and with constant extraction efficiency in triple-THGEM GPM (figure B) for different numbers of UV-induced photoelectrons per lamp burst. Ne:CH₄; $p=1000$ mbar (flow mode); $T=298$ K.

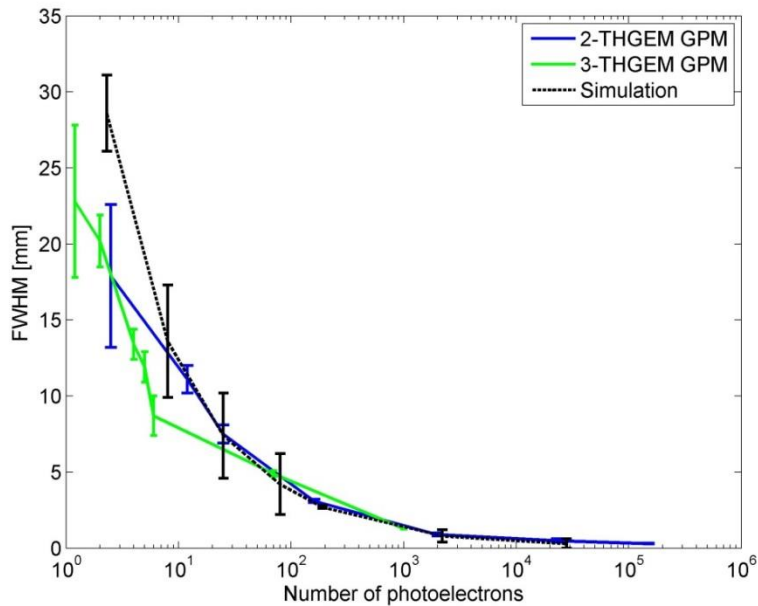


Figure 60: Summary of the measured and simulated COG distribution widths (FWHM) (experimental data of Figure 59), versus the number of photoelectrons. Ne/5%CH₄; $p=1000$ mbar (flow mode); $T=298$ K.

Table 9: The measured and simulated UV-induced COG distribution widths versus the number of photoelectrons. $Ne/5\%CH_4$; $p=1000$ mbar (flow mode); $T=298K$. Data compilation from Figure 60.

2-THGEM GPM		3-THGEM GPM		Geant4 simulations	
Number of PE	FWHM [mm]	Number of PE	FWHM [mm]	Number of PE	FWHM [mm]
$\sim 1.3 \cdot 10^5$	0.3 ± 0.03	~ 1000	1.3 ± 0.04	$\sim 2.8 \cdot 10^4$	0.3 ± 0.3
$\sim 2.3 \cdot 10^4$	0.5 ± 0.1	~ 70	4.9 ± 0.2	~ 2200	0.8 ± 0.4
~ 2000	0.9 ± 0.1	~ 6	8.7 ± 1.3	~ 190	2.7 ± 0.1
~ 160	3.1 ± 0.1	~ 5	11.9 ± 1.0	80	4.2 ± 2.0
~ 25	7.5 ± 0.6	~ 4	13.4 ± 1.0	~ 25	7.4 ± 2.8
~ 12	11.1 ± 0.9	~ 2	20.2 ± 1.7	8	13.6 ± 3.7
~ 2.5	17.9 ± 4.7	1.2	22.8 ± 5.0	2.3	28.6 ± 2.5
~ 2	17.7 ± 19.1	1	-	~ 1	-
~ 1	-				

According to the gamma-ray simulations (see Table 7), the average numbers of PE, in current the experimental setup, are ~ 30 for 1.33 MeV, ~ 100 for 4.4 MeV and ~ 300 for 15.1 MeV. For these numbers of PE, the broadening of the COG distribution width, due only to statistical effects, would be ~ 7 mm, ~ 4 mm and ~ 3 mm, respectively (see Figure 60). On the other hand, the FWHM values, calculated from the gamma pencil beam simulations (with no lower PE threshold), were ~ 6 mm, ~ 4 mm and ~ 5 mm, respectively (see Figure 49C); this indicates that further broadening, due to gamma scattering inside the detector, is rather significant for the 15.1MeV gamma-rays but not for lower gamma-ray energies.

Prior to the gamma and neutron imaging described above, imaging experiments were also performed at cryogenic conditions with an ^{241}Am α -source immersed within the LXe vessel, yielding on the average of ~ 400 PEs/ α event (see section 8.4 in the appendices).

6.2 Gain measurements

6.2.1 Ne/CH₄(5%)

Gain measurements in pulse mode, with a triple-THGEM GPM installed in WILiX, were performed by shining single-UV photons from a DC D₂ lamp, as described above (see section 4.5). The gain was estimated by fitting an exponential function to the resulting pulse-height distributions of the charge recorded (see Figure 61). Figure 62 shows the measured GPM gain curves for Ne/CH₄(5%) at room and cryogenic temperatures, at different gas pressures.

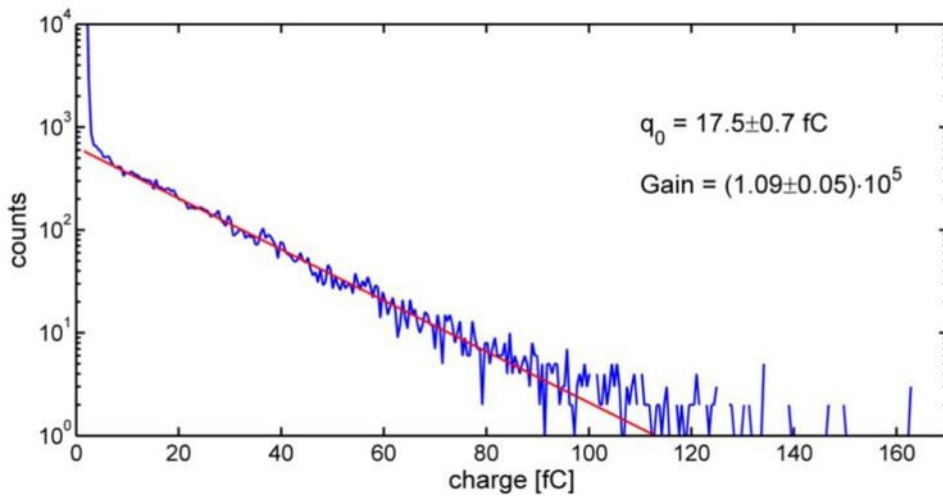


Figure 61: Typical single-photoelectron charge spectrum obtained with the Triple-THGEM GPM configuration (blue) and an exponential fit (red).

Naively, one would expect convergence of two gain curves, measured at RT and cryogenic temperature with the *same gas density* (e.g. 552 torr @294 K (blue circles) with 397 torr @210 K (Blue triangles), or 763 torr @294K (red squares) with 576 torr @222 K). However, as shown in Figure 62, these gain curves do not coincide (in the figure, the gain curve at 763 torr @294 K converges with that of 500 torr @222 K and not with that at 576 torr). Furthermore, the maximal stable gain achieved at RT is higher than that at cryogenic temperatures. Possible explanation would be the large temperature gradient across the GPM (~200K-to-RT across 180mm) causing significant gas density gradient across the GPM.

At room temperature, maximal gain of $\sim 4 \cdot 10^5$ was measured at 756 torr and $\sim 4 \cdot 10^6$ at 552 torr. At cryogenic temperatures, maximal gain of $\sim 6 \cdot 10^5$ was measured at 397 torr. These values assure high single-photon detection efficiency and are well

sufficient for gamma and neutron imaging measurements, even in cases where only a single photon starts an avalanche above a readout pad.

For the gamma and neutron experiments, in which the average number of PEs per event is higher than single photon (see Table 7 and Table 8), detector gains of $2\text{-}4\cdot 10^4$ are sufficient.

Note that during the studies described here (prolonged measurements over several months), the THGEM had accumulated a considerable ‘history’ of occasional discharges, which possibly caused some electrode "aging", thus constrained operation at lower bias values, hence, at lower maximal gains.

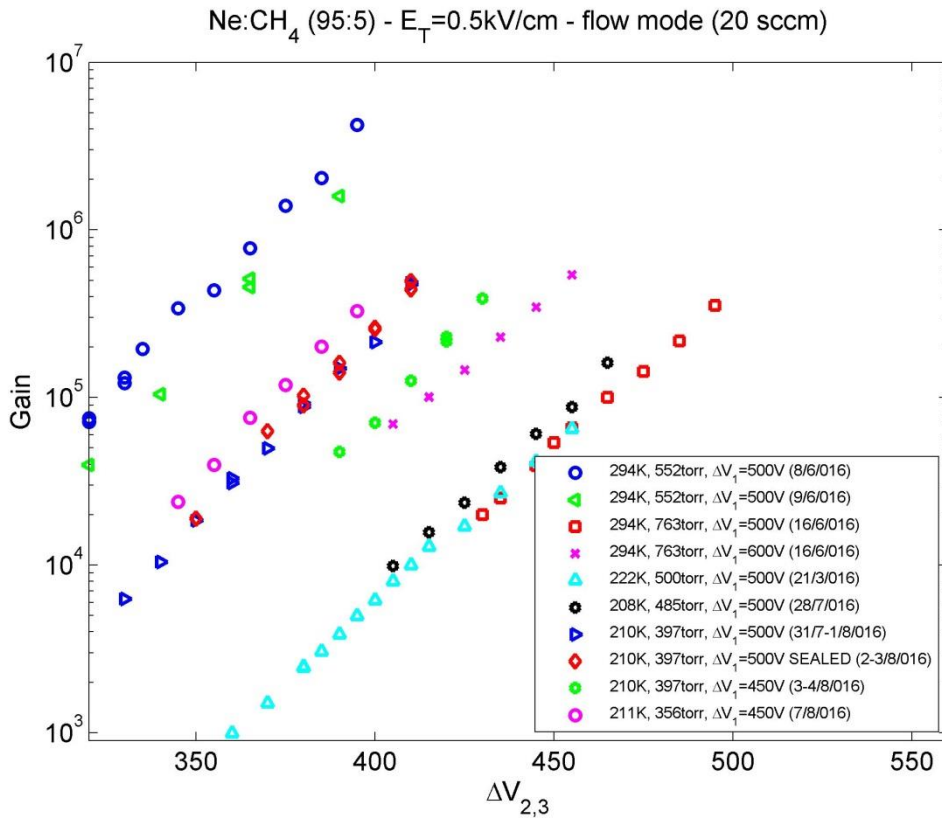


Figure 62: Gain curves, measured in pulse-counting mode, of the triple-THGEM GPM with Ne/CH₄(5%) at room and cryogenic temperatures and different pressures, vs. the equal voltage values $\Delta V_{2,3}$ applied across the second and third GPM stages (see Figure 14). The voltage values across the first THGEM, ΔV_1 , are given in the inset; the induction and transfer fields were 0.5kV/cm in all cases. Uncertainties are smaller than symbols sizes

6.2.2 He/CF₄ and He/CH₄ mixtures

Gain curve and extraction efficiencies in Helium based mixtures were also investigated only at room temperature. Gain curves, measured in current mode, are shown in Figure 63 for a single-THGEM + CsI photocathode deposited on its top electrode, operated under different He/CF₄ and He/CH₄ mixtures. The effective gain is represented as a function of the voltage difference applied to the THGEM electrodes. As seen from Figure 63, both types of gas mixtures allow reaching very high charge-gains, well above 10⁵. Similar gains are obtained in both types of He-based mixtures but higher voltages are necessary for the He CH₄ mixtures: maximum gains are obtained for CF₄ content around the 20–30% while for CH₄ the content must be above 30%. This trend and the achieved gains are similar to those obtained for Ne-based mixtures for THGEMs with similar parameters, e.g. [52, 84]; the differences in the maximum applied voltages needed in the different publications may result from different levels of gas purity, as demonstrated in [84] and [101]. On the other hand, when compared to Ar-based mixtures [52, 84, 102, 103], He-based mixtures allow to achieve similar gains but needing much lower voltages applied to the THGEM. Note that previous work [70, 84, 102, 103] have shown that the maximum gains achieved in pulse mode, resulting from interactions of X-rays with energies in the keV range, are lower than those achieved in current mode, by a factor that can be up to one order of magnitude.

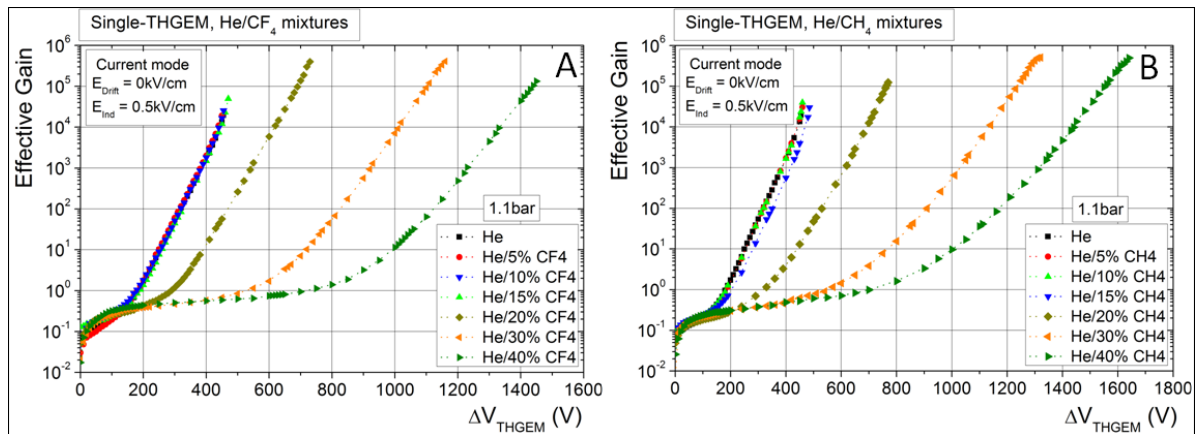


Figure 63: Single-THGEM gain-voltage curves, measured in current mode of photoelectrons emitted from a CsI photocathode coating the THGEM top electrode, for the THGEM operating under several He/CF₄ (A) and He/CH₄ (B) mixtures.

Figure 64 shows the measured photoelectron extraction efficiency from CsI into He/CF₄ (figure A) and He/CH₄ (figure B) mixtures as a function of the electric field above the photocathode. The measured photoelectron currents in gas were normalized to the

vacuum photoelectron current as measured from the CsI photocathode, i.e. the ratio of $I_{\text{gas}}/I_{\text{vacuum}}$. The addition of CF_4 to He is more effective than the addition of CH_4 , in terms of the reduction of photoelectron backscattering, similar to the behavior that found in Ne-based mixtures [84, 85]. This is due to the fact that CF_4 presents lower energy thresholds for the vibrational excitations, resulting in the onset of inelastic collisions at lower photoelectron energies. Compared to Ne-base mixtures with the same molecular additive content, He-based mixtures present lower photoelectron extraction efficiencies. This is a consequence of the higher cross section presented by He for electron impact elastic collisions when compared to Ne. While for He-30% CH_4 mixture the photoelectron extraction efficiency is below 50% for electric fields lower than 2 kV/cm, in Ne-20% CH_4 it is already above 70% for electric fields above 1 kV/cm [84, 85].

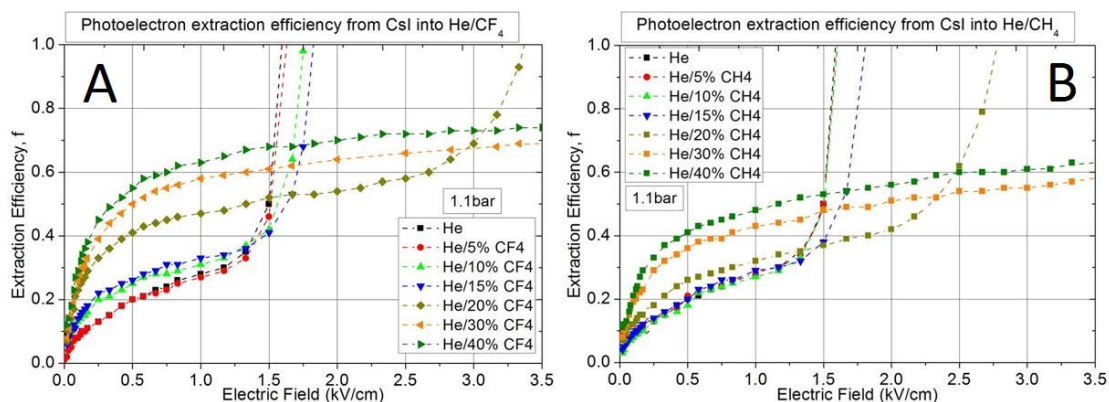


Figure 64: Photoelectron extraction efficiency from CsI into several He/ CF_4 (A) and He/ CH_4 (B) mixtures as a function of the applied electric field in the region above the photocathode. UV photons peaking at 185 nm from a Hg(Ar) VUV lamp were used.

6.3 Gamma-ray imaging experiments

The gamma-ray imaging setup is described above (section 4.6). A typical single gamma-induced event (PE distribution on the pads) is shown (above) in Figure 18E. Distributions of number of "firing" pads, with charge thresholds of 0.8 fC and above 1.6 fC are shown, for a few detector gains, in Figure 65. The average numbers of "firing" pads are listed in Table 10. The average number of "firing" pads does not vary significantly with the gain, indicating that the gain is sufficiently high.

Spectra of the total UV-photon charge induced by (^{60}Co) gamma-interactions in the LXe converter/scintillator, were recorded from all the GPM pads, event-by-event, for

different GPM-detector gains (Figure 66). The spectra have exponential shapes, as expected from the simulations (see blue and black spectra in Figure 45C), due to the relatively small number of PEs and avalanche statistics. The low charge cut-off is not sharp due to noisy trigger signals fed into the leading edge discriminator from the top THGEM3 electrode (see 4.3).

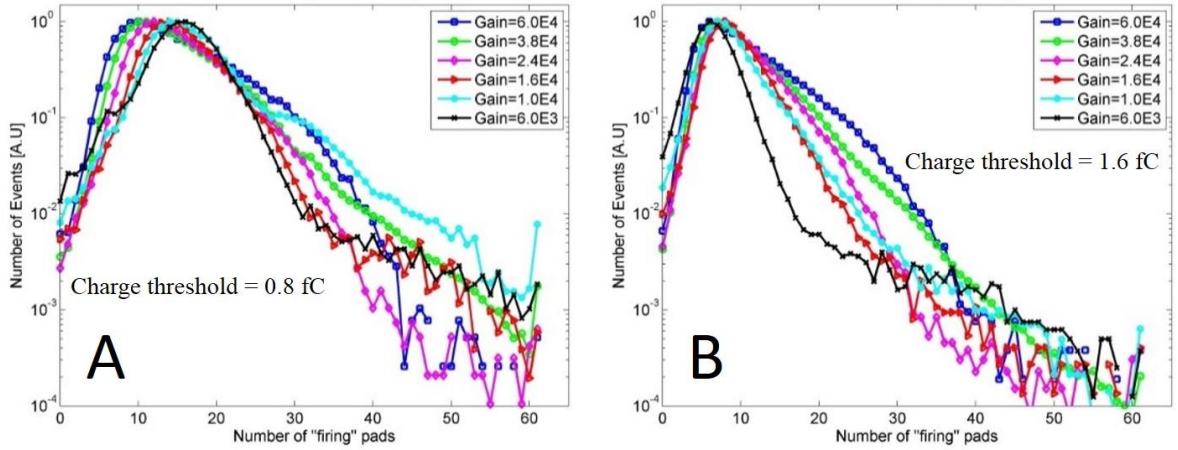


Figure 65: Distributions of number of "firing" pads with (A) charge threshold above 0.8 fC and (B) above 1.6 fC, for different gains, as measured with a ^{60}Co gamma source located outside of WILiX. The distributions are normalized to their maximum.

Table 10: Average numbers of "firing" pads, with charge above 0.8fC and above 1.6fC, as measured with ^{60}Co source.

Gain [$\cdot 10^3$]	Average numbers of "firing" pads with charge above 0.8fC	Average numbers of "firing" pads with charge above 1.6fC
6	16	7
10	18	9
16	16	10
24	15	10
38	15	10
60	15	11

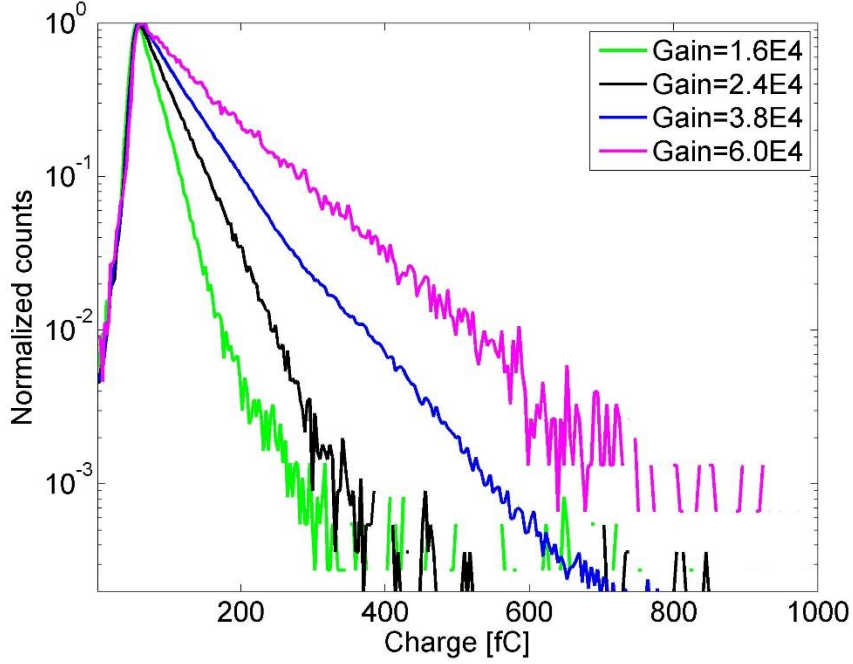


Figure 66: Gamma-ray interactions in the LXe converter (without the Pb edge object): spectra of the total UV-photon induced charge in all GPM pads, calculated offline event-by-event for different detector-gain values. No charge or pad thresholds were applied for the charge spectra.

According to our simulations, the average number of PE for ^{60}Co energies is 30 (see Table 7). On the other hand, the measured average number of "firing" pads with charge above 1.6 fC is 10 (see Table 10), which means that each of the 61 pads will get on average not more than 1-3 PE. Therefore, for each event, the unweighted center of gravity was calculated according to Equation 15, while setting the charge, collected in pad j in event i , to 1 ($Q_{i,j}=1$) for all events.

6.3.1 Gamma-ray imaging experiments of a Pb-object edge

Figure 67A shows the COG histogram, measured with the open ^{60}Co source irradiating a Pb-object edge covering half of the detector area (setup details are in section 4.6). Figure 67B shows the COG histogram, measured with no object (flat image). In these measurements the detector was operated at a gain of 3.8×10^4 ; the charge threshold was set to 1 fC and the pads threshold was set to 10 pads. The color map indicates the number of counts in each 1 mm^2 pixel of the COG histogram.

The resulting ratio image of the Pb edge, calculated according to Equation 19, is shown in Figure 68A. The color map in Figure 68A, indicates the transmission of the incident

radiation with the object, relative to the situation without object. One can clearly see the covered area of the detector.

$$\text{Equation 19} \quad \text{Ratio} = \frac{\left(\frac{\text{Image}_{\text{object}}}{\text{Time}_{\text{object}}} \frac{\text{Image}_{\text{background}}}{\text{Time}_{\text{background}}} \right)}{\left(\frac{\text{Image}_{\text{flat}}}{\text{Time}_{\text{flat}}} \frac{\text{Image}_{\text{background}}}{\text{Time}_{\text{background}}} \right)}$$

The ESF, shown in Figure 68B, is the average profile of the edge image. The expected transmitted fraction of ^{60}Co gamma-rays through the 12 mm Pb object is 45%. In practice, the measured transmission was 55% (see Figure 68B), due to gamma scattering from the detector's uncovered area to the Pb-covered one and also by the object itself. This effect was validated by simulations (see Figure 47D).

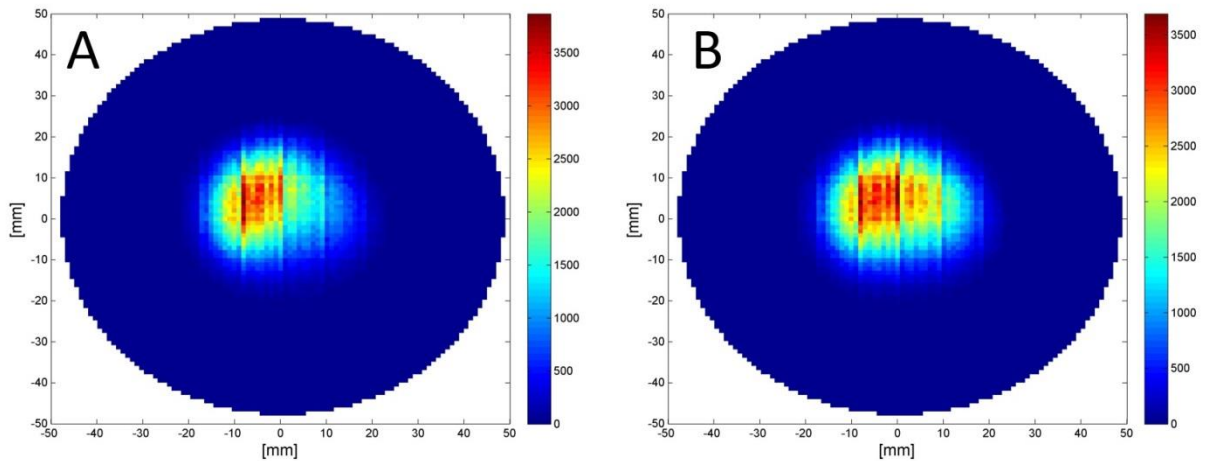


Figure 67: COG histogram, measured with the GPM in the setup of Figure 22B with the ^{60}Co gamma-rays irradiating a Pb object edge covering half of the detector area (A) and with no object (flat image, B). GPM operating conditions: Ne/5%CH₄; p=485Torr (20 sccm flow); T=208K.

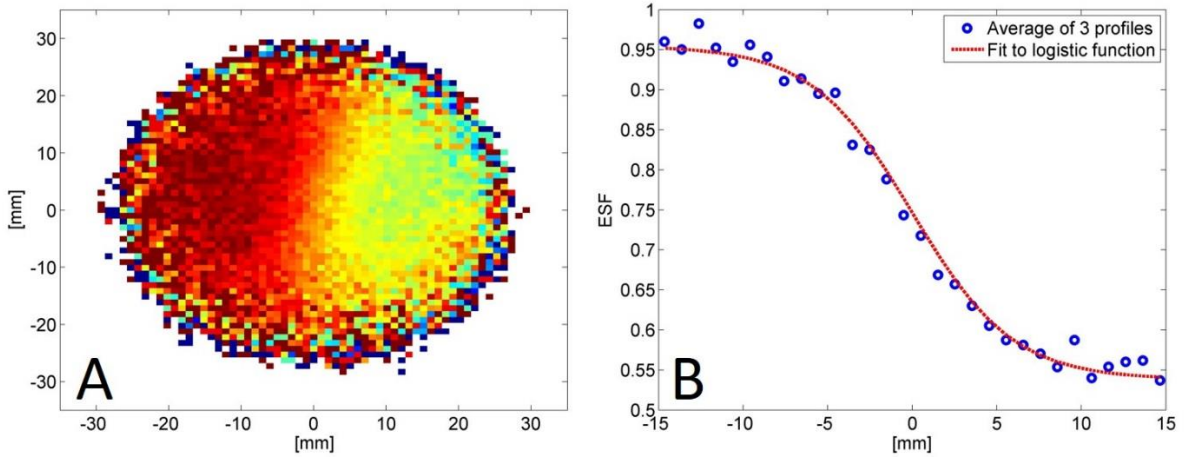


Figure 68: Lead object imaging by gamma-rays emitted from ^{60}Co source in the setup of Figure 22B. A- The 2D image showing the ratio of the object-to-flat image (Figure 67A and B, respectively), calculated according to Equation 19. The color map indicates the transmission of the incident radiation, relative to case of no object. B- Profile and fit to a logistic function (Equation 18). GPM operating conditions: $\text{Ne}/5\%\text{CH}_4$; $p=485\text{Torr}$ (20 sccm flow); $T=208\text{K}$; $\text{gain}=3.8\times 10^4$.

For the Pb-absorber edge irradiation measurements, the PSF was obtained for several pads-threshold values (Figure 69) by differentiating the average profile of the edge, i.e. the edge spread function (ESF) (Figure 68B). Table 11 compares the measured (weighted and un-weighted COG values) and simulated (see 5.3.1) spatial-resolution values in the present experimental geometry. The simulated values agree well with the experimental ones, validating the simulation tools. Note that the “% of total counts” represents the detection efficiency of interacting events in the LXe converter, for a given pads threshold (counting efficiency of converted events). The uncertainty on the measured spatial-resolution values was estimated as $\sim 2\text{mm}$ by the logistic function fit (Equation 18). The PSF values, calculated with un-weighted COG are better than those calculated with the weighted COG, since the un-weighted COG calculation avoids artifact bias due to the exponential distribution of the avalanche process. The PSF values, calculated with un-weighted COG, was $12\pm 2\text{ mm}$ (FWHM) at high detection efficiency (99.1%) compared to pad threshold =0; it is in good agreement to the simulated value for this detector size and geometry. While the PSF value did not improve significantly with increasing pad threshold from 5 to 10, increasing the latter above 5 resulted in considerable loss of efficiency.

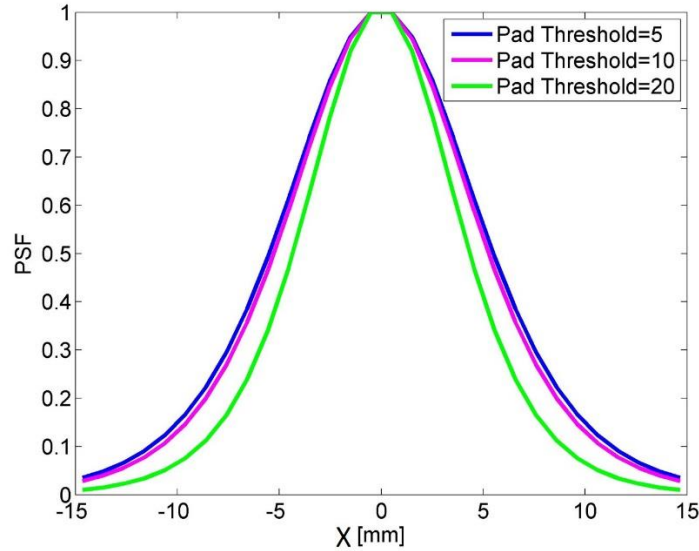


Figure 69: PSF distributions of a ^{60}Co -irradiated Pb edge, for 5, 10 and 20 pads thresholds, as calculated by the derivative of the ESF of the edge measurement (Figure 68B).

Table 11: The measured and simulated spatial-resolution FWHM values resulting from the ^{60}Co -irradiated edge, calculated for three pad thresholds. The % of total counts represents the detection efficiency of interacting events for a given pads threshold (counting efficiency of converted events). The uncertainty on the measured spatial-resolution values is $\sim 2\text{mm}$.

Pad threshold	% of total counts	PSF (FWHM) [mm]		
		Measurement		Simulations
		Weighted COG	Un – weighted COG	
5	99.1	14	12	12
10	71.6	14	11	11
20	14.3	13	9	10

6.3.2 Imaging of a narrow gamma beam

For the collimated ^{60}Co gamma-ray measurements (7 mm diameter spot at the converter base; setup details are in section 4.6), an un-weighted COG-histogram ratio-image of the collimated beam to a flat-irradiation was calculated according to Equation 19 (Figure 70). The *flat* image was measured with an open source, located about a meter below the capillaries-converter. The charge threshold was set to 1 fC and the pads threshold was set to 10 pads. The color map indicates the transmission of the incident radiation, relative to the flat one.

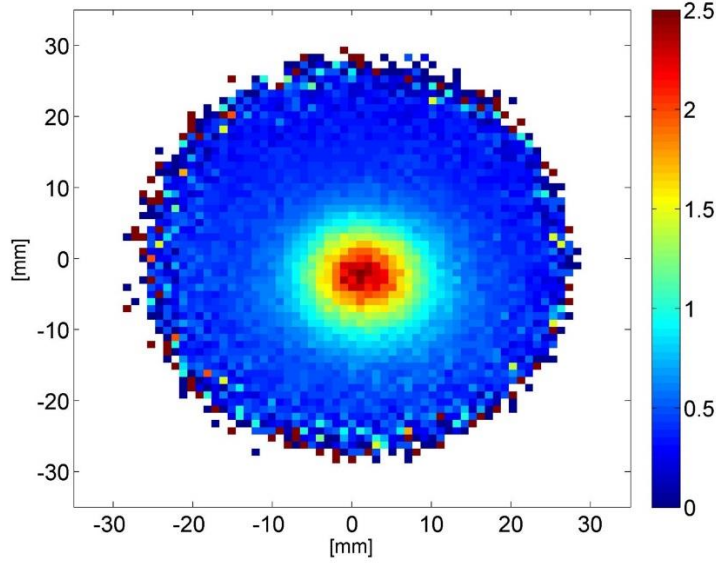


Figure 70: ^{60}Co gamma-ray image obtained by irradiating the LXe/GPM detector with a collimated-beam ($\sim 7\text{mm}$ diameter at the converter level). The image shows the ratio of the beam-to-flat irradiation (un-weighted COG-histogram-ratio image), as calculated according to Equation 19. GPM operating conditions: $\text{Ne}/5\%\text{CH}_4$; $p=356\text{Torr}$; $T=211\text{K}$. Charge threshold=1fC; Pads threshold=10 pads; gain= 4×10^4 .

The PSF profiles were determined through the center of the image (Figure 70), in X and Y axes. The PSF distributions are shown in Figure 71, with Lorentz function fits, for charge threshold of 1 fC and pads threshold of 10 pads. Table 12 compares the measured (weighted and un-weighted COG) and simulated (see 5.3.2) spatial-resolutions. The uncertainty on the measured spatial-resolution values was estimated as $\sim 2\text{mm}$ by the Lorentz function fit.

The PSF values, calculated with the un-weighted COG, are better than those calculated with the weighted COG; the measured spatial resolution was $12\pm 2\text{ mm}$ (FWHM) at a counting efficiency of 95.8% of the converted events (i.e. compared to pad threshold =0), in good agreement to the simulated values. While the PSF value did not improve significantly with increasing pad threshold from 5 to 10, increasing the latter above 5 resulted in considerable loss of efficiency (Table 12).

The rather large PSF value of $12\pm 2\text{ mm}$ (FWHM) determined in the present conditions for both, edge-object and collimated-beam measurements with ^{60}Co gamma-rays, is due to both the source dimensions and scattering within the detector volume. The good agreement between the measured and simulated spatial resolution values indicates that all experimental factors have been accounted for in simulations. Simulation performed for this detector prototype, with the same set of tools, for an infinitely thin pencil

gamma beam, provided *expected* ultimate resolutions of 6, 5, 4 and 5 mm (FWHM) for the respective gamma energies of 1.1, 1.3, 4.4 and 15.1 MeV (see section 5.3.2).

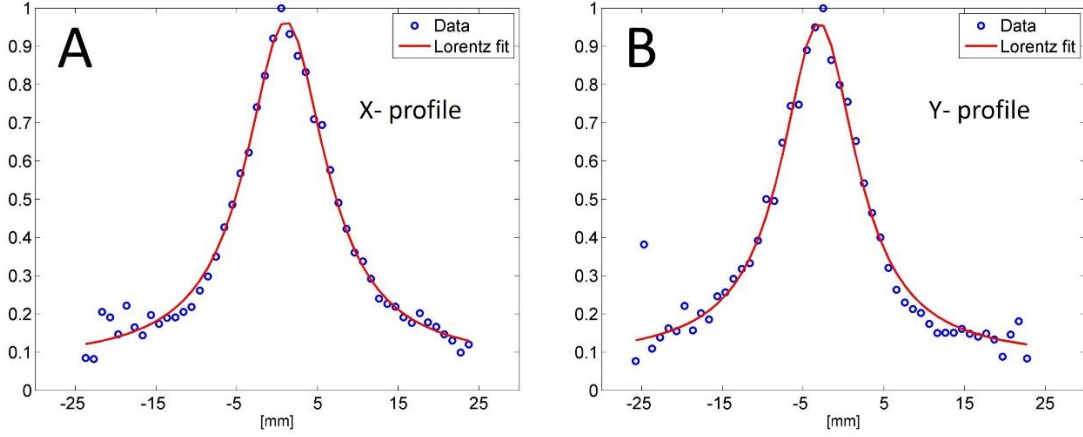


Figure 71: X and Y profiles through the center of the histogram of Figure 70, with fit to a Lorentz function. ^{60}Co ; GPM: Ne/5%CH₄; $p=356\text{Torr}$ (20 sccm flow); $T=211\text{K}$. Charge threshold=1fC; Pads threshold=10 pads.

Table 12: The PSF values, calculated from the X and Y profiles of the collimated ^{60}Co gamma beam, with weighted and un-weighted COG. The right-most column lists the PSF values calculated from the simulations (see section 1). The uncertainty on the PSF values is $\sim 2\text{mm}$.

Pad threshold	% of total counts	PSF (FWHM) [mm]				
		Weighted COG		Un – weighted COG		Simulations
		X profile	Y profile	X profile	Y profile	
5	95.8	16	13	12	12	10
10	63.1	16	13	12	11	10
20	14.4	14	13	11	11	9

6.4 Measurements in mixed neutron & gamma field

6.4.1 Time-of-flight measurements

TOF measurements were carried out in an attempt to separate the gamma-rays and fast neutrons emitted from the AmBe source; the setup description is provided in section 4.7.1 above. While the time resolution of the reference LaBr scintillator (gamma detector) is of the order of 1 ns (FWHM), that of the GPM depends on THGEM geometry and on the number of PEs per pulse (signal-to-noise; function of the THGEM bias). Typical values measured in the past for a double THGEM operating in Ar/CH₄ (95:5) were: 23 ns, 9.5 ns, 2 ns and 1 ns (FWHM) for 1, 25, 100 and 1000 photoelectrons, respectively [104, 105, 106]. The improved time-resolution with the

number of PE results from measuring the "first-arriving PE" (among those photo-produced at different locations on the photocathode's surface or arriving at different times due to diffusion) and from improved signal-to-noise ratio [104, 105, 106]. Further resolution deterioration occurs, in events with small number of PEs, due to the statistical pulse-height distribution of single ionization-electron pulses, affecting the trigger electronics.

According to simulations, the average number of scintillation-induced PEs by 1.2MeV gamma, 4.4MeV gamma and AmBe neutrons, are about 30, 100 and 30, respectively (see Table 7 and Table 8). These PEs are distributed throughout the THGEM's area so that each PE would reach a single hole in this electrode.

TOF spectra, resulting of 511keV and 1274keV gamma-rays (used here for calibration purposes), as measured with the GPM and the LaBr detector, are shown in Figure 72A. The blue graph, in Figure 72A, was measured while the CFD discrimination level of both, GPM and LaBr detectors, were set to enable measuring the 511keV and 1274keV. The green graph was measured while GPM's CFD discrimination level was set to cut the 511keV events.

Time resolutions of 20 ns and 30 ns (FWHM) were measured for scintillation light from 1274 keV and 511 keV gamma-rays, respectively. The expected numbers of PEs are ~30 and ~20 PE, respectively, extrapolating data from Table 7. These time resolution values are worse than expected (~8 and ~10 ns FWHM, respectively) as based on the number of created PEs.

For non-relativistic neutrons, the flight time is given by the following relation:

Equation 20

$$TOF[ns] = \frac{72.3 \cdot d[m]}{\sqrt{E[MeV]}}$$

Where TOF is the flight time in ns, d is the distance in meters and E is the neutrons energy in MeV.

TOF spectrum, of AmBe 4.4MeV gamma and neutrons, as measured with the GPM and the LaBr detector, is shown in Figure 72B. The neutrons' TOF at a flight distance of 83 cm, ranges from ~20 ns to ~80 ns, compatible with the AmBe-source

neutrons energies of 11MeV to 0.75MeV, respectively (according to Equation 20). Although the statistics is quite poor we estimate the time resolution of the 4.43 MeV gamma-ray peak to be about 10 ns (FWHM).

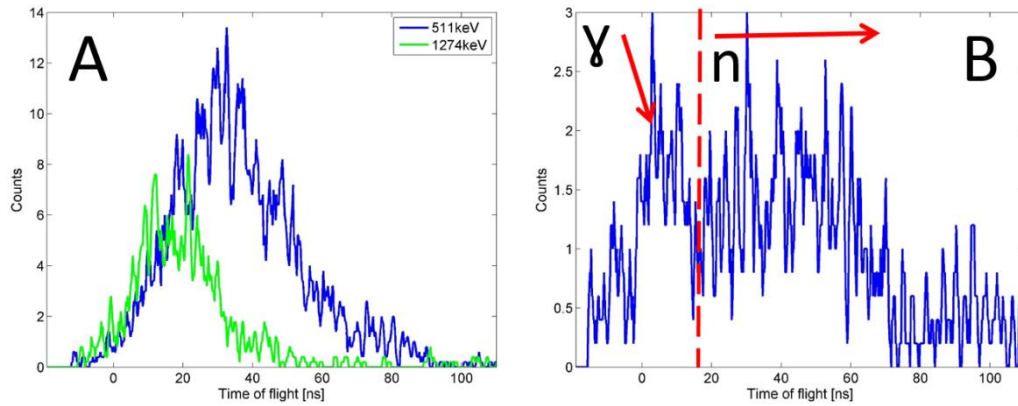


Figure 72: TOF spectra, of 511 keV and 1274 keV gamma-rays (A) and AmBe 4.4 MeV gamma and neutrons (B), as measured with the GPM and the LaBr detector. Flight path: 83 cm; GPM operating conditions: Ne/5%CH₄; p=356 torr (flow of 3 sccm); T=212 K; gain=7.6×10⁴.

The time resolution obtained in these measurements is significantly poorer than that quoted in the literature. The reasons for that could be that the actual PDE was lower than the assumed 10% and our cascaded-THGEM geometry is not optimal for reaching good timing. In addition, our specific THGEM had occasional-sparks history, which probably caused its "aging" and constrained operation at relatively low biases ($\Delta V_1=450V$ instead of $\Delta V_1=700V$) in this set of measurements - hence poorer signal-to-noise conditions and somewhat lower overall PE extraction efficiency from the photocathode (58% instead of 63% [45]).

As a result of the present experimental conditions, the TOF resolution did not permit separating neutrons from gamma; thus the following imaging experiments have been carried out in the mixed neutron and gamma field.

6.4.2 Edge imaging with mixed neutron & gamma field

The mixed-field irradiation setup with fast-neutrons and 4.4MeV gamma-rays, and the procedures involved, are described above (section 4.7.2).

A typical spectrum recorded with the LXe/GPM detector is shown in Figure 73; the spectrum has an exponential shape with a long tail toward higher charge values, as expected from the simulations (see Figure 46C). This is due to inelastic neutron

collisions or neutron capture reactions, where the resulting gamma-rays can add their energy to the Xe recoil one [83]. Furthermore, the introduction of hydrogen atoms inside LXe (structure material of the Tefzel capillaries) may extend the neutron spectrum due to the contribution of knock-on protons, which may receive large fraction of neutron energy in a single collision [83].

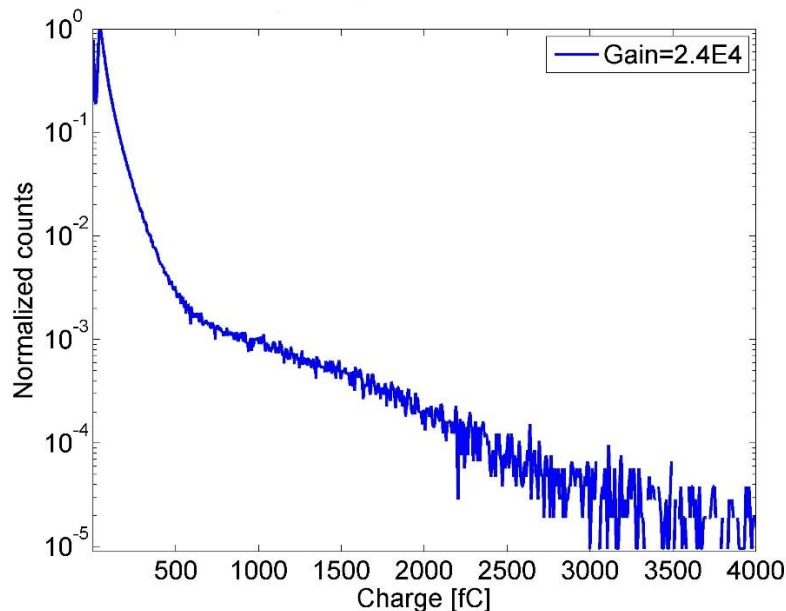


Figure 73: Mixed neutron and gamma-ray interactions in the LXe converter: spectrum of the total UV-photon induced charge in all GPM pads, calculated offline event-by-event. GMP: Ne/5%CH₄; $p=356$ torr (flow of 20 sccm); $T=212K$; $gain=2.4 \times 10^4$.

A typical scintillation-light distribution on the GPM pads, of a single event, is shown in Figure 18F. For each event, the un-weighted center of gravity was calculated according to Equation 15, for all events. Similar to the ⁶⁰Co gamma imaging, two measurements were done; one with the Pb-object covering half of the detector and another without object (flat image). The charge threshold in both measurements was set to 1fC and the pads threshold was set to 5 pads. The ratio image was calculated according to Equation 19, and is shown in Figure 74A. The color map indicates the transmission of the incident radiation, relative to flat image. The average profile of the edge, the ESF, is shown in Figure 74B along with a fit to a logistic function (Equation 18). One can clearly distinguish the covered area of the detector. The theoretical and simulated transmission of neutrons and gamma (of AmBe) through 12 mm thick Pb is 70%. In practice, the measured transmission was 82%, probably due to scattering from the concrete floor and walls, which was not taken into account in the simulations.

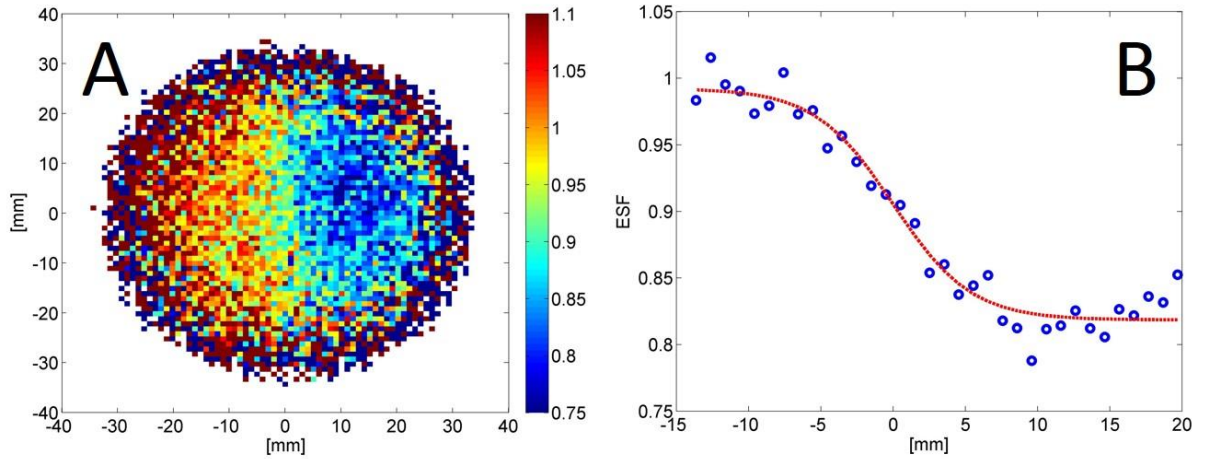


Figure 74: Lead object imaging with a mixed field of neutrons and gammas emitted from the AmBe source. A- Ratio of the object to flat images, calculated according to Equation 15. The color map indicates the transmission of the incidence radiation, relative to a flat image. B- ESF, profile and fit to a logistic function (Equation 19). GPM operating conditions: Ne/5%CH₄; p=356 torr (flow of 20 sccm); T=212K; gain=2.4×10⁴.

The PSF distributions shown in Figure 75 were obtained by differentiating the logistic function fitted to the ESF one (of Figure 74B), for 5, 10 and 20 pads thresholds. Table 11 summarizes the measured and simulated position-resolution values. The estimated error on the measured position-resolution values is ~2mm by the logistic function fit (Equation 19).

Position resolution of $\sim 10 \pm 2$ mm (FWHM) was measured for the mixed neutrons and gamma-rays (with pad threshold of 5), at high detection efficiency (89%; counting efficiency of converted events); it is in good agreement with simulations results (for the present experimental conditions).

Note that, as for the gamma-imaging described above, the estimated resolution in the present experimental conditions, performed with the same set of simulation tools, for a pencil neutron-only beam, is 11-15 mm (FWHM) for neutron energies of 1-11 MeV (see section 5.3.3).

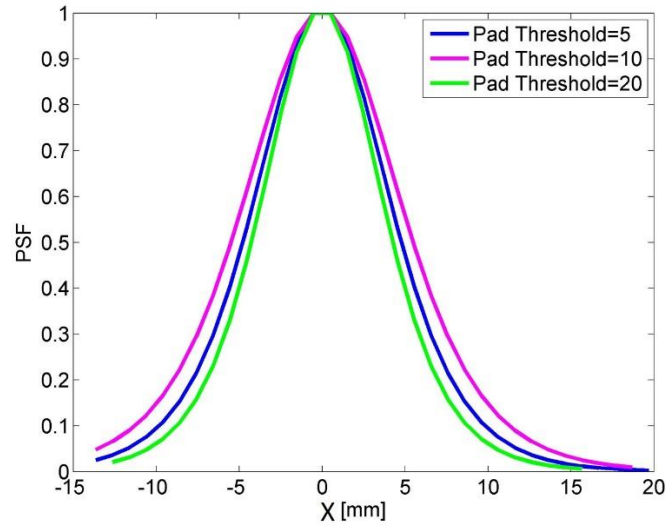


Figure 75: Mixed field of neutrons and gammas: PSF values for pads thresholds of 5, 10 and 20 pads, as calculated by the derivative of the ESF of the edge measurement (Figure 74B).

Table 13: Mixed field of neutrons and gammas: PSF values, calculated (with un-weighted COG) from simulation and experimental edge-irradiation results, for various pads thresholds. The % of total counts represents the detection efficiency of interacting events for a given pads threshold (counting efficiency of converted events). The estimated uncertainty on the PSF values is $\sim 2\text{mm}$.

Pad threshold	% of total counts	FWHM [mm]	
		Measurements (un-weighted COG)	Simulations
5	89.1	10	9
10	56.5	11	9
20	16.0	9	8

7 Summary and conclusions

This work focused on the feasibility study of a new robust, large-area and potentially cost-effective, detector concept for simultaneous imaging of gamma-rays and fast neutrons within the same detection medium – liquid xenon. The research was motivated by the need of effective instrumentation for homeland security applications; more precisely: the detection of concealed explosives (low-Z, with fast neutrons) and fissile materials (high-Z, with gamma-rays) by fast-neutron resonance radiography (FNRR) [9] and Dual-Discrete-Energy Gamma Radiography (DDEG) [7]. Both can be performed using mixed neutron/gamma beams (in the range of 1-20 MeV), provided by the $^{11}\text{B}(d,n\gamma)^{12}\text{C}$ reaction [7, 10]. Imaging of both radiation types with the same detector (usually performed by separate systems), can have practical advantages in terms of cost and throughput; it further enables the use of the data without the need for geometrical alignments and corrections. In the proposed combined DDEG & FNRR imaging, gamma-ray spectroscopy is performed by pulse-height analysis, while fast-neutron spectroscopy and neutron/gamma discrimination is done by a time-of-flight (TOF). The detector concept comprises an efficient, large-area, fast liquid-xenon (LXe) converter-scintillator contained within Tefzel capillaries, coupled to a UV-sensitive gaseous imaging photomultiplier (GPM); the latter incorporates a UV-sensitive CsI photocathode deposited on the top surface of a cascaded Thick Gas Electron Multiplier (THGEM).

In the experimental part of this study, we focused on the development of a small-area (100 mm in diameter) detector, its electronic readout, operation conditions and performances at RT and under cryogenic conditions. Its imaging performances were investigated with a ^{60}Co gamma source (energies of 1.17 and 1.33 MeV) and an AmBe source (mixed radiation field of 0-11 MeV neutrons and 4.4 MeV gamma). The detector's performances for the higher relevant gamma energies (15.1 and 4.4 MeV) foreseen for radiography, were estimated; measurements with these higher gamma energies will be performed at an accelerator outside the scope of this Ph.D. work.

The experimental activity was accompanied by a broad systematic computer-simulation study, including all steps: from radiation conversion in different types (plain liquid and capillaries) of LXe converters, through scintillation in the liquid, to signal

recording with the GPM. The simulations have predicted the efficiency and imaging properties of gamma and neutrons in the relevant energy ranges, in a large-area (580×580×50 mm) detector [83, 92] and in the smaller experimental prototype investigated over this study.

The simulation results of the large-area detector-response indicated that LXe-filled Tefzel capillaries can be considered as an optimal converter in terms of gamma and neutrons spatial resolutions (2-4 mm and ~2mm (FWHM), respectively) in the 2-15 MeV energy range, with respective detection efficiencies of 35% and 20%.

Following these results, a detector prototype was designed, incorporated and characterized in the Weizmann Institute Liquid Xenon cryostat system (WILiX). It consisted of LXe-filled Tefzel-capillaries radiation-converter of 133 mm diameter and 70 mm thickness, viewed by a UV-sensitive GPM and followed by a 2D readout electrode with 61 pads. The APV25-SRS electronics was adjusted for this application for reading analog charge signals induced on the 61 pads of the readout electrode, located at cryogenic temperature. Dedicated readout and analysis software packages were prepared for our experiments.

We characterized double- and triple-THGEM GPM detectors, with CsI photocathode on the first element, and studied their gain, long-term stability at RT and at cryogenic temperatures, under a wide range of counting rates and with different counting gases and pressures. Imaging properties at RT provided us with localization resolutions as function of number of photoelectrons per event (UV-photon flash). At room temperature, maximal gain values of $\sim 4 \cdot 10^5$ were measured with single photons at 756 torr and $\sim 4 \cdot 10^6$ at 552 torr. At cryogenic temperatures, a maximal gain of $\sim 6 \cdot 10^5$ was measured at 397 torr. These values assure high single-photon detection efficiency with the present low-noise APV25 front-end chips and are well sufficient for gamma and neutron imaging measurements. Stable operation at cryogenic temperatures, with high single-photon detection efficiency, was also demonstrated in the presence of highly ionizing background, inducing thousands of photoelectrons flashes [45, 107].

The imaging experiments with gamma (^{60}Co) and a gamma/neutron mixed radiation field (AmBe) were performed with the LXe/capillaries converter and a triple-THGEM GPM detector. The detector geometry was not optimal in sense of the distance between the LXe converter and the photocathode, which was 32 mm.

Experiments with gamma-rays were carried out with both: Pb-edge imaging and irradiating the detector with a collimated beam. The PSF value of the detector, obtained by differentiating the average profile of the edge, yielded a spatial resolution of 12 ± 2 mm (FWHM) for the ^{60}Co gamma-rays; it is in very good agreement with our simulated value in the present experimental geometry (see Table 11).

The experiments performed with the collimated (7mm in diameter) gamma beam, yielded the same resolution, also in rather good agreement to the simulated value (10 mm FWHM) (see Table 12) for the present experimental geometry.

The good agreement between the measured and simulated spatial resolution values, validates the effectiveness of the simulation tools. Therefore the latter were used to simulate the “ultimate” resolution in preferable detector geometry, in which the photocathode is closer to the LXe converter (distance of 13 mm), in response to an infinitely thin pencil gamma beam. In such configuration the estimated resolutions were 2-4 mm FWHM for all relevant (to this study) gamma energies (1.17, 1.33, 4.4 and 15.1 MeV) (see Figure 49D).

Experimental constraints (geometrical limitations at the laboratory, like short flight path, insufficient time resolution and the low activity of the available AmBe source), did not permit performing "neutron-only" imaging measurements. For that reason, Pb-edge object imaging was performed with the mixed gamma/neutron radiation field. These experiments yielded localization resolutions of $\sim 10\pm 2$ mm (FWHM) - in good agreement with the simulation results, for the present experimental conditions. The estimated resolution obtained with the same set of simulation tools, for a pencil neutron beam and preferable detector geometry (LXe converter- photocathode distance of 13 mm) is ~ 2 mm (FWHM) for neutron energies of 1-11 MeV, respectively (Figure 55C). TOF spectra, of AmBe 4.4 MeV gamma and neutrons, as measured with the LXe detector at the short available flight-path (83 cm), showed a potential for separation between gamma-rays and neutrons over larger distances.

As mentioned in the introduction the primary goal of this work was to develop a detector for detection of small quantities of SNM and explosives. A 500 g cube of HEU will have dimensions of about $3\times 3\times 3$ cm³. A 200 g of explosive material, such as TNT in a shape of a cube will have dimensions of about $6\times 6\times 6$ cm³. If the object is

positioned in midway between the radiation source and the detector, the image will be magnified by a factor of 2. Thus the shade created by the threat object is rather large (6x6 cm) and a position resolution of few millimeters obtained here appears to be satisfactory for the above application.

Gamma energy spectroscopy will be performed through pulse-height analysis of the GPM signals. In measurements of 1.17 and 1.33MeV gamma-rays in the present detector configuration, no photo-peak was seen due to the poor light collection and the avalanche process in the GPM (exponential behavior for few PEs; (see Figure 66 (measurement) and Figure 45C (simulation)). With the $^{11}\text{B}(d,n\gamma)^{12}\text{C}$ reaction foreseen for DDEGR, with two well-separated 4.4 MeV and 15.1 MeV gamma lines, the discrimination between the two will be easier, e.g. done by setting a lower-level threshold to measure only the 15.1 MeV gamma-rays (see simulation results in Figure 45C). The estimated contamination of the 4.4 MeV spectrum by 15.1 MeV gamma (~38%), if not corrected for, will affect the high-Z material differentiation accuracy.

In FNRR the fast-neutron spectroscopy and neutron/gamma discrimination are provided by TOF. E.g. an energy resolution of ~500 keV at neutron energy of 8 MeV is required for resolving neutron resonances of carbon in FNRR. For a 6 m long TOF facility, this energy resolution is equivalent to a time resolution of ~5 ns.

GPM scintillation signals were recorded with a time resolution of 2.8 ns (FWHM) for α particles [45] and 20 ns and 30 ns (FWHM) for 1274 keV and 511 keV gamma-rays, respectively (in this work). The superior time-resolution with increasing number of PEs results from measuring pulses with the rise-time originating from the "first-arriving PEs" (among those photo-produced at different locations on the photocathode's surface or arriving at different times due to electron diffusion in gas) and from improved signal-to-noise ratio [104, 105, 106]. Further resolution deterioration occurs, in events with small number of PEs, due to the statistical pulse-height fluctuations of single-electron pulses, affecting the trigger electronics. Simulations (assuming photo detection efficiency, $\text{PDE}_{\text{GPM}}=10\%$) showed that the average number of PEs for 1-11 MeV neutrons is similar to that of PEs induced by 1.33MeV gamma-rays (about 30 PEs, see Table 7 and Table 8). Based on previous studies [104, 105, 106] the expected time resolution for 30 PE should be about ~9 ns FWHM (Double-THGEM with Ar/5%CH₄ 1 bar); while we measured 20 ns (FWHM) with the gamma source. Thus, the expected time resolution of our small-dimensions prototype for 1-11MeV neutrons is also ~20

ns (FWHM). The reasons for the poor time resolution could be due to a non-optimal cascaded-THGEM geometry and to gain limits due to accumulated ‘history’ of occasional discharges, that might have caused it "aging" and thus constrained operation at low biases ($\Delta V_1=450\text{V}$ instead of $\Delta V_1=700\text{V}$ for a “fresh” detector), worse signal-to-noise figure and somewhat lower overall PE extraction efficiency from CsI (58% instead of 63% [45], see also Figure 81B in appendix 8.2).

For an operational FNRR detector the time resolution must be improved. It would require higher detector gains, optimized detector parameters and higher QE value of the photocathode. The spread in PE collection time can be reduced by optimizing the hole-geometry for the CsI-coated electrode (e.g. denser pattern of smaller holes), without effecting the PE collection efficiency into the holes. Such geometries are available with GEM (Gas Electron Multiplier) electrodes [108]. The standard GEM geometry (0.07 mm holes with 0.14 mm pitch) was already successfully used for UV-photon detection in RICH devices [65, 109]. A cascaded-GEM GPM, operated in pure CF_4 , was demonstrated to have a single-PE time resolution of < 4 ns [110]. While this geometry has good timing capabilities, its PE collection efficiency into the holes requires high applied potentials on the CsI-coated GEM, but with a benefit of high PE extraction efficiency. Further optimization can be done by varying holes diameter and pitch values. For example, a GEM electrode with 0.15 mm diameter, single-conical, holes and 0.3 mm pitch was recently tested at WIS in a different project with promising results [111]. Further significant improvement can be achieved by increasing the CH_4 concentration in the gas mixture (e.g., to 20%, as was done in [45]), resulting in reduction of the electron transverse and longitudinal diffusion and an increase in the electron drift velocity [112]. The GPM can reach high gain values and operate in a stable, discharge-free way, by replacing the last THGEM element in the cascade by a discharge-damping Resistive Plate WELL [113, 114]. This is currently being investigated in our group.

The detector concept investigated in this work has the potential of offering a robust, cost-effective, large-area solution for a **combined** detection and imaging of fast-neutrons and gammas, with adequate spatial resolution and detection efficiency. Due to the lack of appropriate neutron and gamma beams, the experiments have been carried out so far only at the laboratory, with radioactive sources. Simulations indicate however, that the detector would fulfill the efficiency and resolution requirements of a

large-object screening system (e.g. efficiency >10% for neutrons and gamma and spatial resolution in the order of 5-10 mm FWHM). This would require further studies at the required DC and pulsed-neutron and gamma fields, with faster GPM detector configurations – that are out of this thesis-work scope. However, such studies have been foreseen and planned in the near future – to fully validate the concept for the proposed application.

Among leading competing imaging techniques, are for example the TRION (neutrons spectroscopy) [12] and TRECOR (gamma and neutrons spectroscopy) [13] systems which combine solid-scintillator screens and intensified CCD cameras. Compared to the proposed LXe detector, they possess better spatial resolutions (~1 mm FWHM) for neutrons and gamma-rays in the relevant energy range; their better time resolution (5.1 and 9.2 ns FWHM for TRECOR and TRION, respectively [13]) results in good energy resolution for neutrons (by TOF). However, these techniques require combination of the gamma and neutron images, which are measured separately in different detector media. Furthermore, the very high cost of large-area imagers of this type, required for an operational container screening system, could be exorbitant.

8 Appendices

8.1 Appendix A – Evaporation and characterization of CsI photocathode

8.1.1 CsI photocathode evaporation

The CsI photocathodes used in the GPM were vacuum-deposited at our laboratory (see setup in Figure 76) on one side of the THGEM electrodes by Joule effect. The THGEM electrode was cleaned beforehand with the standard procedure: 1) flushed with doubly-deionized water; 2) 30 minutes in an ultrasonic bath of iso-propyl alcohol; 3) drying for 1 hour at 60 °C under pure-nitrogen flow; 4) drying for 2 additional hours at 95 °C under pure nitrogen flow. The THGEM electrode is then attached within the vacuum-evaporation vessel to an aluminum heating plate for “annealing” before and after deposition; this was shown to enhance the QE of CsI photocathodes and enhance their stability at short exposures to air during their transfer and installation - from the evaporation chamber to the GPM [115] and [116]. The evaporation setup (Figure 76) comprised of an Hg(Ar) UV lamp, a monochromator and a monitoring calibrated photodiode for *in-situ* monitoring the relative QE value of the photocathode. A Meissner trap was recently installed improving the vacuum quality by approximately one order of magnitude.

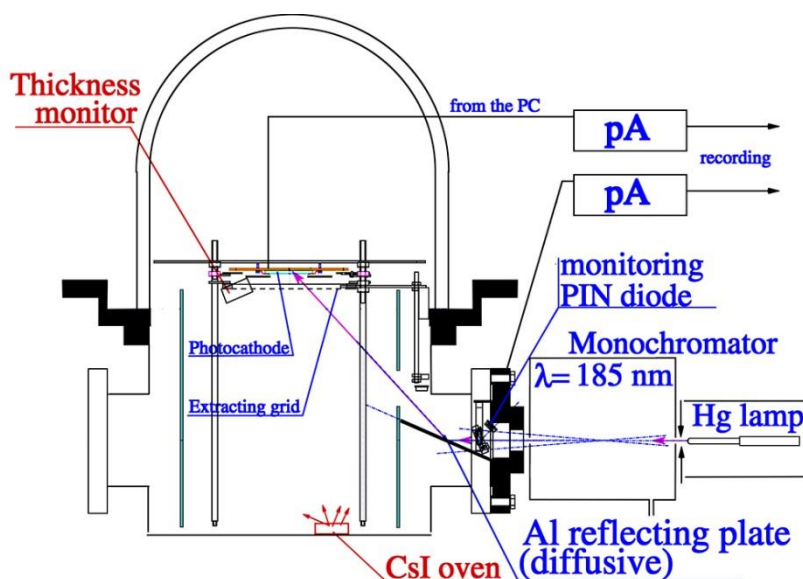


Figure 76: Scheme of the CsI evaporation setup by Joule effect.

Before loading the evaporation crucible with CsI, the chamber was evacuated down to $\sim 1 \times 10^{-7}$ torr and filled with argon. After opening the evaporation chamber, a sealed vial with CsI (purity of 99.999%) was opened at the chamber bottom; CsI powder was loaded on the tungsten crucible and the vial was removed. The evaporation chamber was evacuated down to $\sim 1 \times 10^{-7}$ torr; the CsI was melted by applying current ($\sim 100\text{A}$; $T_{\text{fusion}} = 621\text{ }^\circ\text{C}$) for removing impurities and moisture. Following this CsI pre-melting phase, the chamber was vented with argon and the THGEM electrode was assembled on the aluminum heater base, under argon atmosphere, facing the CsI crucible; after evacuation to $\sim 1 \times 10^{-7}$ torr, the CsI was gradually melted under a shutter; the latter was opened for the duration of the evaporation.

The thickness and deposition rate of the CsI photocathode was monitored by a Sycon Thickness/Rate Monitor STM-100 with a quartz oscillator; the rate (8 to 10 $\text{\AA}/\text{s}$) was manually controlled along the process by adjusting the applied current to the tungsten crucible; the process was stopped when reaching a thickness of $\sim 3000\text{ \AA}$. After deposition, the photocathode's photocurrent was monitored for 24 hours in vacuum.

To extract the photocathode in best-possible conditions, the evaporation chamber was enclosed in an airtight glove-bag and the system was vented and flushed with dry nitrogen. The CsI-coated THGEM electrode, on its aluminum heater base, was transferred (in the glove-bag) to a transport chamber and sealed under nitrogen; the latter was removed from the glove-bag and was either transferred to the nitrogen filled glove-box for installation on the GPM or coupled to a McPherson 302 vacuum monochromators (Figure 77) for a precision measurement of the photocathodes' absolute QE value. The installation process in the vacuum monochromator exposed the CsI to air for a few seconds.

8.1.2 Photocathode characterization

The *relative QE* of the photocathode was estimated, *in-situ*, by illuminating the photocathode with an Oriel Hg(Ar) calibration lamp; its 185 nm line was selected with an UV-monochromator (Oriel model 77250) flushed with pure nitrogen. The light intensity was monitored using a UV beam-splitter and a far-UV sensitive Hamamatsu (S1722-02) Si PIN photodiode. The quantum efficiency of the photocathode was estimated within $\pm 10\%$, by comparing the measured CsI photocurrent, normalized to

that of the photodiode, with previous measurements with other photocathodes of a known absolute QE (determined with the McPherson 302 vacuum monochromators). The *absolute QE* value of the photocathodes was established (with the McPherson monochromators; Figure 77) by comparing its photocurrent (per given wavelength) to that measured with a NIST-calibrated Ball Aerospace far-UV vacuum photodiode (s/n: 1-926). The photodiode (with CsI photocathode and MgF₂ window) was operated with +150 V bias; its absolute QE was provided within 6% error, between 1164 Å and 2000 Å. The monochromator optics provided a quasi-parallel beam, with a (selected by us) diameter of ~8 mm. A side monitoring-PMT permits normalizing the photocurrents to the lamp intensity (usually used only in high-precision measurements). The photocurrents were measured by Keithley 610C pico-amperimeters.

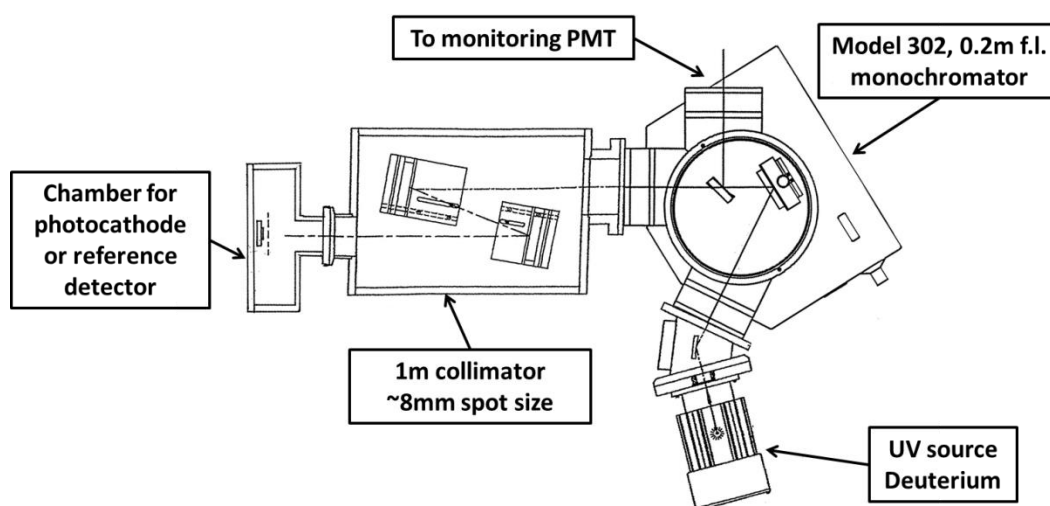


Figure 77: Simplified schematic of the CsI photocathode quantum efficiency measurement setup with the McPherson 302 monochromator.

The QE of a CsI photocathode for a given wavelength λ , $QE_{CsI}(\lambda)$, is determined according to Equation 21:

Equation 21

$$QE_{CsI}(\lambda) = QE_{Ball}(\lambda) * \frac{I_{CsI}(\lambda)}{I_{Ball}(\lambda)} * \frac{I_{MonitorBall}(\lambda)}{I_{MonitorCsI}(\lambda)}$$

Where $QE_{Ball}(\lambda)$ is the known absolute quantum efficiency of the Ball Aerospace photodiode, $I_{CsI}(\lambda)$ is the measured photocurrent of the CsI photocathode, $I_{Ball}(\lambda)$ is the current measured from the Ball Aerospace photodiode, $I_{MonitorBall}(\lambda)$ and $I_{MonitorCsI}(\lambda)$ are the currents from the monitoring PMT during measurements with the photodiode and

photocathode, respectively. Figure 78 shows the $QE_{Ball}(\lambda)$ graphs, as calibrated by NIST in 1993, and recently recalibrated in 2015. Note that the QE value decreased over the years only by $\sim 12\%$ at the relevant 175 nm wavelength.

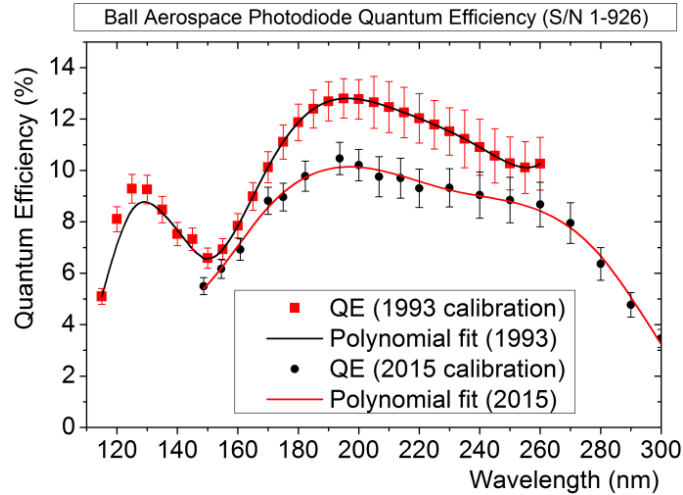


Figure 78: Quantum efficiency of the Ball Aerospace photodiode $QE_{Ball}(\lambda)$ from the original 1993 NIST calibration and from a recent 2015 calibration.

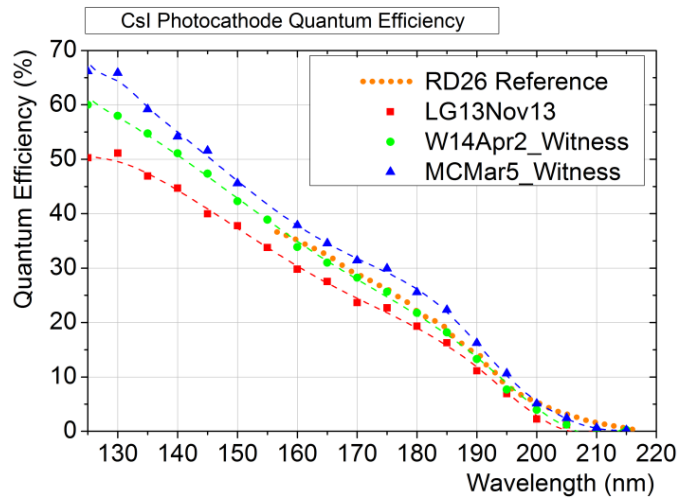


Figure 79: Measured absolute QE values in vacuum of several CsI photocathodes as evaporated on freshly cleaned THGEM gold-plated electrodes. Also represented is the CERN-RD-26 reference..

Figure 79 shows typical QE distributions in vacuum of CsI photocathodes we deposited on gold-plated THGEM electrodes. that the QE value at the Xe-emission wavelength of ~ 175 nm ranged from 24% to 30%. The measured QE values compare with the CERN-RD-26 Collaboration reference value, also shown in Figure 79. To remind, the photocathodes used for these measurements were only exposed for a few seconds to air during installation in the vacuum monochromator.

8.2 Appendix B – Estimation of the overall extraction efficiency

In this appendix we estimate the overall PE extraction efficiencies from CsI as a function of the electric field in Ne/CH₄, Ar/CH₄ and Ne/CF₄ for few gold-plated THGEM geometries (**A**- pitch $a = 0.8$ mm; hole diameter $d = 0.4$ mm; thickness of the substrate $t = 0.4$ mm; rim around the hole $h = 10$ μm ; thickness of the gold layer $\text{Au} = 33$ μm , **B**- $a=0.8$ mm; $d=0.4$ mm; $t=0.4$ mm; $h=50$ μm ; $\text{Au}=64$ μm , **C**- $a=0.7$ mm; $d=0.3$ mm; $t=0.4$ mm; $h=10$ μm ; $\text{Au}=33$ μm , **D**- $a=0.7$ mm; $d=0.3$ mm; $t=0.4$ mm; $h=50$ μm ; $\text{Au}=64$ μm).

The electric field on the photocathode surface, as function of the voltage applied across the THGEM (ΔV_{THGEM}), was calculated using Maxwell software [117] in resolution of $2\mu\text{m}$ (see for example Figure 80). The extraction efficiency, in each point on the photocathode surface, was estimated using the calculated electric field and the data from Figure 9. Extraction efficiencies for electric field values larger than the maximum electric field in Figure 9, were evaluated by extrapolation (taking 1 as the upper limit for extraction efficiency). The overall extraction efficiency was defined as the average of extraction efficiencies over all points across the photocathode surface.

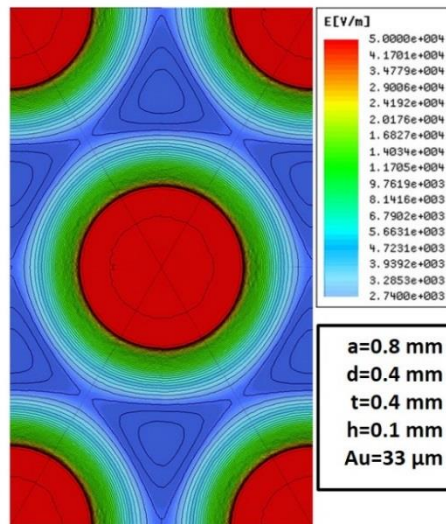


Figure 80: Electric field intensity map on the THGEM surface, having the parameters: $a=0.8$ mm, $d=0.4$ mm, $t=0.4$ mm, $h=0.1$ μm and cladding thickness of 33 μm (see text). Here, the field across the surface varies between 0.03 - 0.5 kV/cm.

The overall extraction efficiencies as a function of ΔV_{THGEM} for Ne/CH₄, Ar/CH₄ and Ne/CF₄ for four gold plated-THGEM geometries are shown in Figure 81. For geometry A, extraction efficiencies above 0.7 (and below 0.8) were estimated for

Ne/CH₄ with CH₄ concentration >50% or for Ne/CF₄ with CF₄ concentration >10% and $\Delta V_{\text{THGEM}} > 400\text{V}$. For Ar/CH₄, extraction efficiencies of ~ 0.8 were estimated for $\Delta V_{\text{THGEM}} > 400\text{V}$.

Enlarging the rim and the Au thickness increase the extraction efficiency by a few percent, for certain voltages (compare Figure 81 A to B and C to D). Reducing the pitch decreases the extraction efficiency by a few percent, for certain voltage (compare Figure 81 A to C and B to D).

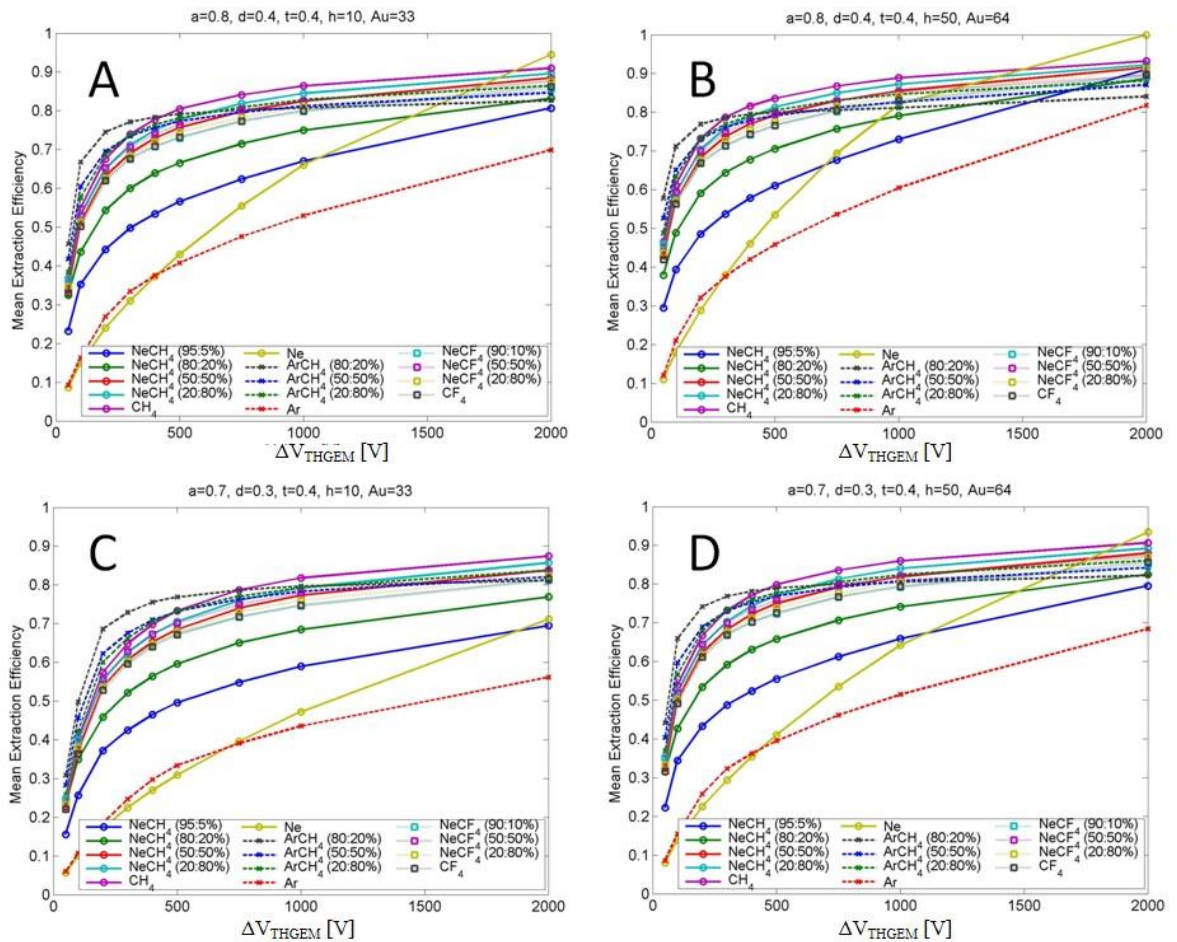


Figure 81: The overall extraction efficiencies as a function of ΔV_{THGEM} for Ne/CH₄, Ar/CH₄ and Ne/CF₄ for four gold coated-THGEM geometries; Figure A- $a=0.8\text{ mm}$; $d=0.4\text{ mm}$; $t=0.4\text{ mm}$; $h=10\text{ }\mu\text{m}$; $\text{Au}=33\text{ }\mu\text{m}$; Figure B- $a=0.8\text{ mm}$; $d=0.4\text{ mm}$; $t=0.4\text{ mm}$; $h=50\text{ }\mu\text{m}$; $\text{Au}=64\text{ }\mu\text{m}$; Figure C- $a=0.7\text{ mm}$; $d=0.3\text{ mm}$; $t=0.4\text{ mm}$; $h=10\text{ }\mu\text{m}$; $\text{Au}=33\text{ }\mu\text{m}$; and figure D- $a=0.7\text{ mm}$; $d=0.3\text{ mm}$; $t=0.4\text{ mm}$; $h=50\text{ }\mu\text{m}$; $\text{Au}=64\text{ }\mu\text{m}$.

As mentioned above (section 4.2), the experiments were performed with THGEM electrodes of $a = 0.8\text{ mm}$, $t=0.4\text{ mm}$, $d = 0.4\text{ mm}$, $h = 50\text{ }\mu\text{m}$ and Cu layer thickness of $64\text{ }\mu\text{m}$. The applied ΔV_1 value were between 450 and 500 V. For these parameters the overall PE extraction efficiency from CsI is $\sim 58\%$ (see Figure 81).

8.3 Appendix C - Large electrode preparation and testing

8.3.1 Leak current measurement

In order to get some preliminary indication about the THGEM-electrode quality, a setup was used that permitted the biasing one face and connecting the other to a grounded, discharge-protected Pico ammeter. The THGEM electrode was installed in a closed vessel, constantly flushed with pure nitrogen. Its leakage current was measured versus the applied voltage, up to the discharge limit.

The best electrodes were used in our GPM detectors, while the others, with the higher leakage currents, were reprocessed by standard cleaning, as described above (see section 8.1.1). The criteria for a “good electrode”: for applied voltage up to 1.5 kV the leakage current measured after 10 minutes of stabilization, should be < 0.5 nA, with no significant fluctuations.

8.3.2 Optical discharge localization

Discharges can occur sporadically over the area - due to highly-ionizing events, or in well-localized holes – due to defects. Each of the THGEM electrodes was scanned for localized discharge "hot-spots" by taking sequence pictures under high voltage in pure helium. The electrodes were thoroughly flushed with dry N₂ gas and installed in a chamber with a large transparent window, viewed with a CCD camera. The chamber was flushed with pure helium gas – which decreased the THGEM discharge voltage to ~ 500 V. A large number ($\sim 10^3$) of individual discharge events were recorded for each electrode with the FLI CCD camera (512x512pixels) set for an exposure time of 0.2 seconds, equipped with a Nikon Nikkor f/1.6 50 mm lens. The camera was cooled by an internal Peltier element and was set for continuous frame acquisitions, from which only the frames showing discharges were selected. The frames were processed in a MatLab code and the position of each discharge event was recorded. Figure 82A depicts the illuminated THGEM electrode; a typical recorded single discharge is shown in Figure 82B, as localized by the MatLab code. The position and occurrence frequency of each discharge is plotted, providing the indication of a damaged hole or area.

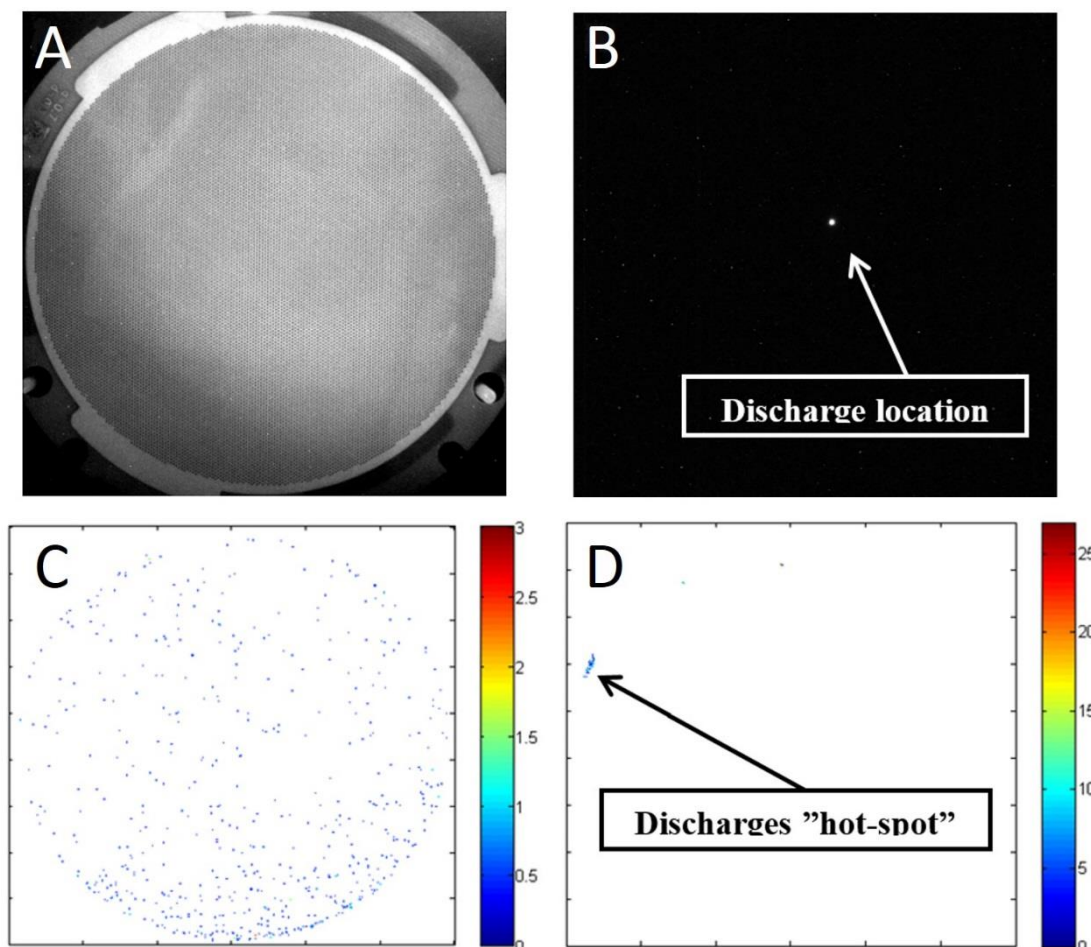


Figure 82: The optical inspection of THGEM electrodes: A) Image of a THGEM acquired by the FLI CCD camera. B) A typical raw image of a single discharge. C) Map of discharges recorded optically on a THGEM electrode, after MatLab processing. D) A detected “hot area” (probably a defect at the electrode edge) of repeated discharges. Scales on right indicates the numbers of overlapping discharge events.

Figure 82C and Figure 82D show the spatial distribution of discharges for a “good” electrode, and for a “bad” one, respectively. In the good electrode the recorded sporadic discharges are well distributed throughout all the area; the circular shape of the electrode can clearly be inferred; here only three discharges occurred in the same hole during the acquiring time, identified by the color bar on the right. In the “bad” electrode most of the recorded discharges occurred in a much localized area at the electrode’s edge; more than 25 discharges occurred in one hole, and others in neighboring ones. In this particular case, upon close inspection of the problematic area, it was observed that at some point in time the electrode was handled without gloves as witnessed by a fingerprint. Cleaning the electrode with the procedure described above (see section 8.1.1) improved its condition dramatically.

8.4 Appendix D - α source imaging

As a preparatory stage, before gamma and neutron imaging, we performed imaging measurements of an ^{241}Am α -source, immersed within LXe (see Figure 83). The 5.5MeV α -particles stop in LXe within 45 μm [118], emitting a large number ($\sim 3\text{E}5$) of scintillation UV-photons over 4π [22]. Therefore, these measurements were expected providing the ultimate localization resolution of the GPM. The active geometrical shape of the open source, deposited on a stainless steel disc, has the dimensions of $\sim 7\text{ mm} \times \sim 5\text{ mm}$ (Figure 83A). The image of the 5.5 MeV alpha particles emitted into the liquid was measured by the GPM and compared to the source autoradiography, when placed on a digital Fuji Plate (of few-microns spatial resolution).

The experimental setup (Figure 83B) shows the α -source, located inside LXe volume (without capillaries), viewed by the GPM through a quartz window ($\phi=36\text{mm}$). A Pyrex-made cup, surrounding the LXe volume, was added to absorb the UV-scintillation photons directed to the walls to prevent image deformation due to UV reflections from the walls. Some scattered UV photons (e.g. from the window) reach a PMT placed underneath the source (blind to the direct scintillation photons) – providing a trigger to the SRS electronics.

The GPM was operated at gain of 1.3×10^4 with 502 torr of Ne/5%CH₄ at a flow of 20 sccm and at 222 K.

In this setup, the GPM viewed the source-emitted scintillation photons over a solid angle of 0.4156 Sr, the window transmission in liquid was 0.95, the GPM mesh transmission was 0.84, the photocathode extraction efficiency was ~ 0.55 (for $dV_1=500\text{V}$), the CsI coverage of the THGEM electrode was 0.77 and the photocathode quantum efficiency was measured as $\text{QE} \approx 12\%$.

The extracted PEs were multiplied by the THGEMs cascade, inducing charge signals on a large number of pads (see typical single event in Figure 18D). A typical spectrum of the total charge recorded in all pads, event by event, and distribution of number of pads with charge above 0.96fC, are shown in Figure 84. In contrast to the gamma charge spectrum (see Figure 66), the α one has a peaked distribution, since the α -particles deposit all of their energy within the LXe, yielding $\sim 410\text{PEs/event}$ ($N_{\text{PE}} = 3.06\text{E}5 * (0.4156/4\pi) * 0.95 * 0.84 * 0.55 * 0.77 * 0.12$) in the GPM.

When the resolution is dictated only by the statistics of the avalanche process (with exponential distribution for single PEs), the relation $\sigma/\mu = \sqrt{2/N_{PE}}$ holds, where σ and μ are the standard deviation and mean of the peak and N_{PE} is the number of PE. Fitting a Gaussian, to the measured charge spectrum, resulted in $\sigma/\mu=13\%$, which is larger than 7% ($=\sqrt{2/410PE}$), indicates that there are more process affecting the resolution, e.g. light collection statistics.

The distribution of the number of pads with charge above $0.96fC$ shows that most events had at least 30 pads firing.

For each event, the center of gravity was calculated, according to Equation 15. Then, a 2D histogram of the COGs was plotted.

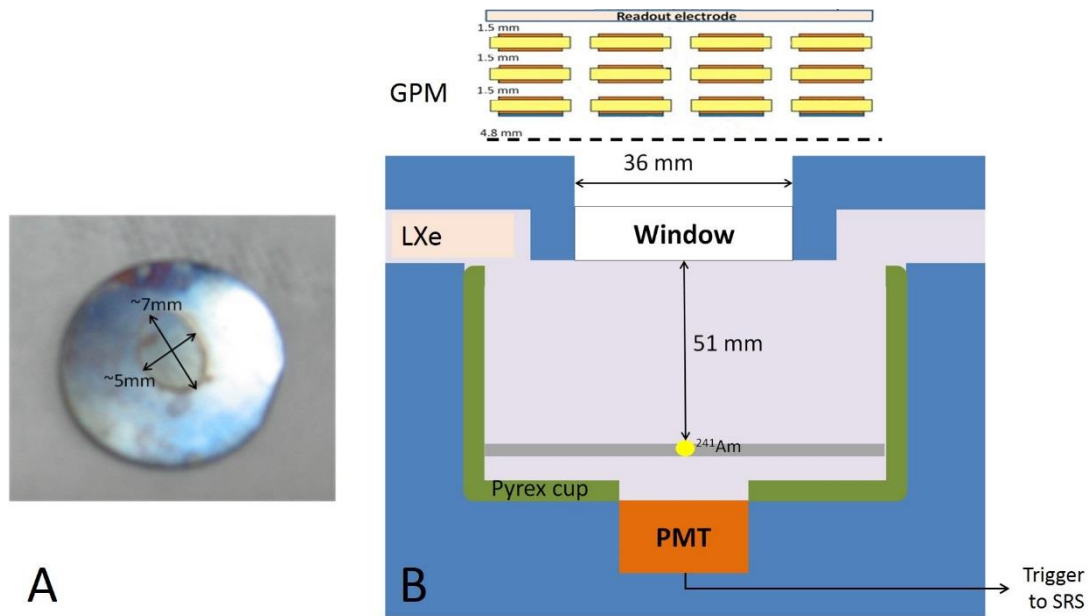


Figure 83: A- The open ($\sim 7\text{mm} \times \sim 5\text{mm}$) ^{241}Am α -source deposited on a metal disk. B- The experimental setup; the ^{241}Am α -source, immersed in LXe (without capillaries), viewed by the GPM through a UV-window (here $\phi=36\text{mm}$). A surrounding Pyrex cup absorbs the UV scintillation light directed to the walls to prevent UV reflections. Some scattered UV photons reach the PMT, placed within the LXe under the source, providing a trigger to the SRS electronics.

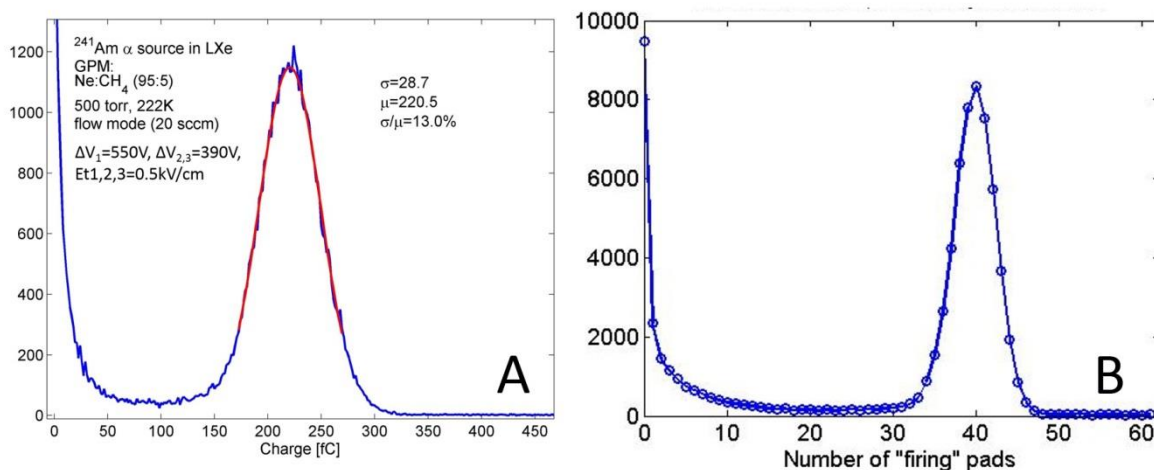


Figure 84: Spectrum of the total charge integrated from all pads, event by event (A) and a distribution of the number of pads with charge above 0.96fC (B), as measured with an ^{241}Am α -source located inside LXe (without capillaries). The red curve in figure A is a Gaussian fit to the data. (see text)

Figure 85 shows the active geometrical shape of the immersed ^{241}Am α -source as imaged by the GPM (A); (B) shows the source image in air, when in contact with the digital Fuji plate. The gray scale of the Fuji plate image is logarithmic. One can see that the active area is indeed elliptic with dimensions of 7.6mm X 5.5mm while most of the source activity is located on a thin contour ($\sim 0.7\text{mm}$ wide) defining its ellipsoidal shape.

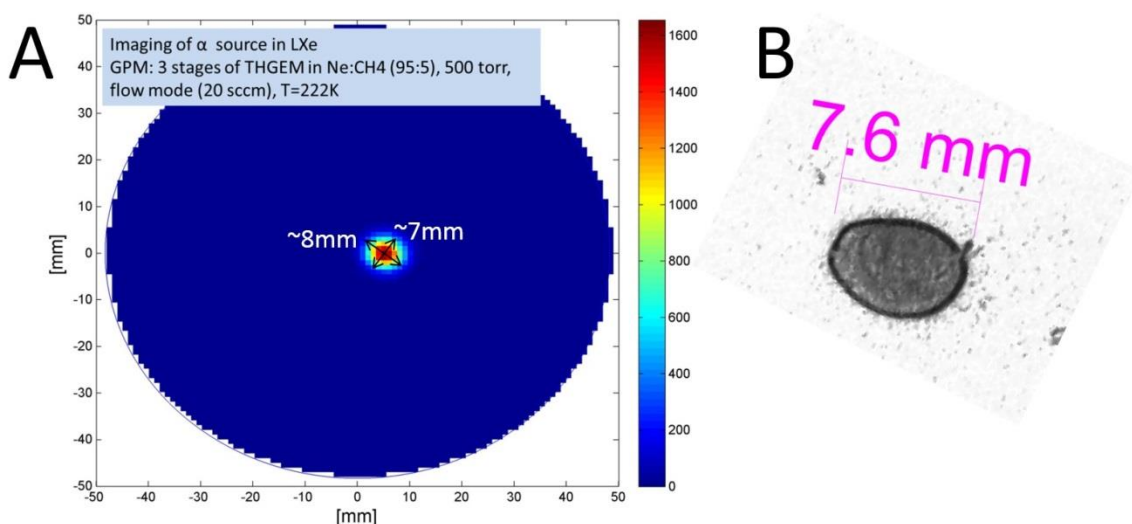


Figure 85: Image of the active geometrical shape of the ^{241}Am α -source. A- Measurement by the GPM of the α -source immersed within LXe. B- Measurement with the Fuji plate with the α -source placed on the plate, in air. In B the image is not converted to local activity and the gray scale is logarithmic. Notice the high activity at the source contour.

According to Figure 60, the GPM spatial resolution (at RT) of a point source emitting ~ 410 PEs/event is ~ 2 mm (FWHM). This resolution does not allow

differentiating the sub-millimetric active contour; however the size ($8 \text{ mm} \times 7 \text{ mm}$) and location of the α -source are well reproduced.

9 **Bibliography**

- [1] R.C. Runkle et al., "Photon and neutron interrogation techniques for chemical explosives detection in air cargo: A critical review", Nucl.Instr. Meth A603 (2009) 510.
- [2] R.C. Runkle et al., "Rattling nucleons: New developments in active interrogation of special nuclear material".Nucl.Instr. Meth A633 (2012) 75.
- [3] <http://www.rapiscansystems.com/en/products/cvi>
- [4] NUCTECH Company Ltd; Dual-Energy Container/Vehicle Inspection Technology, http://www.nuctech.com/indexa_en.jsp?urlbh=31&bh=138&sjlm=2&en=0.
- [5] Smiths Detection Group Limited, see e.g. HCVG and HCVS in "Container Screening" products, http://www.smithsdetection.com/eng/PB_container_screening.php
- [6] Varian Medical Systems, Inc., Security and Inspection, see e.g. Linatron-K9 Dual Energy Cargo screening solution. http://www.varian.com/media/security_and_inspection/products/pdf/DualEnergyProductBrief.pdf
- [7] M.B.Goldberg et al., "A dual-purpose ion-accelerator for nuclear-reaction-based explosives-and SNM detection in massive cargo", Proceedings of International Topical Meeting on Nuclear Research Applications and Utilization of Accelerators, 4-8 May 2009, Vienna, IAEA,Vienna, 2010, STI/PUB/1433, ISBN 978-92-0-150410-4, ISSN 1991-2374,<http://arxiv.org/abs/1001.3255>
- [8] Buffler A., "[Contraband detection with fast neutrons](#)", Rad. Phys. and Chem. 71(2004) pp. 853-861, and references therein
- [9] D. Vartsky et al., "Monte-Carlo simulations of time-resolved, optical readout detector for fast-neutron transmission spectroscopy", Proceedings of "International Workshop on Fast Neutron Detectors and Applications" PoS(FNDA2006) 064. http://pos.sissa.it/archive/conferences/025/084/FNDA2006_084.pdf
- [10] M.B. Goldberg, U.S. Pat.No. 7,381,962 (June 3, 2008 — prioritydate:Dec. 16, 2003).
- [11] V. Dangendorf et al., "[Detectors for energy-resolved fast-neutron imaging](#)", Nucl.Instr.Meth., A 535 (2004) 93-97.
- [12] Mor et al, "High spatial resolution fast-neutron imaging detectors for Pulsed Fast-Neutron Transmission Spectroscopy", 2009 JINST 4 P05016

- [13] M. Brandis et al. " Neutron measurements with Time Resolved Event Counting Optical Radiation (TRECOR) detector", 2012 JINST 7 C04003
- [14] Private communication with Michal Brandis. Measurements performed but not published yet.
- [15] P. B. Rose, A. S. Erickson, M. Mayer, J. Nattress, I. Jovanovic."Uncovering Special Nuclear Materials by Low-energy Nuclear Reaction Imaging".
nature scientific reports 6, Article number: 24388 (2016), doi:10.1038/srep24388
- [16] http://www2.dupont.com/Teflon_Industrial/en_US/assets/downloads/h96518.pdf
- [17] R. Chechik, A. Breskin. (2008). Advances in Gaseous Photomultipliers. Nuclear Instruments and Methods in Physics Research A(595), 116-127.
- [18] R. Chechik, A. Breskin, C. Shalem, D. Mormann. (2004, December). Thick GEM-like hole multipliers: Properties and possible applications. Nuclear Instruments and Methods in Physics Research Section A, 535(1 - 2), 303 - 308.
- [19] C. Shalem et al., "Advances in Thick GEM-like gaseous electron multipliers—Part I: atmospheric pressure operation ", Nucl. Instrum.Meth.A558, 475 (2006).
- [20] M. Cortesi et al.,"Investigations of a THGEM-based imaging detector ",2007 JINST2 P09002.
- [21] A. Breskin et al., "A concise review on THGEM detectors", Nucl.Instr.Meth.A598 (2009) 107.
- [22] E. Aprile and T. Doke, "Liquid xenon detectors for particle physics and astrophysics", Rev. Mod. Phys. 82, (2010) 2053-2097 [arXiv:0910.4956].
- [23] V. Chepel and Henrique Araújo. "Liquid noble gas detectors for low energy particle physics", 2013 JINST 8 R04001. arXiv:1207.2292.
- [24] E. Aprile, A. E. Bolotnikov, A. I. Bolozdynya and T. Doke, "Nobles Gas Detectors". WILEY-VCH Verlag GmbH & Co. KGaA, 2006
- [25] U. Asaf, I. T. Steinberger, "Photoconductivity and electron transport parameters in liquid and solid xenon," Physical Review B, vol. 10, no. 10, pp. 4464 - 4468, November 1974.
- [26] M. J. Berger, J. S. Coursey, M. A. Zucker, J. Chang. National Institute of Standards and Technology - ESTAR, PSTAR, and ASTAR. [Online].
<http://www.nist.gov/pml/data/star/index.cfm>
- [27] <http://physics.nist.gov/PhysRefData/Star/Text/ASTAR.html>
- [28] NIST XCOM: <http://physics.nist.gov/PhysRefData/Xcom/html/xcom1.html>

- [29] G. F. Knoll, "Radiation detection and measurements", Fourth edition 2010, John Wiley and sons, Inc.
- [30] P. Rinard, "Neutron Interaction with Matter," in *Passive Nondestructive Assay of Nuclear Materials*, N. Ensslin, H. Smith Jr. D. Reilly, Ed.: Nuclear Regulatory Commission, NUREG/CR-5550, 1991, ch. 12, p. 357.
- [31] ENDF nuclear data: <http://www.nndc.bnl.gov/exfor/endl00.jsp>
- [32] R. L. Platzman, "Total ionization in gases by high-energy particles: An appraisal of our understanding," *International Journal of Applied Radiation and Isotopes*, vol. 10, no. 2 - 3, pp. 116 - 127, 1961.
- [33] E. Shibamura, "Drift velocities of electrons, saturation characteristics of ionization and W-values for conversion electrons in liquid argon, liquid argon-gas mixtures and liquid xenon," *Nuclear Instruments and Methods in Physics Research Section A*, vol. 131, pp. 249 - 258, 1975.
- [34] T. Takahashi, S. Konno, T. Hamada, M. Miyajima, S. Kubota, A. Nakamoto, A. Hitachi, E. Shibamura, T. Doke, "Average energy expended per ion pair in liquid xenon," *Physical Review A*, vol. 12, no. 5, p. 1771, November 1975.
- [35] Joshua Jortner, Lothar Meyer, Stuart A. Rice, E. G. Wilson, "Localized Excitations in Condensed Ne, Ar, Kr and Xe," *Journal of Chemical Physics*, vol. 42, no. 12, p. 4250, 1964.
- [36] N. Schwentner, E-E Koch, J Jortner, *Electronic Excitations in Condensed Rare Gases.*: Springer-Verlag Berlin and Heidelberg GmbH & Co. K, 1985.
- [37] Kubota, S., M. Hishida, and J.Ruan, 1978, *J. Physics*, Vol.11, 2645
- [38] A. Hitachi, T. Takahashi, N. Funayama, K. Masuda, J. Kikuchi, T. Doke, "Effect of ionization density on the time dependence of luminescence from liquid argon and xenon," *Physical Review B*, vol. 27, p. 5279, May 1983.
- [39] M. Szydakis, N. Barry, K. Kazkaz, J. Mock, D. Stolp, M. Sweany, et al., NEST: a comprehensive model for scintillation yield in liquid xenon, *JINST* 6 (2011) P10002.
- [40] M. Szydakis, A. Fyhrie, D. Thorngren and M. Tripathi, "Enhancement of NEST Capabilities for Simulating Low-Energy Recoils in Liquid Xenon", 2013 *JINST* 8 C10003; e-Print: arXiv:1307.6601 [physics.ins-det and astro-ph.IM]
- [41] J. Lindhard, V. Nielsen, M. Scharff and P. V. Thomsen, Integral equations governing radiation effects, *Mat. Fys. Medd. Dan. Vid. Selsk.* 33 (1963) 1
- [42] J. Thomas and D. Imel, Recombination of electron-ion pairs in liquid argon and liquid xenon, *Phys. Rev. A* 36 (1987) 614.

- [43] A. Breskin, CsI UV photocathodes: History and mystery, Nucl. Instrum. Meth. A 371 (1996) 116.
- [44] F. Piuz, "CsI-photocathode and RICH detector", Nuclear Instruments and Methods in Physics Research Section A 371 (1996) 96-115
- [45] L. Arazi, A. E. C. Coimbra, E. Erdal, I. Israelashvili, M. L. Rappaport, S. Shchemelinin, D. Vartsky, J. M. F. dos Santos, and A. Breskin. "First results of a large-area cryogenic gaseous photomultiplier coupled to a dual-phase liquid xenon TPC". 2015 JINST 10 P10020. <http://dx.doi.org/10.1088/1748-0221/10/10/P10020>.
- [46] R. T. Poole, J. G. Jenkin, J. Liesegang, R. C. G. Leckey. (1975, June). Electronic band structure of the alkali halides. I: Experimental parameters. Physical Review B, 11(12), 5179 - 5189.
- [47] A. Buzulutskov, A. Breskin, R. Chechik. (1997). Photoemission through thin dielectric coating films. Journal of Applied Physics , 81(1), 466.
- [48] R. Triloki, Nikita Gupta, Nabeel F.A. Jammal, B.K. Singh. (2014). Photoemission and optical constant measurements of a Cesium Iodide thin film photocathode. Nuclear Instruments and Methods in Physics Research Section A, 787, 161 - 165.
- [49] W. E. Spicer. (1958, October). Photoemissive, Photoconductive, and Optical Absorption Studies of Alkali-Antimony Compounds. Physical Review, 112(1), 114 - 122.
- [50] W. E. Spicer, A. Herrera-Gomez. (1993, October). Modern theory and applications of photocathodes. Proceedings of the International Society for Optical Engineering (SPIE) Symposium on Optics, Imaging and Instrumentation, (pp. 18 - 35). San Diego.
- [51] C. N. Berglund, W. E. Spicer. (1964, November). Photoemission Studies of Copper and Silver: Theory. Physical Review Letters, 136(4A), A1030 - A1044.
- [52] C D R Azevedo et al., "Towards THGEM UV-photon detectors for RICH: on single-photon detection efficiency in Ne/CH₄ and Ne/CF₄", 2010 JINST 5 P01002. [arXiv:0909.5357].
- [53] J. Escada et al., "Measurements of photoelectron extraction efficiency from CsI into mixtures of Ne with CH₄, CF₄, CO₂ and N₂", JINST 2009 4 P11025
- [54] L. C. C. Coelho et al., "Photoelectron transmission efficiency in Ar-CH₄ and Xe-CH₄ mixtures: Experimental results", NIM A 607 (2009) 587.
- [55] F. Piuz, A. B. (1999). Final tests of the CsI-based ring imaging detector for the ALICE experiment. Nuclear Instruments and Methods in Physics Research A (433), 178 - 189.

- [56] G. Charpak, R. Bouclier, T. Bressani, J. Favier, Č. Zupančič. (1968, July). The use of multiwire proportional counters to select and localize charged particles. *Nuclear Instruments and Methods*, 62, 262 - 268.
- [57] G. Charpak, P. Fonte, V. Peskov, F. Sauli, D. Scigocki, D. Stuart. (1991). Investigation of operation of a parallel-plate avalanche chamber with a CsI photocathode under high gain conditions. *Nuclear Instruments and Methods in Physics Research A*, 307, 63 - 68.
- [58] P. Fonte, T. Francke, N. Pavlopoulos, V. Peskov, I. Rodionov. (2005). Novel single photon detectors for UV imaging. *Nuclear Instruments and Methods in Physics Research A*, 553, 30 - 34.
- [59] Sauli, F. (1997). GEM: A new concept for electron amplification in gas detectors. *Nuclear Instruments and Methods in Physics Research A*, 386, 531 - 534.
- [60] Sauli, F. (2007, October). Imaging with the gas electron multiplier. *Nuclear Instruments and Methods in Physics Research Section A*, 580(2), 971 - 973.
- [61] M. Cortesi, R. Alon, R. Chechik, A. Breskin, D. Vartsky, V. Dangendorf. (2007, September). Investigations of a THGEM-based imaging detector. *Journal of Instrumentation*, 2.
- [62] J. F. C. A. Veloso, J. M. F. dos Santos, C. A. N. Conde. (2000, June). A proposed new microstructure for gas radiation detectors: The microhole and strip plate. *Review of Scientific Instruments*, 71, 2371 - 2376.
- [63] H. Natal da Luz, A. L. Gouvêa, J. A. Mir, J. M. F. dos Santos, J. F. C. A. Veloso. (2009, December). The 2D-Micro Hole & Strip Plate in CF₄ atmosphere aiming neutron imaging. *Journal of Instrumentation*, 4.
- [64] F. D. Amaro; C. Santos; J. F. C. A. Veloso; A. Breskin; R. Chechik; J. M. F. dos Santos. (2010, October). The Thick-COBRA: a new gaseous electron multiplier for radiation detectors. *Journal of Instrumentation*, 5.
- [65] D. Mörmann, A. Breskin, R. Chechik and C. Shalem, "Operation principles and properties of the multi-GEM gaseous photomultiplier with reflective photocathode". *Nuclear Instruments and Methods A* 530 (2004) 258-274.
- [66] R. Chechik, A. Breskin and C. Shalem; Thick GEM-like multipliers - a simple solution for large area UV-RICH detectors; *Nuclear Instruments and Methods A* 553(2005)35-40

- [67] A. Breskin, T. Boutboul, A. Buzulutskov, R. Chechik, G. Garty, E. Shefer, B.K. Singh. "Advances in gas avalanche photomultipliers". Nuclear Instruments and Methods in Physics Research section A 442 (2000), 58 - 67.
- [68] S Bressler, L Arazi, H Natal da Luz, C D R Azevedo, L Moleri, E Oliveri, M Pitt, A Rubin, J M F dos Santos, J F C A Veloso and A Breskin. "Beam studies of novel THGEM-based potential sampling elements for Digital Hadron Calorimetry". 2013 JINST 8 P07017
- [69] M. Cortesi, R. Zboray, R. Adams, V. Dangendorf and H.-M. Prasser, "Concept of a novel fast neutron imaging detector based on THGEM for fan-beam tomography applications". 2012 JINST 7 C02056.
- [70] A. Breskin et al., "CsI-THGEM gaseous photomultipliers for RICH and noble-liquid detectors", Nucl. Instrum. Meth. A 639 (2011) 117-120 [arXiv:1009.5883]. Also in A. Breskin, V. P. (2011). CsI-THGEM gaseous photomultipliers for RICH and noble-liquid detectors. Proceedings of the 7th International Workshop on Ring Imaging Cherenkov Detectors, (pp. 117 - 120). Cassis, Provence, France.
- [71] M. Alexeev et. al., "THGEM based photon detector for Cherenkov imaging applications". Nucl. Instrum. Methods Phys. Res., A 617 (2010) 396-397. Also in proceedings of the 11th Pisa Meeting on Advanced Detectors on Frontier Detectors For Frontier Physics, La Biodola, Italy, 24 - 30 May 2009, pp.396-397
- [72] A. Bondar, A. Buzulutskov, A. Grebenuk, D. Pavlyuchenko, R. Snopkov, Y. Tikhonov. (2007, October). First results of the two-phase argon avalanche detector performance with CsI photocathode. Nuclear Instruments and Methods in Physics Research Section A, 581(1 - 2), 241 - 245.
- [73] A. Bondar, A. Buzulutskov, A. Dolgov, A. Grebenuk, E. Shemyakina, a. Sokolov, D. Akimov, A. Breskin, D. Thers. (2013, February). Two-phase Cryogenic Avalanche Detectors with THGEM and hybrid THGEM/GEM multipliers operated in Ar and Ar+N₂. Journal of Instrumentation, 8.
- [74] B. Lopez Paredes, C. D. R. Azevedo, S. Paganis, A. L. M. Silva, N. J. C. Spooner, J. F. C. A. Veloso. (2015, July). Cryogenic Gaseous Photomultiplier for Position Reconstruction of Liquid Argon Scintillation Light. Journal of Instrumentation, 10.
- [75] Wenqing Xie, Yidong Fu, Yulan Li, Jin Li, Yuanjing Li, Qian Yue. (2015, February). Cryogenic THGEM-GPM for the readout of scintillation light from liquid argon. Nuclear Instruments and Methods in Physics Research Section A: Accelerators, Spectrometers, Detectors and Associated Equipment, 774, 120 - 126.

- [76] A. Badertscher, A. Curioni, U. Degunda, L. Epprecht, A. Gendotti, S. Horikawa, L. Knecht, D. Lussi, A. Marchionni, G. Natterer, K. Nguyen, F. Resnati, A. Rubbia and T. Viant, "First operation and drift field performance of a large area double phase LAr Electron Multiplier Time Projection Chamber with an immersed Greinacher high-voltage multiplier", 2012 JINST 7 P08026
- [77] DARWIN Collaboration (Aalbers, J. et al.), "DARWIN: towards the ultimate dark matter detector", JCAP 1611 (2016) no.11, 017 arXiv:1606.07001 [astro-ph.IM]
- [78] S. Duval, A. Breskin, R. Budnik, W. T. Chen, H Carduner, M. Cortesi, J. P. Cussonneau, J. Donnard, J. Lamblin, P. Le Ray, E. Morteau, T. Oger, J. S. Stutzmann, D. Thers. "On the operation of a micropattern gaseous UV-photomultiplier in liquid-Xenon". 2011 JINST 6 P04007.
- [79] S. Duval, L. A.-T.-P.-F. (2012, December). Hybrid Multi Micropattern Gaseous Photomultiplier for detection of liquid-xenon scintillation. Nuclear Instruments and Methods in Physics Research Section A, 695, 163 - 167.
- [80] D. Vartsky, I. Israelashvili, M. Cortesi, L. Arazi, A.E. Coimbra, L. Moleri, E. Erdal, D. Bar ,M. Rappaport, E. N. Caspi , O. Aviv and A. Breskin. "Liquid-Xe detector for contraband detection". Nuclear Instruments and Methods in Physics Research A 824 (2016) 240–242. [doi:10.1016/j.nima.2015.10.104](https://doi.org/10.1016/j.nima.2015.10.104).
- [81] I. Israelashvili, A. Coimbra, D. Vartsky, L. Arazi, S. Shchemelinin, E. N. Caspi, A. Breskin. "Fast-neutron and gamma-ray imaging with a capillary liquid-xenon converter coupled to a gaseous photomultiplier". To be published at JINST
- [82] L. Arazi et al., First observation of liquid-xenon proportional electroluminescence in THGEM holes, 2013 JINST 8 C12004 [arXiv:1310.4074].
- [83] I. Israelashvili, M. Cortesi, D. Vartsky, L. Arazi, D. Bar , E. N. Caspi and A. Breskin. "A Comprehensive Simulation Study of a Liquid-Xe Detector for Contraband Detection". 2015 JINST 10 P03030. <http://arxiv.org/abs/1501.00150>
- [84] M. Cortesi et al., THGEM operation in Ne and Ne/CH₄, 2009 JINST 4 P08001 [arXiv:0905.2916].
- [85] Escada J, Coelho L C C, Dias T H V T, Lopes J A M, Santos J M F d and Breskin A; "Measurements of photoelectron extraction efficiency from CsI into mixtures of Ne with CH₄, CF₄, CO₂ and N₂". 2009 JINST 4 P11025. [arXiv:0909.2965].
- [86] D. B. Carr, R. J. Littlefield, W. L. Nicholson, J. S. Littlefield. (1987, June). Scatterplot Matrix Techniques for Large N. Journal of the American Statistical Association, 82(398), 424 - 436.

- [87] M.J. French et al., "Design and results from the APV25, a deep sub-micron CMOS front-end chip for the CMS tracker", *Nuclear Instruments and Methods in Physics Research A* 466 (2001) 359–365.
- [88] S. Martoiu et al., "Development of the Scalable Readout System for Micro-Pattern Gas Detectors and Other Applications". *JINST* 8 (2013), C03015 doi:10.1088/1748-0221/8/03/C03015
- [89] A. E. C. Coimbra, I. Israelashvili, and J. M. F. dos Santos. "Photoelectron extraction efficiency from a CsI photocathode and THGEM operation in He-CF₄ and He-CH₄ mixtures". 2016 *JINST* 11 P03025. doi:10.1088/1748-0221/11/03/P03025.
- [90] Zhenzhou Liu, Jinxiang Chen, Pei Zhu, Yongming Li, Guohui Zhang. "The 4.438 MeV gamma to neutron ratio for the Am–Be neutron source". *Applied Radiation and Isotopes* 65 (2007) 1318–1321.
- [91] S. Agostinelli, et. al., "[GEANT4—a simulation toolkit](#)", *Nucl.Instr.Meth A* 506 (2003), 250-303.
- [92] A. Breskin, I. Israelashvili, M. Cortesi, L. Arazi, S. Shchemelinin, R. Chechik, V.Dangendorf, B. Bromberger and D. Vartsky. "A novel liquid-xenon detector concept for combined fast-neutron and gamma imaging and spectroscopy". 2012 *JINST* 7 C06008. doi: 10.1088/1748-0221/7/06/C06008.
- [93] R.H. French et al., "Optical properties of polymeric materials for concentrator photovoltaic systems", *Solar Energy Materials & Solar Cells* 95 (2011) 2077–2086.
- [94] C. Silva et al., "A model of the reflection distribution in the vacuum ultra violet region ", *Nucl. Instr. Meth. in Physics Research A* 619 (2010) 59–62
- [95] E. Aprile et al., " Simultaneous Measurement of Ionization and Scintillation from Nuclear Recoils in Liquid Xenon for a Dark Matter Experiment", *Phys. Rev. Lett.* 97, 081302 – Published 25 August 2006.
- [96] IDEX health and science: <http://www.idex-hs.com/products/868/Tefzel-ETFE-Tubing.aspx?ProductTypeID=1&ProductFamilyID=5>
- [97] <http://www.mathworks.com>
- [98] J.W. Marsh et al., " High resolution measurements of neutron energy spectra from Am-Be and Am-B neutron sources", *Nucl. Instr. and Meth. in Phys. Res. A* 366 (1995) 340-348.
- [99] Sitter, D.N., Goddard, J.S., and Ferrell, R.K., "Method for the measurement of the modulation transfer function of sampled imaging systems from bar-target patterns", *Applied Optics*, volume 34 (1995) 746-751.

- [100] V. J Lehr, J B Sibarita, J M Chassery, Image restoration in X-ray microscopy: PSF determination and biological applications, *IEEE Trans on Image Processing*, 7(2) (1998) 258-263.
- [101] A.E.C. Coimbra, A. Breskin and J.M.F. dos Santos; "THGEM operation in high pressure Ne/CF₄". 2012 JINST 7 C02062.
- [102] M. Alexeev et al.; "THGEM based photon detector for Cherenkov imaging applications". *Nucl. Instrum. Meth. A* 617 (2010) 396.
- [103] M. Alexeev et al., Development of THGEM-based photon detectors for Cherenkov Imaging Counters, 2010 JINST 5 P03009.
- [104] A. Breskin, R. Alon, M. Cortesi, R. Chechik, J. Miyamoto, V. Dangendorf, J. M. Maia, J. M. F. Dos Santos. "A concise review on THGEM detectors". *Nuclear Instruments and Methods in Physics Research A* 598 (2009) 107–111.
- [105] R. Alon, MSc thesis, Weizmann Institute of Science.
http://jinst.sissa.it/jinst/theses/2008_JINST_TH_001.pdf
- [106] R. Alon, M. Cortesi, A. Breskin and R. Chechik. "Time resolution of a Thick Gas Electron Multiplier (THGEM)-based detector", 2008 JINST 3 P11001
- [107] L. Arazi, A. E. C. Coimbra, E. Erdal, I. Israelashvili, M. L. Rappaport, S. Shchemelinin, D. Vartsky, J. M. F. dos Santos and A. Breskin. "Cryogenic gaseous photomultipliers and liquid hole multipliers: advances in THGEM-based sensors for future noble-liquid TPCs". 7th International Symposium on Large TPCs for Low-Energy Rare Event Detection. *Journal of Physics: Conference Series* 650 (2015) 012010. doi:10.1088/1742-6596/650/1/012010.
- [108] F. Sauli, "GEM: A new concept for electron amplification in gas detectors", *Nucl. Instrum. Meth. A* 386 (1997) 531.
- [109] A. Kozlov, I. Ravinovich, L. Shekhtman, Z. Fraenkel, M. Inuzuka, I. Tserruya, "Development of a triple GEM UV-photon detector operated in pure CF₄ for the PHENIX experiment", *Nucl. Instrum. Meth. A* 523 (2004) 345.
- [110] [D. Mörmann](#), [M. Balcerzyk](#), [A. Breskin](#), [R. Chechik](#), [B.K. Singh](#), [A. Buzulutskov](#), "GEM-based gaseous photomultipliers for UV and visible photon imaging", *Nucl. Instrum. Meth. A* 504 (2003) 93.
- [111] L. Arazi, private communication.
- [112] Y. Asser and A. Sharma, "Transport Properties of operational gas mixtures used at LHC", arXiv:1110.6761

[113] A. Rubin, L. Arazi, S. Bressler, L. Moleri, M. Pitt and A. Breskin, 2013 First studies with the Resistive-Plate WELL gaseous multiplier JINST 8 P11004 [arXiv:1308.6152]

[114] S. Bressler, L. Moleri, M. Pitt, S. Kudella, C.D.R. Azevedo, F.D. Amaro, M.R. Jorge, J.M.F. dos Santos, J.F.C.A. Veloso, H. Natal da Luz, L. Arazi, E. Olivieri and A. Breskin". First in-beam studies of a Resistive-Plate WELL gaseous multiplier". 2016 JINST 11 P01005 [arXiv:1510.03116]

[115] A. Buzulutskov, A. Breskin, R. Chechik. (1995, December). Heat enhancement of the photoyield from CsI, NaI and CuI photocathodes. Nuclear Instruments and Methods in Physics Research A, 366(2), 410 - 412.

[116] A. S. Tremsin, O. H. W. Siegmund. (2000, March). Heat enhancement of radiation resistivity of evaporated CsI, KI and KBr photocathodes. Nuclear Instruments and Methods in Physics Research Section A, 442(1 - 3), 337 - 341.

[117] MAXWELL 3D, ANSOFT Co, Pittsburgh, PA, U.S.A.

[118] ASTAR - stopping power and range tables for helium ions in various materials. National institutes of standards and technology.

<http://physics.nist.gov/PhysRefData/Star/Text/ASTAR.html>

10 List of all publications authored by Itamar during the study

1. A. Breskin, **I. Israelashvili**, M. Cortesi, L. Arazi, S. Shchemelinin, R. Chechik, V. Dangendorf, B. Bromberger and D. Vartsky. "A novel liquid-xenon detector concept for combined fast-neutron and gamma imaging and spectroscopy". 2012 JINST 7 C06008. doi: 10.1088/1748-0221/7/06/C06008.
2. **I. Israelashvili**, M. Cortesi, D. Vartsky, L. Arazi, D. Bar , E. N. Caspi and A. Breskin. "A Comprehensive Simulation Study of a Liquid-Xe Detector for Contraband Detection". 2015 JINST 10 P03030.
<http://arxiv.org/abs/1501.00150>
3. L. Arazi, A. E. C. Coimbra, E . Erdal, **I. Israelashvili**, M. L. Rappaport, S. Shchemelinin, D. Vartsky, J. M. F. dos Santos and A. Breskin."Cryogenic gaseous photomultipliers and liquid hole multipliers: advances in THGEM-based sensors for future noble-liquid TPCs". 7th International Symposium on Large TPCs for Low-Energy Rare Event Detection. Journal of Physics: Conference Series 650 (2015) 012010. doi:10.1088/1742-6596/650/1/012010.
4. L. Arazi, A. E. C. Coimbra, E. Erdal, **I. Israelashvili**, M. L. Rappaport, S. Shchemelinin, D. Vartsky, J. M. F. dos Santos, and A. Breskin. "First results of a large-area cryogenic gaseous photomultiplier coupled to a dual-phase liquid xenon TPC". 2015 JINST 10 P10020. <http://dx.doi.org/10.1088/1748-0221/10/10/P10020>.
5. A. E. C. Coimbra, **I. Israelashvili**, and J. M. F. dos Santos. "Photoelectron extraction efficiency from a CsI photocathode and THGEM operation in He-CF4 and He-CH4 mixtures". 2016 JINST 11 P03025. doi:10.1088/1748-0221/11/03/P03025.
6. D. Vartsky, **I. Israelashvili**, M. Cortesi, L. Arazi, A.E. Coimbra, L. Moleri, E. Erdal, D. Bar ,M. Rappaport, E. N. Caspi , O. Aviv and A. Breskin. "Liquid-Xe detector for contraband detection". Nuclear Instruments and Methods in Physics Research A 824 (2016) 240–242. doi:10.1016/j.nima.2015.10.104.
7. D. Vartsky, M. B. Goldberg, V. Dangendorf, **I. Israelashvili**, I. Mor, D. Bar, K. Tittelmeier, M. Weierganz, A. Breskin. "Quantitative discrimination between oil and water in drilled bore cores via fast-neutron resonance transmission radiography". Appl. Radiat. Isot. 118 (2016) 87-94 arXiv:1602.06533.

8. A. E. C. Coimbra, C. A. O. Henriques, **I. Israelashvili**, J. A. Mir, J. M. F. dos Santos. "Characterization of THGEM coupled to submillimetric induction gaps in Ne/CH₄ and Ar/CH₄ mixtures". 2017 JINST 12 P01013.
9. **I. Israelashvili**, A. Coimbra, D. Vartsky, L. Arazi, S. Shchemelinin, E. N. Caspi, A. Breskin. "Fast-neutron and gamma-ray imaging with a capillary liquid-xenon converter coupled to a gaseous photomultiplier". 2017 JINST 12 P09029.

11 List of publications resulting from this work

(in which Itamar is one of two equally contributing first authors)

1. A. Breskin, **I. Israelashvili**, M. Cortesi, L. Arazi, S. Shchemelinin, R. Chechik, V. Dangendorf, B. Bromberger and D. Vartsky. "A novel liquid-xenon detector concept for combined fast-neutron and gamma imaging and spectroscopy". 2012 JINST 7 C06008. doi: 10.1088/1748-0221/7/06/C06008.
 2. **I. Israelashvili**, M. Cortesi, D. Vartsky, L. Arazi, D. Bar , E. N. Caspi and A. Breskin. "A Comprehensive Simulation Study of a Liquid-Xe Detector for Contraband Detection". 2015 JINST 10 P03030.
<http://arxiv.org/abs/1501.00150>
 3. A. E. C. Coimbra, **I. Israelashvili**, and J. M. F. dos Santos. "Photoelectron extraction efficiency from a CsI photocathode and THGEM operation in He-CF4 and He-CH4 mixtures". 2016 JINST 11 P03025. doi:10.1088/1748-0221/11/03/P03025.
 4. D. Vartsky, **I. Israelashvili**, M. Cortesi, L. Arazi, A.E. Coimbra, L. Moleri, E. Erdal, D. Bar ,M. Rappaport, E. N. Caspi , O. Aviv and A. Breskin. "Liquid-Xe detector for contraband detection". Nuclear Instruments and Methods in Physics Research A 824 (2016) 240–242. doi:10.1016/j.nima.2015.10.104.
 5. **I. Israelashvili**, A. Coimbra, D. Vartsky, L. Arazi, S. Shchemelinin, E. N. Caspi, A. Breskin. "Fast-neutron and gamma-ray imaging with a capillary liquid-xenon converter coupled to a gaseous photomultiplier". In preparation; to be submitted to JINST.
-

